TÉCNICO LISBOA

Quantum Plasmonics

Luís Carlos Ferreira Rodrigues

Thesis to obtain the Master of Science Degree in

Electrical and Computer Engineering

Supervisor: Prof. Dr. Mário Gonçalo Mestre Veríssimo Silveirinha

Examination Committee

Chairperson: Prof. José Eduardo Charters Ribeiro da Cunha Sanguino
Advisor: Prof. Dr. Mário Gonçalo Mestre Veríssimo Silveirinha
Members of the Committee: Prof. Filipa Isabel Rodrigues Prudêncio

November 2018

Acknowledgments

I would like to thank my thesis supervisor, Prof. Mário Silveirinha. It has been a fantastic opportunity to work under its supervision due to all precious insights and knowledge.

To all my family, most notably to my mother, Teresa Ferreira, my father, António Bernardo, for their sacrifice, unconditional support and patience. Without them none of this would be possible.

Last, but not least, to my best friend, Joana Baleiras, the most honest thanks for the support and patience through these years and for the greatest help in this dissertation.

Declaration

I declare that this document is an original work of my own authorship and that it fulfills all the requirements of the Code of Conduct and Good Practices of the Universidade de Lisboa.

Abstract

In conducting materials such as metallic and semiconductor systems, coherent oscillations of collective free charge may be observed at frequencies usually in the ultraviolet spectrum. This phenomenon affects the permittivity response, which can assume negative values and allows sub-wavelength confinement of light, thus, enabling a wide range of applications. The rapid oscillations of the electron density can be quantized wherein a quantum of plasma oscillation is named plasmon. Due to this quantization, it is necessary to revise concepts of both Quantum Mechanics and the Plasmonics field. For a metal-dielectric interface, the coupling between light modes and plasmons confined at the interface gives origin to the quasi-particle surface plasmon-polaritons (SPP). The SPP represent the principal subject of this dissertation. The analysis of its permittivity response is performed either for the case where a local medium is assumed and for the scenario where the spatial dispersion is accounted. The quantization of the SPP electromagnetic field in the electrostatic regime is derived for both approaches. The spontaneous emission of SPP in the nonlocal approach is also subject of study for a system which consists in a two-level atom in the vicinity of a metal slab. The interaction between the atom and the SPP waves is examined, taking into account a local description of the SPP in the quasi-static approximation. Contrasts between strong and weak coupling regimes regarding the interaction of these two systems are also discussed.

Keywords: Plasmon, Plasma Frequency, Surface Plasmon-Polariton, Charge Density Oscillation, Quantum Mechanics, Operators, Quantization, Quantum Electrodynamics (QED), Harmonic Oscillator, Spontaneous Emission, Non-local Surface Plasmons

Resumo

Em materiais condutores como os metais e semicondutores, a oscilação coerente de cargas livres colectivas é observada para frequências tipicamente no espectro do ultravioleta. Este fenómeno afecta a resposta da permitividade, possibilitando que esta assuma valores negativos, e consegue também confinar a luz com comprimentos de onda inferiores aos correspondentes para a mesma onda em meio livre, abrindo portas para diversas aplicações. A oscilação rápida da densidade de eletrões pode ser quantizada, sendo o plasmão um *quantum* de oscilação do plasma. Graças a esta quantização, são introduzidos conceitos referentes à Mecânica Quantica e à Plasmónica. Para uma interface constituída por um metal e um dieléctrico, o acopulamento entre os modos de radiação e plasmões, confinados na interface, dá origem às quasi-partículas *surface plasmon-polaritons* (SPP). Os SPP são o principal foco de estudo nesta dissertação. A permitividade dos SPP é analisada para o caso em que o meio é local e para quando existe dispersão espacial. Em ambas as análises, é feita a derivação do campo electromagnético dos SPP no regime electroestático. Também é analisada a emissão espontânea de SPP para o problema em que se tem o átomo de dois níveis na vizinhança de uma chapa metálica. A interação entre estes dois elementos é também abordada, na qual se utiliza uma descrição local dos SPP no regime eletroestático. O contraste entre os regimes de acopulamento forte e fraco, relativamente à interação do átomo com os SPP, é contemplado neste estudo.

Keywords: Plasmões, Frequência de Plasma, Plasmões-Polaritões de Superfície, Oscilação de Densidade de Carga, Operadores, Quantização, Electrodinâmica Quântica,Oscilador Harmónico, Emissão Espontânea, Plasmões de Superfície Não-Locais

Contents

List of Tables

List of Figures

Acronyms

ABC Additional Boundary Conditions. 28

DA Dipole Approximation. 41

DOS Density of States. 32

FGR Fermi's Golden Rule. 46

JCM Jaynes–Cummings Model. 53

LDOS Local Density of States. 32

LSP Localized Surface Plasmons. 16

MBC Maxwellian Boundary Conditions. 28

RWA Rotating Wave Approximation. 41

SPP Surface Plasmon-Polaritons. 1, 13

TDPT Time-Dependent Perturbation Theory. 45

TLA Two-Level Atom. 41

Chapter 1

Introduction

1.1 Context and Motivation

In most of the cases, the preferential approach to characterize the dynamics of a given system is through the classical description, which is often desirable due to its simplicity and satisfactory results. However, not always the classical perspective is the most suitable one to apply for every systems, since, in general, the error associated with this overview increases as the spatial dimensions decrease. In those cases, it is mandatory the use of quantum theory, where the dynamics of the system are fully captured (depending on the exhaustive description assumed). It is worth to mention that the classical and quantum theories are not incompatible theories. In fact, the quantum theory predicts the classical properties for problems at the macroscopic scales or having a huge number of particles. The physical quantities described by a Newtonian description are linked with its quantum characterization through the expectation value of the corresponding observable.

The main objective of this dissertation is the study of problems with relevant effects and properties in the quantum realm and their principal consequences and features when comparing to the classical description of the same ones. More specifically, the systems of interest are inserted in the quantum plasmonic research field [15], that combines the modern plasmonics with the quantum optics field. The plasmons consist in a coherent oscillation of the free density charge, that emerges at high frequencies (usually in the visible and ultraviolet spectra) in conducting materials such as metals and semiconductors [16].

The plasmons may appear in different scenarios giving rise to different phenomena, *e.g.*, the bulk plasmons, the localized plasmons and the Surface Plasmon-Polaritons (SPP), being the latter one of most concerns in this work. Moreover, the SPP are characterized by a strong interaction between light and plasmons and can be treated as a quasi-particle, allowing a quantum description of their features and properties. The introduction of the joint state of matter and light was introduced by Hopfield [17]. Depending on the type of matter, these are called phonon-polariton, when referred to the quasi-static ions, and plasmon-polariton for the electron charge gas scenario. After the Hopfield's approach, it was then first quantized the SPP by Ritchie *et al.* [18], where certain properties of the system like the hydrodynamic effects were not addressed, being later exploited by Nakamura [19]. Afterward, other formulations for the SPP quantization were developed, in which the loss nature of the plasmons is taken into account. This loss emerges from electron collisions with the background ions and themselves. This dispersive effect may be nowadays quantized by a microscopic method or via a macroscopic analysis, using the Green's functions [5].

The interest in this field (plasmonics) is related with the outstanding range of possible practical applications, due to their unique characteristics, such as the subwavelength confinement and the capacity to support waves that go beyond diffraction limit [20]. These properties allow the use of plasmons to produce superlenses, where the spatial resolution of an object is enhanced when compared to the traditional optical lenses built with positive permittivity materials. Plasmons are also present in biosensors (which are later presented) since their

reflectance and transmittance cross-sections are extremely sensitive to modifications in the surrounding environment. As well, their strong coupling to light is a desirable feature for light control via highly confined fields at the surface of a metal-dielectric interface, which is very appealing for electronic circuit applications due to their small dimensions. Other applications such as spectroscopy analysis, antennas, light emitters and waveguides are also part of the plasmon applications. In order to explain the emission of SPP radiation by a quantum emitter is necessary to quantize the modes of the electromagnetic field and solve the *Schrödinger* equation. Moreover, only using a quantum description of the system, it is possible to explain the spontaneous emission of SPP in the presence of a quantum object.

The surface plasmons are typically introduced considering an homogeneous medium, which enables a local response of its permittivity to an external electric field. However, for problems where the dimensions are of the nanometer scale, effects such as the repulsive interaction between the free electrons become more relevant and provoke a non-homogeneous spatial distribution of the charge density. This diffusion effect is already described using thermodynamic theory, that result in approaches such as the *hydrodynamic model* [21].

In order to dispose of a quantum description of the SPP, it is necessary to introduce concepts of quantum mechanics, as well as derive its classical electromagnetic field using *Maxwell equations*. In addition, some of the plasmonic applications are revised in this work to show the fundamental features of these systems, which make this field so appealing.

This dissertation proposes to study the interaction of a quantum object (*e.g.*, an atom) that is placed in the vicinity of a metal slab, which is capable of supporting SPP waves. To conduct this analysis, it is introduced the quantization of the SPP electromagnetic field in the electrostatic regime, either using a local description of the medium and one where the spatial dispersion response is considered. The coupling between these two systems can fall either into the strong or into the weak regimes. Therefore, the temporal evolution of the system is examined in both regimes. In addition, the probability of finding the atom in excited and ground states is computed over time.

As an initial approach, the problem is considered to have no loss channels and the dynamics of the system are simply obtained by solving the *Schrödinger* equation , where the *Hamiltonian*'s system is composed by the the *Hamiltonian* of the atom and of the SPP and by the *Hamiltonian* due to the interaction between them. Afterward, the inclusion of losses is made heuristically by considering a term that accounts with radiation dispersed via spontaneous emission.

Hence, the spontaneous emission of SPP is also studied, where is assumed that in the initial state of the system the atom is in an excited state. Moreover, the comparison of the emission rates for the cases where the local and a non-local description of the SPP is made and in the scenario where the quantum object is in free space. The effects of the nonlocality are also addressed, when discussing the density of states for the SPP in the quasi-static approximation, being also commented its local limit.

1.2 Dissertation Outline

This dissertation is organized in six chapters.

Chapter 1 presents the objectives of this work, taking into account the physical motivation behind them.

Chapter 2 introduces the main concepts of Quantum Mechanics and Plasmonics, wherein the latter some of its applications are discussed. Then, useful problems formulations are presented such as the quantum harmonic oscillator, which allows to explain the quantization of the SPP in a local media, also mentioned in this Chapter.

Chapter 3 studies the non-local SPP scenario where a structure for the its electric fields as well as the dispersion relation for this propagation waves are derived. The density of states is also computed for the non-local SPP and is compared with its local analogous and the density of states in free space. The quantization of the non-local SPP electromagnetic field is also addressed.

Chapter 4 describes the quantum model for light-matter systems. First, explains the two-level atom (TLA) and, then, the light-matter interaction for the case of having an electromagnetic wave classically described. Finally, the spontaneous emission of non-local SPP is computed.

Chapter 5 provides the study of local SPP with respect to the atom quantum interaction. First, introduces the Hamiltonian reformulation. Then, the lossless interaction between TLA and SPP in the local quasi-static approximation, where the strong and weak coupling regimes are compared.

Chapter 6 concludes the dissertation and introduces a few ideas for future work.

Chapter 2

Main Concepts

2.1 Quantum Mechanics Concepts

2.1.1 Modern Physics Compared to Classical Physics

Quantum physics emerged in 20^{th} century and was powered by phenomena such as the black body radiation spectrum, the photoelectric effect and the double slit experiment. These instigated the introduction of the discrete energy states (quantum) concept and the wave-particle duality feature of matter. Moreover, quantum mechanics defines correctly the behavior of matter and interactions between particles at scales near atom sizes, where the classical approach yields inaccurate results when comparing to the experimental data. Therefore, since that is an increasing interest on searching for smaller devices offering the same or higher performances, it is expectable that quantum mechanics approach will continue to be a requirement in order to account with effects that are meaningful at nanoscales.

2.1.2 Postulates

Quantum theory [22] enlightens that the state of a system can be described by a mathematical complexed valued wavefunction, generally denoted by Ψ, which contains all the information within a system and in particular can represent the configuration of a particle.

The following five postulates are axioms of non-relativistic quantum mechanics, which as intrinsic property do not need any further proof. These axioms were introduced because their derived results provide an extremely precision when compared to the experimental data.

- **Postulate 1:** A quantum mechanical system is absolutely characterized by the wavefunction $\psi(x,t)$ in a Hilbert space and $\psi^*(x,t)\,\psi(x,t)$ is the distribution density probability amplitude that must verify Eq. 2.1

- **Postulate 2:** Each observable (physical entity) in classical physics corresponds to a linear Hermitian operator (represented by a matrix) in quantum mechanics.

- **Postulate 3:** A particle in a given state ψ_1, after an ideal measurement of a physical property $\hat{\mathbf{\Omega}}$, will yield to an eigenvalue ω and will collapse into an eigenstate Φ_1 (i.e. $\hat{\mathbf{\Omega}}\vec{\psi}_1 = \omega\vec{\Phi}_1$), such that $\vec{\psi}_1 \rightarrow \vec{\Phi}_1$. The state ψ_1 is however a superposition (linear combination) of eigenstates with coefficients C_n, where $\|C_n\|^2$ represents the probability to measure the state Φ_n.

- **Postulate 4:** Every Hermitian operator contains a complete eigenbasis (formed by the eigenstates) which implies that any possible state is contained in the linear expansion of eigenstates (Spectral Theorem).

Table 2.1: Common operators in Quantum Physics and its correspondent physical entity.

Physical Entity	**Operators**	**Physical Entity**	**Operators**
Position	X	Hamiltonian	$H = -\frac{\hbar^2}{2m}\frac{\partial^2}{\partial^2 x} + V(x,t)$
Linear Momentum	$P_x = \frac{\hbar}{i}\frac{\partial}{\partial x}$	Momentum with Electromagnetic field	$P_x = \frac{\hbar}{i}\frac{\partial}{\partial x} - qA_x$
Angular Momentum	$L_x = -i\hbar(y\frac{\partial}{\partial x} - x\frac{\partial}{\partial y})$	Kinetic Energy with Electromagnetic field	$T_x = \frac{1}{2m}(-i\hbar\frac{\partial}{\partial x} - qA_x)^2$
Kinetic Energy	$T_x = -\frac{\hbar^2}{2m}\frac{\partial^2}{\partial^2 x}$		

• **Postulate 5:** The time evolution of the wavefunction obeys to the first order derivative in respect to time Schrödinger equation (Eq.2.2), where $\hbar$ is the reduced Planck constant and $\hat{\mathbf{H}}$ is the Hamiltonian operator.

$$\int_{-\infty}^{\infty} \overrightarrow{\psi}^{*}(x,t)\,\overrightarrow{\psi}(x,t)\,dx = 1 \tag{2.1}$$

$$i\hbar\frac{d}{dt}\overrightarrow{\psi}(x,t) = \hat{\mathbf{H}}\overrightarrow{\psi}(x,t) \tag{2.2}$$

In fact, ψ can be represented in any basis corresponding to an observable physical entity (*e.g.* momentum, position, etc.), and its squared amplitude represents the density probability of measuring that observable, which implies a correct normalization given by Eq. 2.1. Moreover, in order to have physical meaning, $\psi(x,t)$ must be continuous and has to vanish at infinity ($x = \pm\infty$). These two constraints are often applied as boundary conditions on the energy eigenvalues determination. The profound difference between classical and quantum physics is stressed by the fact that, in quantum mechanics, a system has a probability of behaving in a certain way instead of having an inexorable deterministic behavior.

The mechanism of an operator ($\hat{\mathbf{\Omega}}$) acting on a given wavefunction represents the measurement of the correspondent system's physical entity (*e.g.* position or energy). Thus, the values of the measurements can only correspond to the possible eigenvalues (ω). In Table 2.1 are represented, for a particle in one spatial dimension, some relevant Hermitian operators and their associated transformation when acted on a wavefunction in the position x basis [22].

Postulates 3 and 5 may seem counterintuitive since one of them suggests that a particle's behavior evolves following deterministic rules (Schrödinger equation) unless a measurement is made. On the other hand, when an observation is done, postulate 3 states that the particle collapses into a certain eigenstate with a probability ($\mid cn \mid^2$) associated.

Another important property arises from the postulate 4, where interference effects emerge from the superposition of wavefunctions which enable to explain the quantum nonlocality and is the theoretical grounds of quantum information theory[23]. In fact, any wavefunction can be written as the sum over all states with exact momentum (Eq. 2.3 and position (Eq. 2.4), where e^{ikx} and $\delta(x - x_0)$ are the definite states of each physical quantity, respectively, and $\tilde{\psi}$ are the coefficients.

$$\psi(x) = \frac{1}{2\pi}\int \tilde{\psi}(k)\,e^{ikx}dk \tag{2.3}$$

$$\psi(x) = \frac{1}{2\pi}\int \tilde{\psi}(x_0)\,\delta(x - x_0)\,dx_0 \tag{2.4}$$

The dot product between an eigenstate $\vec{\psi}_n$ and the system wavefunction is typically evoked to calculate the coefficient c_n. Since the eigenfunctions form a complete basis, they must be orthogonal to each other, hence

this fact can be reproduced in Eq. 2.5 where δ_{mn} function is equal to one if $m = n$ or zero otherwise.

$$\left\langle \vec{\psi}_n | \vec{\psi} \right\rangle = \vec{\psi}_n \sum_{m=1}^{\infty} c_m \vec{\psi}_m = c_n \delta_{mn} \tag{2.5}$$

2.1.3 Expectation Value and Uncertainty

Classical predictions usually have a counterpart in quantum mechanics expressed among the expectation value of a system (a consequence of the Ehrenfest theorem), which is defined in the following Eq. 2.6 in different notations. Note that x appears in the right side of the equation multiplying due to the operation of $\hat{\mathbf{X}}$ upon acting on function $f(x)$. Therefore, if one want to compute the expectation value of some other observable, the proper transformation of that operator must be used.

$$\left\langle \vec{\psi}_n \middle| \hat{\mathbf{X}} \middle| \vec{\psi} \right\rangle = \int \psi^*(x)\, x\psi(x)\, dx \tag{2.6}$$

The formula that gives the uncertainty of measuring a physical quantity comes in Eq. 2.7, where the physical entity is chosen to be the position.

$$\sigma_x^2 = \left\langle \hat{\mathbf{X}}^2 \right\rangle - \left\langle \hat{\mathbf{X}} \right\rangle^2 = \int_{-\infty}^{\infty} \psi^*(x)\, x^2 \psi(x)\, dx - \left\langle \hat{\mathbf{X}} \right\rangle^2 \tag{2.7}$$

Certain physical properties of a system are incompatible, *i.e.*, they cannot be defined at the same time within a system, which follows the Heisenberg's uncertainty principle that can be written as Eq. 2.8a or Eq. 2.8b in terms of commutators ($[A, B] = AB - BA$). The most famous example where this happens is for the case of position and momentum, where if the position of a particle is precisely known (in practice this is not achievable) then the momentum at that same moment is devoid of meaning, *i.e.*, it cannot be known even theoretically. The uncertainty is a fundamental property inherent in quantum mechanics nature and the more precise a physical quantity is, the less exact is its incompatible pair.

$$\sigma_x \sigma_p \geq \frac{\hbar}{2} \tag{2.8a}$$

$$\left[\hat{\mathbf{X}}, \hat{\mathbf{P}}\right] = i\hbar \tag{2.8b}$$

2.1.4 Schrödinger Equation

The time evolution of a system can be interpreted as the rotation of ψ in the Hilbert space. Therefore, for a basis that rotates at the same rate as the time evolution, the eigenfunction will seem static and the operator, in contrast, will be time dependent. The latter corresponds to the *Heisenberg formalism* of quantum mechanics. Hereafter, the characteristics of the *Schrödinger picture* and then the *Heisenberg* picture are highlighted.

The Hamiltonian, for conservative forces, represents the total energy of a system just as in the classical view, where $V(x)$ represents the potential energy [22].

Although Eq. 2.2 is the general time-dependent *Schrödinger equation*, it is often convenient to split into two simpler equations, Eq. 2.9a and Eq. 2.9b, and solve them distinctly, where E appears as the eigenvalue of the time-independent Hamiltonian. The purpose is that, by postulate 3, any state (even for time-independent Hamiltonian) can be composed by a linear combination of eigenfunctions $\psi_E(x,t)$.

$$\mathrm{E}\psi_E(x,t) = \left[-\frac{\hbar^2}{2m}\frac{\partial^2}{\partial x^2} + V(x)\right]\psi_E(x,t) \tag{2.9a}$$

$$\mathrm{E}\psi_E(x,t) = i\hbar\frac{\partial \psi_E(x,t)}{\partial t} \tag{2.9b}$$

The solutions of Eq. 2.9b are in the form plane waves, $\psi_E(x)\, e^{-iEt}$, and are designated by stationary states due to its probability be time-independent. Afterward, the computation of Eq. 2.9a is easily extracted just by recalling that the wavefunction solution must respect the continuity and boundary constraints. In typical scenarios, it will exist more constraints than free parameters to determine and consequently, this will lead to the quantization of the energy system where only some allowed energies (quanta) solve the equation. Eq. 2.9a can be rearranged in Eq. 2.10 where $k(x)^2 = \frac{2m}{\hbar^2}(V(x) - E)$ and one can inspect that for $V(x) > E$ the solution is composed of exponential wavefunctions (that must vanish at infinite) and if $V(x) < E$ then the equation is solved by sines and cosines.

$$\frac{\partial^2 \psi_E(x,t)}{\partial x^2} = k(x)^2 \psi_E(x,t) \tag{2.10}$$

However, the usual scenarios and the ones with practical interest possess a time-dependent Hamiltonian. Hence, one must adopt a new approach named *Perturbation Theory*, that is explained at [22] and takes into account small variations of the time-dependent component. When the potential is greater than the particle energy, it is common to appear states that are confined in a certain region of space, as in the case of a particle in a box, which are designated bound states. This does not stand for every potential greater than the energy and, in particular conditions, the particle can even pass through the disallowed region, which is the so-called *quantum tunneling* [24].

2.1.5 Quantum Electrodynamics

In order to provide a quantum description of the electromagnetic field, it is important to mention the relevant consequences and features that it entails [25]. In fact, in examples such as the spontaneous emission, the *Casimir force* (later discussed), the laser line-width, squeezed photon states, etc., the use of quantized radiation modes becomes crucial for the sake of their explanation.

Since the electric and magnetic fields can be decomposed into a linear expansion of normal modes in the Fourier space, by Maxwell equations inspection, the wave equations in Eq. 2.11 and Eq. 2.12 may be obtained, where $\mathrm{E}(k)$ and $\mathrm{B}(k)$ are the Fourier transform of electric and magnetic fields, respectively and c is the light speed. Their resemblance to the uncoupled harmonic oscillator equations is the key for all the further analysis. In fact, one of the most important properties for the resolution of certain problems in quantum mechanics is the expansion of the system in terms of harmonic oscillators, which have well-known solution described in Subsection 2.3.1.

$$\frac{d^2\mathrm{E}(k)}{dx^2} + c^2 k^2 \mathrm{E}(k) = 0 \tag{2.11}$$

$$\frac{d^2\mathrm{B}(k)}{dx^2} + c^2 k^2 \mathrm{B}(k) = 0 \tag{2.12}$$

In quantum electrodynamics, it is desirable to quantize the radiation field rather than the *Coulomb* field of the charged particles, since the radiation field has its own degrees of freedom, unlike the *Coulomb* field, for which they are determined by the charged particles [26]. For a free space electromagnetic field quantization without sources, there is no need to resort to electromagnetic potentials neither to provide a gauge.

However, it is worth to mention that, for systems with external sources, is mandatory to choose an adequate (if possible) vector potential and gauge, in order to facilitate the quantization of the electromagnetic field. Moreover, each gauge has its own commutation relationships and the most common ones are the *Coulomb gauge*, where is imposed the condition $\nabla \cdot \vec{A} = 0$ ($\vec{A}$ is the magnetic vector potential), and the *Lorenz gauge*, whose condition is given by $\partial_\mu A^\mu = 0$ (where A^μ is the four-potential). The *Coulomb gauge* advantage relies on the fact that it holds the capacity to yield to transverse photons or, after an appropriate transformation, to photons with helicity. In contrast, the *Lorenz gauge* benefits from the *Lorentz invariance*.

Due to the simpler analysis and the ability to reproduce all the desirable results for this context, it will be further presented electromagnetic field quantization for the free space scenario without any gauge usage.

2.1.6 Free-Space Electromagnetic Field Quantization

The quantization of the electromagnetic field, provided below, is valid only for the case where the medium is non-dispersive and is a reproduction of the formulation present in [27]. For the dispersive medium scenario, only the final result of the quantization is mentioned (for a deeper understanding consult [28]).

In order to be able to quantize the electromagnetic field, it is often considered a cavity terminated with periodic boundary conditions. This method allows decomposing the radiation fields as a sum of normal field modes, each mode associated with a unique combination between a wavenumber k and polarization n. This assumption is very useful since it allows discretizing the integral over all the field modes into a sum. In fact, this method does not provide any less information and any boundary condition considered reproduces the same results.

Beginning by a classical overview of the electromagnetic field by presenting bellow the Maxwell equations in free space and without external charges. To accomplish that, it is employed a matricial formalism [29] where is used a six dimensional vector to represent either the electrical and magnetic fields, $\mathbf{F} = (\mathbf{E}, \mathbf{H})^T$, and either the electrical displacement and magnetic induction fields,$(\mathbf{D}, \mathbf{B})^T$, which are related to each other through Eq. 2.13.

$$\begin{pmatrix} 0 & i\nabla\times \\ -i\nabla\times & 0 \end{pmatrix} \begin{pmatrix} \mathbf{E} \\ \mathbf{H} \end{pmatrix} = i\frac{\partial}{\partial t} \begin{pmatrix} \mathbf{D} \\ \mathbf{B} \end{pmatrix} \tag{2.13}$$

Considering the case of isotropic materials, which is sufficient for the further analysis on this report, the constitutive relations may be written using a matrix $\mathbf{M} = \mathbf{M}(r)$, that concerns the material properties and is defined for each spatial point. As it is possible to observe in Eq. 2.14, the matrix $\mathbf{M}$ is real-valued and Hermitian since $\mathbf{M} = \mathbf{M}^\dagger$, which will be essential for the sake of the derivation.

$$\begin{pmatrix} \mathbf{D} \\ \mathbf{B} \end{pmatrix} = \begin{pmatrix} \varepsilon_0\varepsilon(r) & 0 \\ 0 & \mu_0\mu(r) \end{pmatrix} \begin{pmatrix} \mathbf{E} \\ \mathbf{H} \end{pmatrix} \tag{2.14}$$

This way, the Maxwell equations may be represented only in terms of E and H by Eq. 2.15, where the $\mathbf{N}$ matrix is the one that appears in the left side of the Eq. 2.13.

$$\mathbf{N} \cdot \mathrm{F} = i\mathbf{M} \cdot \frac{\partial \mathrm{F}}{\partial t} \tag{2.15}$$

Moreover, since the energy stored in the electromagnetic field is given by Eq. 2.16, it is obvious that this energy must be always positive by reminding that the matrix M is positively defined for all space.

$$H_{EM} = \frac{1}{2}\int d^3r \mathrm{BH} + \mathrm{DE} = \frac{1}{2}\int d^3r \mathrm{F} \cdot \mathbf{M} \cdot \mathrm{F} \tag{2.16}$$

In order to proceed further, an inner product between two vectors, denoted by $\langle|\rangle$, must be defined. This is fulfilled through Eq. 2.17, where $\mathrm{F}_1$and F_2 are considered as electromagnetic field vectors. The latter expression is analogous to the structure of the stored energy equation.

$$\langle \mathrm{F}_1 | \mathrm{F}_2 \rangle = \frac{1}{2}\int d^3r \mathrm{F}_1 \cdot \mathbf{M}(r) \cdot \mathrm{F}_2 \tag{2.17}$$

So, by the same argument as used before, the inner product verifies $\langle \mathrm{F}|\mathrm{F}\rangle > 0$, if F is not the null vector. Assuming that F_1 and F_2 respect the periodic boundary conditions in a given cavity, it is then verifiable that the condition in Eq. 2.18 holds.

$$\left\langle \mathbf{M}^{-1}\mathbf{N}\mathrm{F}_2 | \mathrm{F}_1 \right\rangle = \left\langle \mathrm{F}_2 | \mathbf{M}^{-1}\mathbf{N}\mathrm{F}_1 \right\rangle \tag{2.18}$$

This is the same as saying that $\mathbf{M}^{-1} \cdot \mathbf{N}$ is a Hermitian operator, from which immediately follows that exists a complete basis formed by the eigenfunctions of that operator, such that

$$\mathbf{M}^{-1} \cdot \mathbf{N} \left|\mathrm{F}_n\right\rangle = \omega_n \left|\mathrm{F}_n\right\rangle \tag{2.19}$$

where ω_n is the eigenfrequency associated with the n mode of $|\mathrm{F}\rangle$ inside the cavity. One should notice that $|\mathrm{F}_n\rangle$ can only be complex, since, otherwise, the equation above would have an imaginary term on the left side and a real one on the right side. Also, the eigenfunctions correspondent to different modes are orthogonal to each other, which is depicted in Eq. 2.20. Recalling that the matrix $\mathbf{M}$ is real valued, it is enough to conjugate Eq. 2.19 on both sides to see that the eigenvalue correspondent to the state F_n^* can only be $-\omega_n$, which consequently implies a symmetry on the frequency spectrum.

$$\langle \mathrm{F}_n | \mathrm{F}_m \rangle = \frac{1}{2} \int d^3 r \mathrm{F}_n^* \cdot \mathbf{M}\left(r\right) \cdot \mathrm{F}_m = \delta_{mn} \tag{2.20}$$

In addition, only transverse modes exist since it is considered the scenario where there are no external charges (*i.e.*, $\nabla \cdot \mathrm{D} = 0$) and the medium is non-dispersive. Resourcing to the formulation of the electromagnetic field normal modes in a cavity with periodic boundary conditions, E and H are expanded by transverse eigenmodes in the compact way visible in Eq. 2.21. The coefficients are given by $b_n = \langle \mathrm{F}_n | \mathrm{F} \rangle$ and $b_n^* = \langle \mathrm{F}_n^* | \mathrm{F} \rangle$.

$$\mathrm{F} = \sum_{\omega_{nk} > 0} b_n \mathrm{F}_n\left(r\right) + b_n^* \mathrm{F}_n^*\left(r\right) \tag{2.21}$$

Although it may seem counter intuitive that the sum is only defined for $\omega_n > 0$, in fact the negative frequencies are present in the $\mathrm{F}_n^*\left(r\right)$ modes, as mentioned earlier. The next step stresses the computation of the stored energy (defined in Eq. 2.16) of the electromagnetic field, now defined as an expansion of transverse modes, which enables to convert the integral into a sum. By the orthogonality between different modes (Eq. 2.20 and the inner product definition, previously discussed, follows

$$H_{EM} = 2 \sum_{\omega_n > 0} \left\|b_n\right\|^2 = \sum_{\omega_n > 0} {b'}_n^{\,2} + {b''}_n^2 \tag{2.22}$$

where b'_n is the real part of b_n and ${b''}_n$ is the imaginary one. In order to F be ruled by the Maxwell equations, it is crucial that$\omega_n b_n = i \frac{d}{dt}(b_n)$, which leads to the simple solution $b_n\left(t\right) = b_n\left(0\right) e^{-i\omega_n t}$. Therefore, the real and imaginary components of b_n must be such that $\frac{d}{dt} b'_n = \omega_n {b''}_n$ and $\frac{d}{dt} {b''}_n = -\omega_n b'_n$. At this moment one should notice that b'_n and ${b''}_n$ present similar relations and structure comparing to the ones of the habitual conjugate variables x_n and p_n, being these the spatial coordinate and momentum, respectively. This is the crucial moment where the jump from the classical overview to the quantum one can be taken, since b'_n and ${b''}_n$ may be defined in terms of x_n and p_n, respectively. This equivalence is made such that the stored energy of each electromagnetic field mode corresponds to the energy of an uncoupled harmonic oscillator, which have a known quantum description. Thus, since the energy of uncoupled harmonic oscillators is given by the following equation (further addressed in Subsection 2.3.1)

$$H_{HO} = \sum_{\omega_n > 0} \left(\frac{1}{2} m \omega_n^2 x_n^2 + \frac{1}{2m} p_n^2 \right) \tag{2.23}$$

then ${b''}_n = \frac{1}{2\sqrt{m}} p_n$ and $b' = \frac{\omega_n}{2} \sqrt{m} x_n$. It is therefore sustained the assumption that the electromagnetic field is described by an infinite composition of uncoupled harmonic oscillators, since the same relations ($\frac{dx_n}{dt} = \frac{p_n}{m} = \frac{\partial H_{EM}}{\partial p_n}$ and $\frac{dp_n}{dt} = -m\omega_n^2 x_n = -\frac{\partial H_{EM}}{\partial x_n}$) prevail. Using the Dirac canonical quantization, where the canonical commutation relations$[x_n, p_n] = i\hbar$ must be observed, the canonical coordinates are promoted to operators. This may be accomplished by writing $\mathbf{X}_n$ and $\mathbf{P}_n$ in terms of the raising and lowering operator ($\hat{\mathbf{a}}^\dagger$

and $\hat{\mathbf{a}}$, respectively), where $X_n = \sqrt{\frac{\hbar}{2m\omega_n}}\left(\hat{\mathbf{a}}_n + \hat{\mathbf{a}}_n^\dagger\right)$ and $P_n = i\sqrt{\frac{\hbar m\omega_n}{2}}\left(\hat{\mathbf{a}}_n^\dagger - \hat{\mathbf{a}}_n\right)$.

The last step is to write down the quantization of electromagnetic field (Eq. 2.24) using the knowledge that Hamiltonian operator of the quantum harmonic oscillator is given by $\mathbf{H}_{HO} = \hbar\omega\left(\hat{\mathbf{a}}_n^\dagger\hat{\mathbf{a}}_n + \frac{1}{2}\mathbf{I}\right)$. The operators for the magnetic induction $\mathbf{B}$ and the electric displacement $\mathbf{D}$ appear just from the matricidal multiplication $\mathbf{M}\cdot\mathrm{F}$.

$$\hat{\mathbf{F}} = \begin{pmatrix} \hat{\mathbf{E}} \\ \hat{\mathbf{H}} \end{pmatrix} = \sum_{\omega_\mathrm{n}>0}\sqrt{\frac{\hbar\omega_\mathrm{n}}{2}}\left(\hat{\mathbf{a}}_n\mathrm{F}_\mathrm{n}\left(\mathrm{r}\right) + \hat{\mathbf{a}}_n^\dagger\mathrm{F}_\mathrm{n}^*\left(\mathrm{r}\right)\right) \tag{2.24}$$

A striking consequence from the above quantization is the fact that the electromagnetic field in a cavity is discrete and that each energy mode is associated to a certain number of photons. In the ground state no quanta are present, corresponding to the vacuum scenario, but if one applies the creation operator to that state, may notice that the energy rises due to the emergence of one photon. Similarly, if one continues to use $\hat{\mathbf{a}}^\dagger$ to the ground state, it will appear as many photons as many times this operator is employed, and thus, a greater energy as well. Although this result is only valid for non-dispersive media, the formula for a dispersive medium is identical to the one at Eq. 2.24, with a little difference in the F_n terms, that follow a different normalization from the one mentioned in Eq. 2.20. The reason is implicit in the frequency dependence on the material matrix ($\mathbf{M} = \mathbf{M}\left(r,\omega\right)$), and consequently in this case the normalization is introduced as in Eq. 2.25, where the paper [28] should be consulted for a detailed description on all the formalism behind it.

$$\langle\mathrm{F}_n|\mathrm{F}_m\rangle = \frac{1}{2}\int d^3r\mathrm{F}_n^*\cdot\frac{\partial\left[\omega\mathbf{M}\left(r\right)\right]}{\partial\omega}\cdot\mathrm{F}_m = \delta_{mn} \tag{2.25}$$

2.2 Plasmonics

2.2.1 Brief Description

With the purpose of introducing the concepts behind plasmons, one must understand previously that the device's dimensions involving plasmonic features are of the order of hundreds of nanometers or less. Therefore, one must attend that the influence of quantum effects may represent a substantial origin of error among the mathematical system description and the experimental results observed. In metals (good conductors) it is attained for energies near the *Fermi level* the free electron motion (valence electrons), which can be controlled by an external field [2]. The plasmon is the quantum of free electrons oscillation waves, oscillating relatively to fixed positive ions in a metal, and may be perceived as a collection of electrons (electron gas), which is described as a quasiparticle with discrete energy and momentum (for propagation modes), identical to a photon for electromagnetic oscillations. This resemblance permits an analogy on the procedure undertaken to quantize the electromagnetic waves in photons to the electrostatic wave in plasmon case. Although one should use a quantum model to characterize the system, almost all the important properties can be unveiled with a classical free electron model.

This phenomenon emerges in different circumstances, such as volume plasmons, surface plasmons, local plasmons and others that will not be addressed on this thesis. Each of them has different characteristics and, hence, different possible applications in multiple fields.

2.2.2 Drude's Model

To develop a further analysis regarding the plasmons behavior, it is crucial to capture the free electrons response (permittivity) in metals to an external electric field. This can be attained by using *Drude's model* [30], which is a particular case of *Lorentz model* with no restoring force (since the electrons are free), and that describes the motion of the electron "gas" (conduction electrons) moving against a background of heavy immobile ions in metals using classical kinetic theory. The assumptions made are:

- Electron scattering with other electrons, photons, impurities and the bulk (positive ions) are accounted for the kinetics analysis by the empirical parameter τ, which stands for the mean time between collisions. Other possible interactions are neglected, which is in practice a good approximation.

- Electron collisions are instantaneous and uncorrelated enabling describing the system as a Poisson process, and therefore the momentum is considered zero on average after scattering.

- The probability of collision in an instantaneous time interval is dt/τ.

- Electrons achieve thermal equilibrium with lattice only by collisions.

If an external electric field E is applied to the metal, using the *Newton's second law* one gets Eq. 2.26, where q is the elementary charge and P is the average momentum of the electron gas.

$$\frac{dP\left(t\right)}{dt} = -\frac{P\left(t\right)}{\tau} - qE\left(t\right) \tag{2.26}$$

Assuming $\mathbf{E}(t) = Re\{E_0 e^{-i\omega t}\}$, replacing P for the current density $\mathbf{j}(t) = (-e)n\mathbf{P}(t)/m_e$, where n is the number of free electrons and m_e is the electron mass, and using the *Fourier transform* one easily gets Eq. 2.27.

$$j\left(\omega\right) = \frac{nq^2}{m_e}\frac{1}{i\omega\tau - 1}E\left(\omega\right) \tag{2.27}$$

The relative permittivity follows from solving *Maxwell equations* in Eq. 2.28, where ε_0 is the vacuum permittivity, γ is the damping rate ($\gamma = \tau^{-1}$) and $\omega_p = \sqrt{\frac{nq^2}{\varepsilon_0 m_e}}$ the *plasma frequency* (usually in the ultraviolet spectrum for most metals).

$$\varepsilon_m = 1 - \frac{nq^2}{\varepsilon_0 m_e}\frac{1}{\omega^2 - i\omega\gamma} = 1 - \frac{\omega_p^2}{\omega^2 - i\omega\gamma} \tag{2.28}$$

Attending to Eq. 2.28 (by neglecting the losses) and knowing that $k^2 = \frac{\omega^2}{c^2}\varepsilon_m$, the system's dispersion found in Eq. 2.29 is easily achieved. Furthermore, it is verified that the transverse and longitudinal propagation modes are supported for frequencies above the plasma frequency and at ω_p, respectively. The longitudinal modes correspond to having $\varepsilon_m = 0$ (for a thorough analysis consult [31]). Figure 2.1 illustrates the dispersion curves for the transverse and longitudinal propagations, as well as the plot of the real and imaginary permittivity predicted by *Drude's model*.

$$\omega = \sqrt{c^2k^2 + \omega_p^2} \tag{2.29}$$

Drude's model suffices as an initial approach since it explains the principal properties inherent of metal response to excitations. However, there are more accurate approaches as the *Linhard dielectric response* (examined in [32]) and the ones done via a quantum analysis of the system, where interactions between particles and plasmon dispersion are accounted. The neglect of interband transition of electrons also contributes to inaccuracies in this model.

2.2.3 Volume Plasmons

The volume or bulk plasmons appear when radiationless oscillations of single electrons become coherent and start to act as an electron gas. Therefore, instead of the individual electrons dielectric response analysis (as presented in *Drude's model*), one ought to consider the motion of a gas with mass $M = m_e nV$ with V being the volume where the plasmons are confined.

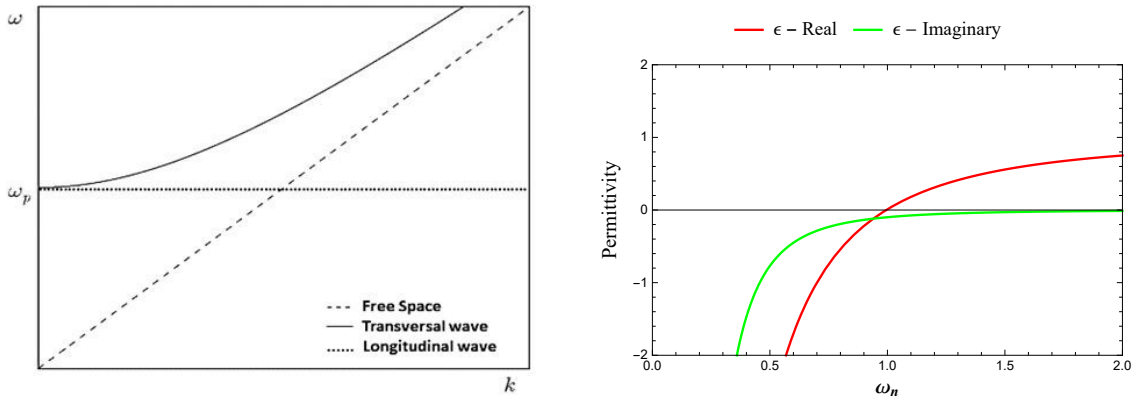

Figure 2.1: 1.a) Dispersion of k for *Drude's model* containing the transverse and longitudinal propagation modes. b) Plot of real and imaginary permittivity [1].

In these circumstances and assuming a charge displacement $\vec{u}$ in a bulk, as observed in Figure 2.2, an electric field will be generated such that $E = -q\frac{n\vec{u}}{\varepsilon_0}$ (by the *Electrical Gauss law*). By *Newton's law*, a force $\vec{F}$ is produced as shown in Eq. 2.30, from which Eq. 2.31 may also be derived.

$$\vec{F} = M\frac{d^2\vec{u}}{dt^2} = \frac{q}{m_e}M\vec{E} \tag{2.30}$$

$$\frac{d^2\vec{u}}{dt^2} = -\omega_p^2\vec{u} \tag{2.31}$$

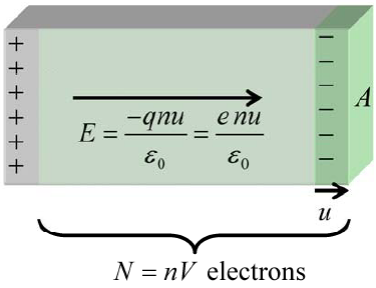

Figure 2.2: Plasma oscillation in a bulk [2].

The latter equation confirms that volume plasmons arise from collective longitudinal electron oscillations at the plasma frequency, which are rather characterized by the oscillation in the exchange between electrostatic and kinetic energy. Due to the vanishing magnetic field (and *Poynting vector*) the bulk plasmons do not couple to transverse electromagnetic fields and, therefore, they cannot be excited by radiation. An alternative solution is either by electron collision or using the *Cherenkov effect* to transfer energy to single electrons.

2.2.4 Surface Plasmons

The surface plasmons are defined as the quanta of charge oscillations that are extremely confined on the interface between a metal and a dielectric as represented in Figure 2.3. When there is a coupling between these confined plasmons and polaritons (i.e., polarization waves from a dielectric) this phenomenon is called surface plasmon-polaritons (SPP). Moreover, this coupling is mediated by an electromagnetic field.

To analyze the dispersion of SPP waves [1] one must solve *Maxwell equations* at the metal-dielectric interface for a homogeneous solution, i.e. a solution that is supported without external excitation. Considering the coordinates of Figure 2.3, the surface plasmon wave is characterized by a TM mode ($\vec{H}$ propagating along $\vec{y}$ and

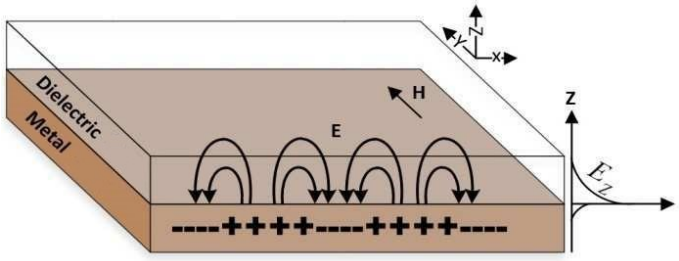

Figure 2.3: Dielectric-metal interface scheme with SPP propagation [3].

$\vec{E}$ along $\vec{x}$ and $\vec{z}$), which must exponentially decay along $\vec{z}$ either for above or below the interface, since the wave is highly confined to the interface. It is worth to mention that, depending on the chosen coordinate system, $\vec{k_y}$ may be not null, from where is useful to define the wavenumber $k_{\parallel} = \sqrt{k_x^2 + k_y^2}$.
However, in this scenario $\vec{k}$ is composed by $\vec{k_x}$ (sinusoidal propagation) and a $\vec{k_z}$ (exponentially decaying propagation). It is straightforward to check that from the *Maxwell equations* these wavevectors must obey to Eq. 2.32, where the subscript j stands for either the metal or dielectric medium.

$$k_x^2 + k_{z,j}^2 = \varepsilon_j \frac{\omega^2}{c^2} \tag{2.32}$$

By boundary conditions inspection, k_x may also be written as Eq. 2.33 and it can also be verified that such propagations occur only if ε_m and ε_d have opposite signals [33]. For common dielectrics, ε_d takes positive values, and consequently, ε_m ought to be negative. Since k_x must be real to allow sinusoidal modes and ε_m is given by Eq. 2.28, then the only possible solution exists for $\varepsilon_m(\omega) < -\varepsilon_d(\omega)$. To find the upper allowed frequency one must solve $\varepsilon_d + \varepsilon_m(\omega_{sp}) = 0$, which neglecting the damping term γ leads to the surface plasmon frequency $\omega_{sp} = \frac{\omega_p}{\sqrt{1+\varepsilon_d}}$.

$$k_x = \frac{\omega}{c}\sqrt{\frac{\varepsilon_d \varepsilon_m}{\varepsilon_d + \varepsilon_m}} \tag{2.33}$$

Figure 2.4 shows the dispersion curves for the SPP in contrast to the bulk plasmon's and the photon's (in the dielectric) dispersion.

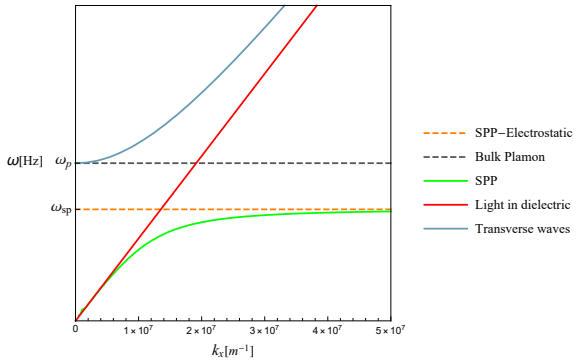

Figure 2.4: Dispersion curves of the photons in the dielectric, the transverse modes in the metal, the bulk plasmons and the e plasmons, where for the e plasmons the convergence frequency is ω_{sp}.

The SPP wavevector is always greater than the photons wavevector in the dielectric, which means that the e plasmon cannot be excited through direct incident radiation. This can be overcome by coupling light through a material (*e.g.* a prism) with a higher refraction index in a *Kretschmann* or *Otto configuration* [8], which are described in Figure 2.5.

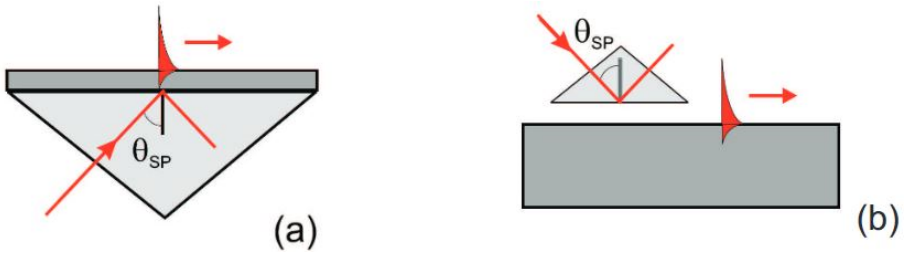

Figure 2.5: Prism coupling: (a) *Kretschmann configuration*, (b) *Otto configuration* [4].

These methods explore the total reflection mechanism of the incident light, where besides the reflected wave also an evanescent wave is transmitted towards the dielectric-metal interface. Moreover, being $\vec{k_0}$ the wavevector of the incident light, then the wavevector of the refracted radiation which is parallel to the interface (corresponding to the evanescent wave) is given by $\vec{k_{\|}} = n\vec{k_0}\sin(\theta)$. Consequently, for some refraction indexes (n) and angles (θ) combinations it is obtained $k_{\|} = nk_0\sin(\theta) = k_{sp}$, which enables the plasmon coupling via the evanescent wave. In fact, for the excitation frequency of SPP, the power associated with the reflected wave abruptly decreases and almost all the energy is coupled into the SPP.

In summary, metals support: surface plasmon waves for frequencies below the plasmon frequency; volume plasmons at frequencies near the plasma frequency; TEM propagation modes for frequencies above ω_p.

The metals optical properties are the source of some applications further discussed and in fact, they vary with the frequency associated to the incident radiation. Furthermore, for frequencies below ω_p the electrons in the metal bulk tend to reflect the radiation (opaque behavior) since the wave has difficulties penetrating the metal (due to the evanescent wave). In contrast, for high frequencies (above ω_p) the metal becomes more transparent due to the incapacity of electrons to screen the electromagnetic wave. These behaviors allow explaining the characteristically shinning properties of metals, since the plasma frequency typically takes values in the ultraviolet spectrum. Moreover, the energy absorption is enhanced at plasma frequency.

As λ is inversely proportional to k, the wavelength of SPP is smaller than the one of an electromagnetic wave propagating on a dielectric, which is an interesting feature to leverage on radiation confinement at electronics fields.

2.2.5 Short and Long-Range Plasmons

Since the permittivity on metals has a complex nature, then k_x will also come complex. Thus, it will occur a damping phenomenon in $\vec{x}$ direction, which leads to a characteristic propagation length given by Eq. 2.34.

$$\delta_{SP} = \frac{1}{2\mathrm{Im}\left(k_x\right)} \tag{2.34}$$

However, if the metal thickness (measured on $\vec{z}$ coordinate) is small enough, and is separated by dielectric substrates at both sides, then two evanescent waves associated with both interfaces may be supported. In this case, the magnetic interaction between the two interfaces cannot be neglected and the SPP dispersion will be strongly modified such that the coupling of the two waves must be taken into account. Considering a symmetrical environment, this coupling will produce two different frequencies for the SPP waves (hybridization). The lower (ω_-) mode, also called short-range SPP, corresponds to a symmetric electric field distribution, while for the higher (ω_+) frequency the fields have antisymmetric profile (see Figure 2.6) and the respectively propagating mode is designated long range SPP.

The frequencies, considering the dielectrics permittivity approximately 1 (for the air medium), are defined in Eq. 2.35 where d represents the thickness of the film metal.

$$\omega_{\pm} = \omega_{sp}\sqrt{1 \pm e^{-k_x d}} \tag{2.35}$$

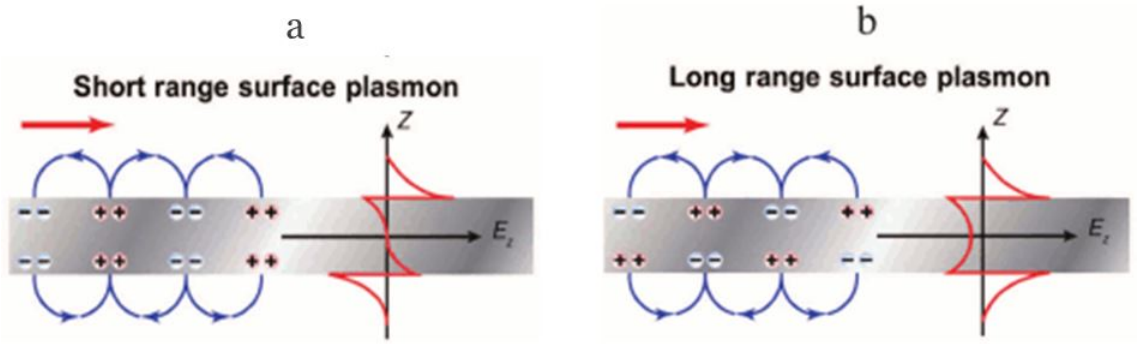

Figure 2.6: Plasmon excitation – a) Symmetric field profile in short range surface plasmon. b) Antisymmetric field profile in short range surface plasmon [5].

For long-range SPP, the imaginary wavevector term decreases quadratically with the decreasing of metal thickness, thus, by Eq. 2.34 the propagation length increases, which explains the mode designation.

The dispersion curves of even and odd modes for a silver layer with thicknesses of $100nm$ and $50nm$ are presented in Figure 2.7, where one is able to note that as the thickness of the metal slab decreases the more the curves are approximated by usual SPP curve dispersion [6].

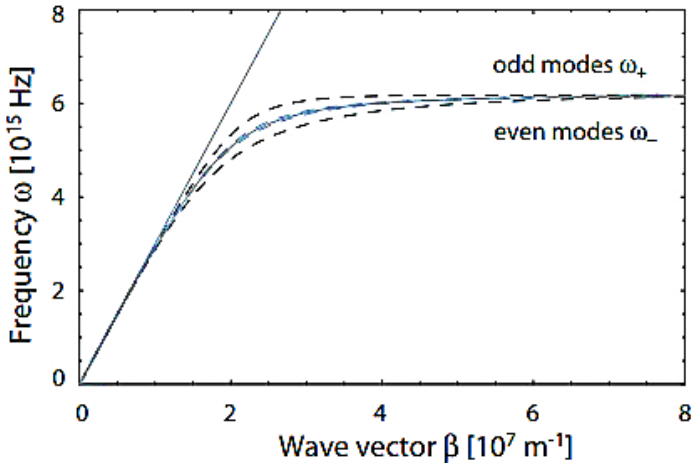

Figure 2.7: Dispersion curves of the coupled odd and even modes for an air-silver-air multilayer with a metal core of thickness $100nm$ (dashed gray curves) and $50nm$ (dashed blue curves) [6].

The applications on waveguides are explored because of the confinement level of the wavelength. Although the previous analysis, there were not accounted the leaky modes and the coupling between the SPP that is significantly modified by the difference in the two dielectric layers, which inevitably leads to losses.

2.2.6 Local Plasmon

For metal nanoparticles another plasmonic excitation appears associated with a non-propagating plasmon, which is named localized surface plasmons (Localized Surface Plasmons (LSP)). The phenomenon is identical to the discussed volume plasmons when the dimensions of these particles are about the range of the penetration depth (in the metal). The metal nanoparticles are involved in a dielectric (*e.g.*, a glass) in order to be excited by an evanescent wave, similarly to the discussed excitation of the SPP.

In the presence of an external electric field, as represented in Figure 2.8-a), the electrons move in the opposite direction of that field (trying to cancel the field inside the nanoparticle), while the positive ions stay steady, thus creating an opposite electric field (*Lenz's law*). For a time-varying electric field with a given frequency, the electrons will try to follow (oppositely) its movement This generates the local plasmon oscillation that has a

stronger response for the plasma frequency (resonance frequency), which is usually in the visible or infrared spectrum. The system also contains losses due to some electrical resistance.

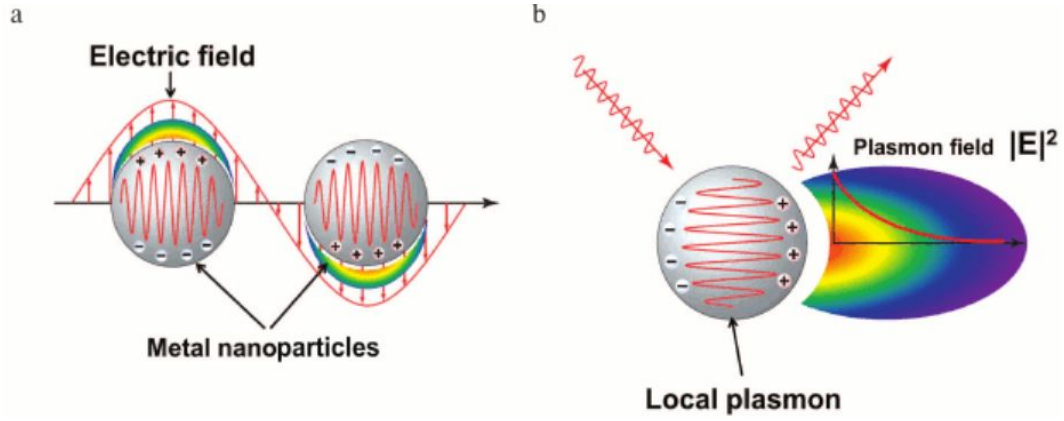

Figure 2.8: a) LSP excitation by electric field. b) Field intensity distribution for a local plasmon around the nanoparticle [7].

Detailed analysis for the physical model description of plasmon resonance in a small spherical particle can be consulted here [8]. The results show that the absorption and scattering of incident light in the particles is highly dependent on its radius a, more specifically they scale with a^3 and a^6, respectively. Then, for small particles, absorption is the dominant mechanism while for larger particles it will be the scattering. This is the main feature that enables the detection of metal nanoparticles, which are used as labels in biological samples. The size variation of the metal nanoparticles leads to a resonant scattering power shift in terms of the wavelength, which is perceptible for some metals, such as gold and silver, because these shifts occur in the visible spectrum. Increasing the surrounding dielectric permittivity also provokes a redshift on the scattering cross-section for spherical particles (represented in Figure 2.9 for gold and silver nanoparticles).

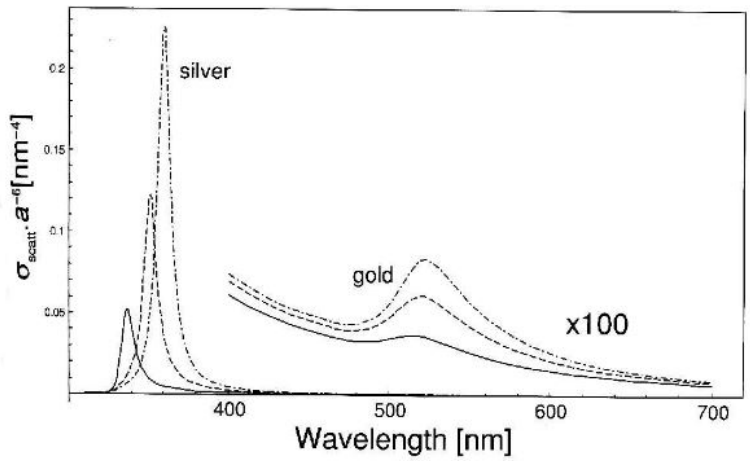

Figure 2.9: Plots of the scattering cross-section of spherical Ag and Au particles in different environments normalized by a^6 (a: particle radius). Solid line: vacuum, $n = 1$, dashed line: water, $n = 1 : 33$, dash-dotted line: glass, $n = 1 : 5$ [8].

Similarly, to the bulk plasmons, LSP are described not just by an effective electron mass but also by the morphology and charge density of the particle. In fact, even before the study and comprehension of this phenomenon, already in the fourth century AD was produced the *Lycurgus Cup* (Figure 2.10) by the Romans, which employed the concepts behind local plasmons. The inclusion of variable sized gold nanoparticles in the glass provided a green color to the *Lycurgus Cup* when observing the reflecting light in the cup and a red color when attending to the transmission radiation.

Figure 2.10: The *Lycurgus Cup* 4th century AD appears green when lit from the front and red when lit from the back [9].

Multi-resonant frequencies can appear in nanoparticles with complex geometries, which may be seen as the consequence of hybridizations of elementary plasmons with simpler structures.

2.2.7 Applications

Biosensors

As seen for local plasmons, the resonant scattering power is sensible to dielectric constant changes of the environment which allows their use in biological and chemical sensing and detection applications [8]. Therefore, by inserting metal nanoparticles into a biological sample, it is possible to measure the occurred shifts on the resonance frequency associated with certain chemicals and molecules. The nanoparticles morphology may be adapted for a better identification of a given molecule. Nevertheless, surface plasmon sensors are also a viable option in environmental changes detection for very short distances from the surface interface. Regarding the precision of an SPP in a *Kretschmann configuration*, it can be detected the effects (a shift) on the reflectivity for particle' sizes of a few nanometers' order, *e.g.*, it can be measured the effect produced by a $3nm$ layer of water adsorbed on a $53nm$ silver film [1]. The Figure 2.11 shows the scheme of a sensor used to measure the adsorption of a biological compost in a *Kretschmann configuration*.

Another example is the detection of malicious cancer cells by injecting a substance composed by a dielectric core and metal shell into the patient body. There occurs a bonding between these particles and the cancer cells, which enables to localize with a high precision the malicious cells via laser incident radiation. Lastly, the laser kills the cells by heating them up.

Spectroscopy

Another possible application of plasmons lies on *Raman scattering spectroscopy* [1], used to identify the chemical composition of a sample since the molecular vibrations energy spectrum provide a fingerprint-like characteristic. The *Raman scattering effect* is analogous to a modulation (as in telecommunications) where a time-harmonic optical field (*e.g.* monochromatic light) behave like a carrier that is modulated by the molecular vibrations (phonons). This process results in scattered radiation that suffers a frequency shift correspondent to the frequencies associated with the molecular oscillations. The uniqueness of the originated spectrum is related to the dependence of the molecular vibrations in its particular molecular structure (for a detailed description consult [34]).

The *Raman scattering* is an extremely weak effect when comparing to other effects and therefore the SPP

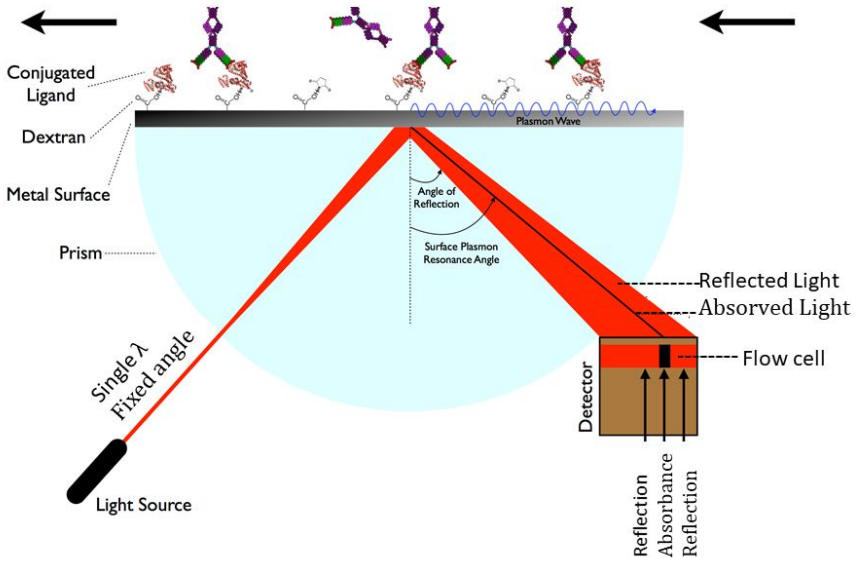

Figure 2.11: Biosensor scheme based on a *Kretschmann configuration* using SPP, based on [10].

emerge in the picture with the purpose of enhancing the strength magnitude regarding the light and molecules' interactions. Surface enhanced *Raman scattering* (SERS) is an example of a technique using surface plasmons and although the prominent results that have been achieved using this technique, it still does not exist a satisfactory explanation for the observed enhancement magnitudes (where 10^{12} magnitudes can be achieved).

Imaging with Super Lens

Consider a given source, which may be decomposed in spatial harmonics, radiating towards a plane of interest. The conventional optical systems usually have a maximum for the resolution that can be achieved, and which is associated with a fixed frequency radiation. This constraint comes from the *Sommerfeld* radiation condition and it is known as *Rayleigh diffraction limit*. It imposes a maximum spatial resolution of $\Delta_{min} = \frac{2c}{f}$ attained for a source radiation with frequency f. This condition cannot be surpassed even if resorting to optical lenses.

However, in 2000, John Pendry proposed a solution for this problem based on SPP excitation which allowed the coupling between the evanescent near-field of a source and the surface plasmons. Since the cause of the Rayleigh diffraction limit is associated with the fading of the source evanescent near-field, this coupling stands as the key for breaking this limit. Attending to Figure 2.12-a), it is possible to demonstrate, using even and odd plane wave excitation modes (consult [2] for better understanding), that at certain conditions the transmission coefficient of the incident wave comes as in Eq. 2.36 and the reflected field vanishes.

$$T = e^{\gamma_0 d} \tag{2.36}$$

These conditions are satisfied by using the plasmon frequency ω_{sp} as the working frequency (so that $\frac{\varepsilon_0}{\varepsilon_m} \approx -1$) and also by making $\gamma_m \approx \gamma_0$ (which are the propagation constants of the evanescence waves in metal and air, respectively), that is verified in silver for $|k_x| > k_0$ slabs for $||k_x||/k_0 \gg 1$.

Eq. 2.36 indicates that the near-field is enhanced within the silver slab and since the reflection coefficient disappears, the wave fading again exponentially when exiting the metal towards the air (illustrated into Figure 12-b)). If $d_1 + d_2 = d$, the exponential growing cancels the exponential decaying, thus, the transmitted wave at the image plane will be identical to the one from the object plane, which in theory allows extremely high resolutions. The approximations made are translated in inaccuracy for the results, which for the silver lenses case are as acceptable as smaller the distance d is in comparison to the wavelength. Hyperlens via anisotropic

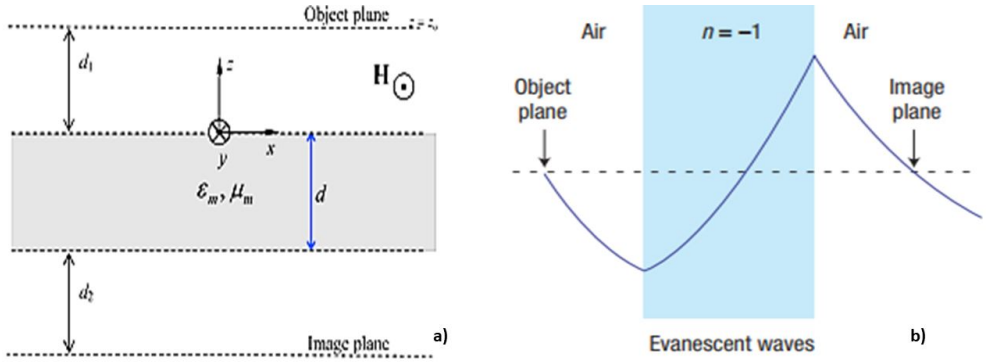

Figure 2.12: a) Imaging the near-field with super lens [2]. b) Evanescent wave enhancement for image formation at the image plane [11].

materials are also possible but are mentioned only as an informative element (for further analysis check [2] and [11]).

2.3 Useful Problems Formulations

2.3.1 Harmonic Oscillator

Beyond being completely solved by quantum and classical mechanics, the harmonic oscillator system is also a useful and powerful approach to solve some systems with time-dependent Hamiltonian. In fact, any system, where the state varies in time by a small amount relative to a steady configuration can be associated with a harmonic oscillator or an ensemble of decoupled harmonic oscillators. As in the classical example, where an object with mass m coupled to a string with constant force k, also the harmonic oscillator potential in quantum mechanics can be written as $V(x) = \frac{1}{2}m\omega^2 x^2$, where $\omega = \sqrt{\frac{k}{m}}$ is the classical harmonic oscillator frequency and x is the displacement relative to the equilibrium point. Therefore, the Hamiltonian of a Harmonic Oscillator follows as in Eq. 2.37.

$$\mathbf{H} = \frac{1}{2m}\mathbf{P}^2 + \frac{1}{2}m\omega^2\mathbf{X}^2 \tag{2.37}$$

The fact that **H** can be addressed in terms of the uncertainty relations is the reason for the next derivation of Harmonic Oscillator solutions. It is defined an operator $\hat{\mathbf{a}}$ in Eq. 2.38a and its adjoint $\hat{\mathbf{a}}^\dagger$ in Eq. 2.38b , which are designated by destruction or lowering operator and creation or raising operator, respectively. One should note that **X** and **P** are equal to their adjoint since they are Hermitian.

$$\hat{\mathbf{a}}^\dagger = \sqrt{\frac{m\omega}{2\hbar}}\mathbf{X} - i\sqrt{\frac{1}{2m\omega\hbar}}\mathbf{P} \tag{2.38a}$$

$$\hat{\mathbf{a}} = \sqrt{\frac{m\omega}{2\hbar}}\mathbf{X} + i\sqrt{\frac{1}{2m\omega\hbar}}\mathbf{P} \tag{2.38b}$$

These operators are introduced from the factorization method of the Hamiltonian. Thus **H** can be also expressed as represented in Eq. 2.39.

$$\mathbf{H} = \hbar\omega\left(\hat{\mathbf{a}}^\dagger\hat{\mathbf{a}} + \frac{1}{2}\mathbf{I}\right) \tag{2.39}$$

This representation allows to easily extract the commutation relations between the Hamiltonian and the annihilation operators (exhibited in Eq. 2.40b and Eq. 2.40a), which are of extremely importance when solving

systems containing electromagnetic fields.

$$[\hat{\mathbf{a}}, \mathbf{H}] = \hbar\omega\hat{\mathbf{a}} \tag{2.40a}$$

$$\left[\hat{\mathbf{a}}^{\dagger}, \mathbf{H}\right] = -\hbar\omega\hat{\mathbf{a}}^{\dagger} \tag{2.40b}$$

For a particle in the eigenstate $\vec{E}$ with energy E, if the lowering operator is applied and then measured the energy of the new configuration generated, is observed Eq. 2.41.

$$\mathbf{H}\hat{\mathbf{a}}\vec{E} = (\mathrm{E} - \hbar\omega)\,\hat{\mathbf{a}}\vec{E} \tag{2.41}$$

This result reveals that $\hat{\mathbf{a}}\vec{E}$ also solves the Schrödinger equation. Thus, it can be represented as a new eigenstate $\vec{E}_{E-\hbar\omega}$ with a lower energy than $\vec{E}$ (reason for which a is called the lowering operator).

Similarly, if the lowering operator was replaced by the raising operator, one would obtain Eq. 2.42, whereas unlike the previous scenario, the energy of the new eigenstate $\vec{E}_{E+\hbar\omega}$ is incremented of $\hbar\omega$ relatively to the one of $\vec{E}$.

$$\mathbf{H}\hat{\mathbf{a}}^{\dagger}\vec{E} = (\mathrm{E} + \hbar\omega)\,\hat{\mathbf{a}}^{\dagger}\vec{E} \tag{2.42}$$

Moreover, if the raising or the lowering operator is applied n times repeatedly on $\vec{E}$, the energy of the resultant eigenstates would be $\vec{E}_{E+n\hbar\omega} = E + n\hbar\omega$ or $\vec{E}_{E-n\hbar\omega} = E - n\hbar\omega$, respectively, which enables the construction of an infinite tower of allowed energies as shown in Figure 2.13. Although the energy is not bounded for high energies, the same does not happen for low energies, where there is a minimum positive value for the energy which is designed by ground state. Its associated energy is $E_0 = \frac{1}{2}\hbar\omega$ and can be easily determined by considering that a acting on the ground state will result on the null vector.

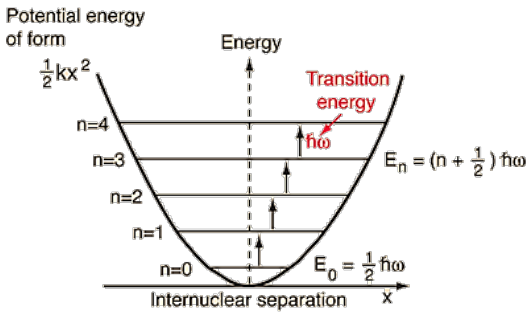

Figure 2.13: Energy states of a quantum harmonic oscillator of frequency ω [12].

Contrary to what was expected classically, the ground state energy is not zero, but instead a low positive value which is connected to the *Heisenberg uncertainty principle*. However, this does not impose any contradiction to the classical reality that one is accustomed. The reason is that the gaps between the consecutive discrete energies are so small in comparison to the measurements precision, that it seems like the energy allowed is continuous.

Consequently, the problem is solved without worrying about the position and momentum basis, since one may apply only the commutations relations presented above. The energy levels are spaced by uniform gaps of energy $\Delta E = \frac{1}{2}\hbar\omega$, a property that is explained by the raising and lowering operator nature. The wavefunctions $\psi_n(x)$ (correspondent to the n energy level) are obtained by solving the *Schrödinger equation* and are typically established in terms of the *Hermite polynomials* $\mathrm{H}_n(y)$ as perceived in Eq. 2.43.

$$\psi_n(x) = \left(\frac{m\omega}{\pi\hbar 2^{2n}(n!)^2}\right)^{\frac{1}{4}} e^{-\frac{mx^2}{2\hbar}}\,\mathrm{H}_n\left[\left(\frac{m\omega}{\hbar}\right)^{\frac{1}{2}}x\right] \tag{2.43}$$

In Figure 2.14 the behavior of $\psi_n(x)$ and of the density probability function ($||\psi_n(x)||^2$) are represented along the position coordinate for several energy levels including the ground state.

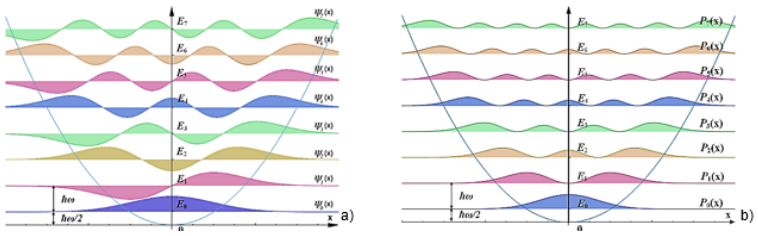

Figure 2.14: a) Wavefunctions of the harmonic oscillator for each energy level; b) Probability associated with each energy level eigenfunction [13].

The results of this problem will be of extreme importance when discussing the electromagnetic field characterization and its interactions with other systems (*e.g.*, atoms), where the potential $\mathrm{A}(r,t)$ assumes the role of $\mathbf{X}$ and $\mathrm{A}(r,t)$ is the velocity corresponding to the coordinate $\mathrm{A}(r,t)$. The electromagnetic field oscillations, similarly to the harmonic oscillator, are quanta and leave a ladder of allowed energy levels. This is useful in systems like the Hydrogen atom or electrons subjected to strong magnetic fields, wherein the latter the energy levels lead to the *Landau levels*.

2.3.2 Casimir Effect

The *Casimir force* [35, 36] is a phenomenon that cannot be explained by a classical approach and where the consequences of the quantized electromagnetic field are visible. The experiment considers two uncharged and perfectly conductor parallel plates (as in Figure 2.15). Casimir showed that it exists an attractive force between the two parallel plates very close to each other, even though they are not charged. This force is produced by a sort of radiation pressure on the plates by the virtual photons (vacuum fluctuations) that also originate the zero-point energy [29]. The attractive behavior results from pressure originated, that is weaker between the plates than outside that region. There exist also other phenomena that exhibit similar effects to *Casimir's* such as the case of plates drowned into colored water containing a *sonicator* or the case of two beads that are apart from each other on a string and that suffer an attractive force [37].

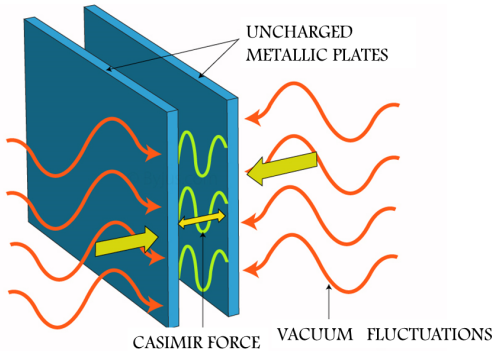

Figure 2.15: Casimir experiment scheme with to uncharged parallel metallic plates [14]

For the following derivation of *Casimir's force*, one must consider that the plates have a section area $S = L^2$, the direction $\hat{x}$ and $\hat{y}$ are the ones parallel to the plates and the $\hat{z}$ the perpendicular one. Moreover, the phenomenon may be understood by admitting that the presence of a metal or dielectric in the vacuum modifies the vacuum expectation value of the quantized electromagnetic field energy. Casimir also realized that for larger

distances between the plates the force grows weaker. To calculate this force, one may first compute the lowest energy associated with the system (zero-point energy). In the absence of external fields and since the cavity is perfectly reflective, the waves that propagate inside the cavity must be "trapped", and therefore only standing waves are accounted for the zero-point energy calculation. At each possible standing wave, an energy E_n is associated.

One easily confirms that due to the electric field vanishment at the conducting plates, its modes will present a structure represented in Eq. 2.44, where no amplitude term is considered and F is used instead of E because the latter is used to represent the energy.

$$F_n\left(x,y,z,t\right) = e^{-i\omega_n t} e^{i(k_x x + k_y y + k_z z)} \sin\left(k_n z\right) \tag{2.44}$$

Moreover, n represents the polarizations that can propagate inside the cavity, the wavevectors k_x and k_y are related by $\omega_n/c = \sqrt{\frac{n\pi^2}{2} + k_x + k_y}$, and the term $k_n = \frac{n\pi}{d}$ comes from the boundary condition referred, where d is the distance between plates. Considering the sum of all modes, the vacuum expectation energy is reached through Eq. 2.45.

$$\langle E \rangle = \sum_{n,p} \frac{\hbar}{2} c \sqrt{\frac{n\pi^2}{2} + k_x + k_y} \tag{2.45}$$

This sum inevitably diverges to infinity, and although it seems strange to have an infinite energy, in fact what can be physically measured are not energies but rather energy differences. Also, the energy depends on the shape of the cavity, and one may use the periodic boundary conditions to transform the sum above in an integral (Eq. 2.46)) representing the energy per area, where $d^2k = dk_x dk_y = (2\pi/L)^2$.

$$\frac{\langle E \rangle}{S} = \frac{1}{2} \frac{2\hbar}{(2\pi)^2} \int\int d^2k \sum_{n=1}^{\infty} \omega_n \tag{2.46}$$

The additional 2 factor appears in the formula to account with two possible wave polarizations (TE or TM).

However, the expression above still diverges to infinity and consequently it is introduced a regulator s that suppresses the higher frequencies, functioning as a low pass filter. Although this formulation may seem a little artificial and devoided of meaning, it can be argued that for very high frequencies any material (including the cavity) will transmit the wave rather than reflecting it. However other approaches involving the use of functional integrals may be employed to solve the above equation without introducing anything artificial.

Resorting to the regulator, the vacuum energy is written as in Eq. 2.47. Furthermore, the equation results in a finite energy only for $R_e\{\mathbf{s}\} > 3$. Also, the sum contains a pole for s=3, which may be analytically resolved by using the analytically continued technique at s=0, where the sum finite.

$$\frac{\langle E\left(\mathbf{s}\right)\rangle}{S} = \frac{\hbar}{(2\pi)^2} \int\int d^2k \sum_{n=1}^{\infty} \omega_n |\ \omega_n\ |^{-s} \tag{2.47}$$

Therefore, skipping the intermediate steps, that one may consult at [34], the final expression of the energy is given by Eq. 2.48, where $\zeta\left(x\right)$ is the *Riemann zeta function* used in the intermediate steps. Finally, the *Casimir force* per unit area is calculated deriving the energy with respect to the distance d, obtaining the formula in Eq. 2.49. This expression represents well why the force is incredibly weak, since the reduced Planck constant is very small, and therefore only for very short distances the effects of *Casimir force* are visible. The signal in the equation also explains the attractive behavior of the force.

$$\frac{\langle E \rangle}{S} = -\frac{\hbar c \pi^2}{6d^3} \zeta\left(-3\right) = -\frac{\hbar c \pi^2}{720 d^3} \tag{2.48}$$

$$\frac{F_C}{S} = -\frac{\partial}{\partial d} \frac{\langle E \rangle}{S} = -\frac{\hbar c \pi^2}{240 d^4} \tag{2.49}$$

2.3.3 Surface Plasmons Quantization

For the brief derivation of the fields quantization for the SPP system, it is considered the quasi-static regime, where the magnetic field is approximately zero ($B \approx 0$) and only the electric field is considered [38]. It is introduced the potential vector of the electric field modes ϕ_k (where each k is the wavevector correspondent to each mode), which is related with the electric field by $-\nabla\vec{\phi}_k = \vec{E}_k$. Thus, recalling the structure of the quantized electric field operator, discussed previously, one may write it down in terms of the electric potential as seen in Eq. 2.50.

$$\mathbf{E} = \sum_k \sqrt{\frac{\hbar\omega_k}{2}} \left(-\nabla\phi_k \hat{\mathbf{a}}_k - \nabla\phi_k^* \hat{\mathbf{a}}_k^\dagger\right) \tag{2.50}$$

To fully determine the electric field operator for the surface plasmons one needs to find an expression for $\vec{\phi}_k$. Manipulating *Maxwell equations* and considering a system without any external sources, one extracts the modal equation (Eq. 2.51).

$$\nabla \cdot (\varepsilon(\omega, z) \nabla\phi_k) = 0 \tag{2.51}$$

Evoking the evanescent propagation in $\hat{z}$ direction of the SPP wave and its characteristic TM polarization, the general solution for the modal equation is attained (in Eq. 2.52).

$$\phi_k(x, y, z) = e^{i(k_x x + k_y y)} \begin{cases} A_{1,k} e^{-k_\parallel z} & , z > 0 \\ A_{2,k} e^{k_\parallel z} & , z < 0 \end{cases} \tag{2.52}$$

The $k_\parallel$ is the wavevector parallel to the metal-dielectric interface, which must be determined as $k_\parallel^2 = k_x^2 + k_y^2$ so that Eq. 2.51 is observed.

Imposing the continuity of the electrical potential (i.e., $\phi(z = 0^-) = \phi(z = 0^+)$), comes that the amplitudes in both branches of the function have to be equal $A_k = A_{1,k} = A_{2,k}$. Another boundary condition required to verify is the continuity of the electric displacement component perpendicular to the plasmon surface, i.e., $\vec{D}$ or $\varepsilon\frac{\partial\phi}{\partial z}$ must be continuous. Consequently, noticing that $\varepsilon(z, \omega)$ is defined as ε_0 for $z > 0$ (dielectric substrate) and as $\varepsilon_m(\omega) = \varepsilon_0\left(1 + \frac{(\omega_p^2)}{\omega^2}\right)$ for $z < 0$ (metal substrate), it is straightforward to check that $\varepsilon_m(\omega) + \varepsilon_0 = 0$. The frequency that verifies this condition is surface plasmon frequency ω_{sp}.

In this case, one may recall by inspecting the dispersion curve at $\omega = \omega_{sp}$ that the density of modes is extremely high and consequently, the electric field can be decomposed as a sum over all possible k's. In addition, it must be chosen a normalization for the amplitude A_k, which in this case is given by Eq. 2.53 or more conveniently in Eq. 2.54, where is considered that the energy for each mode is one *Joule*. The n stands for the possible polarizations of the system and $d^3r = dxdydz$.

$$\langle E_{nk} | E_{nk} \rangle = \frac{1}{2} \int d^3r {E_{nk}}^* \cdot \frac{\partial[\omega\varepsilon(z, \omega)]}{\partial\omega} \cdot E_{nk} = 1 \tag{2.53}$$

$$|A_k|^2 \int d^3r\, k_\parallel^2\, e^{-2k_\parallel |z|} \frac{\partial[\omega\varepsilon(z, \omega)]}{\partial\omega} = 1 \tag{2.54}$$

The partial derivative term on the right side of Eq. 2.54 leads to $\varepsilon = 3\varepsilon_0$ and $\varepsilon = \varepsilon_0$ for the metal and air media, respectively. With everything fixed, it is now possible to use the normalization condition above to extract the value for A_k, which, for a metal slab with area $S = L_x L_y$, follows

The last step is done by replacing the electric potential obtained by Eq. 2.55 and Eq. 2.52 in the electric field operator. It is important to remark that all this formulation is carried away by associating the normal modes of the electric field to uncoupled quantum harmonic oscillators.

$$|A_k| = \sqrt{\frac{1}{2\varepsilon_0 k_\parallel S}} \tag{2.55}$$

Chapter 3

Non-local SPP

3.1 Classical Metal Response in Non-local Medium

3.1.1 Drift-Diffusion Model

The description of the plasmonic response to an external source is usually made with the assumption of a homogeneous charge distribution along the metal slab. In practice, when dealing with systems of a few nanometers size, the *Drude's* model is not the most adequate approach due to the outmatching results when compared with the experimental ones [39]. For a more acquainted description, certain mechanisms should be taken into account, such as the motion of single electrons and the repulsive Coulomb interactions between each other. These interactions provoke diffusion effects, which create a repelled motion of electrons from the areas with higher charge concentration as the case of the interface where charges are accumulated [40, 41]. An immediate implication of this charge nonlocality is that the value of the electric polarization in a specific position (due to an external electric field) is no longer solely determined by the response of that point, but also of its surrounding region. Consequently, this implies the introduction of a new electron's motion model for non-local media and the derivation of a dielectric spatial dispersive response [42].

Furthermore, the nonlocality may also be perceived as a macroscopic manifestation of the Pauli exclusion principle and the description of the electromagnetic properties in this kind of materials may be accomplished by using the *Hydrodynamic (or Drift-Diffusion) model* [39, 43]. Despite the existence of other approaches [44], such as the time-dependent density functional theory (TD-DFT) [45, 46] which allows a quantum description of collective excitations, their complexity is higher. In specific for the TD-DFT model, its dimensional regime of validation is comprised of sub-nanometer systems, which do not cover most of the Plasmonic applications.

Unlike the *Drude's* model where the current density does not have any spatial dependence, the *Drift-Diffusion* or *Hydrodynamic* model comprises this dependence in an additional term $\beta^2 \nabla \rho$ resulting in the Eq. 3.1.

$$\frac{\partial \overrightarrow{j}}{\partial t} = \varepsilon_0 {\omega_p}^2 \overrightarrow{E} - \gamma \overrightarrow{j} - \beta^2 \tag{3.1}$$

Here, ρ is the density charge and $\beta^2 = \left\langle v^2 \right\rangle = \frac{3}{5} {v_F}^2$ is a term that indicates the strength of the nonlocality, being v_F the Fermi-velocity of the electron gas [2]. The methods used to represent the electrons response are usually based on Boltzmann theory and the *Navier-Stokes equation* [41]. Another very common method to include the spatial dispersion of the medium is the *local analogue method* (*LAM*), which can reproduce results with a good level of precision, by replacing the non-local metallic surface with an effective local metallic surface coated with a dielectric layer.

The procedures undertaken hereinafter to achieve a closed expression for the permittivity on non-local metals are the same as followed at [2, 47]. One may foresee that in the static limit ($\frac{\partial \overrightarrow{j}}{\partial t} = 0$), the current is given by

$\overrightarrow{j} = \frac{\varepsilon_0 \omega_p^2}{\gamma}\overrightarrow{E} - \frac{\beta^2}{\gamma}\nabla\rho$, where the first term in the right side of the equation represents the drift current and the second one is associated with the diffusion current [2]. However, $\frac{\partial \overrightarrow{j}}{\partial t}$ is in general non-trivial Thus, to solve the differential equation it is often assumed that the solution can be decomposed in planar waves of the form $\overrightarrow{E} \sim e^{i(\overrightarrow{k}\cdot\overrightarrow{r}-\omega t)}$ for the different possible wave vectors $\overrightarrow{k} = (k_x\widehat{x};\ k_y\widehat{y};\ k_z\widehat{z})$ [48]. Consequently, it follows that $\nabla = i\overrightarrow{k}$ and $\frac{\partial}{\partial t} = -i\omega$, which combined with the continuity equation 3.2.

$$\frac{\partial \rho}{\partial t} + \nabla \cdot \overrightarrow{j} = 0 \tag{3.2}$$

Substituting this result in the *Hydrodynamic* equation one obtains

$$\omega(\omega + i\gamma)\overrightarrow{j} - \beta^2 \overrightarrow{k}(\overrightarrow{k} \cdot \overrightarrow{j}) = i\omega\varepsilon_0 {\omega_p}^2 \overrightarrow{E} \tag{3.3}$$

One may also rewrite the latter equation in a matricial notation, as $\mathrm{M}\ \overrightarrow{j} = i\omega\varepsilon_0 {\omega_p}^2 \mathrm{I}\ \overrightarrow{E}$ being $\mathrm{M} = \omega(\omega + i\gamma)\,\mathrm{I} - \beta^2 \vec{k}\otimes\vec{k}$. Moreover, simply by matrix inversion one may define the electric density current in terms of the electric field (Eq. 3.4).

$$\overrightarrow{j}(k,\omega) = i\omega\varepsilon_0 \frac{{\omega_p}^2}{\omega(\omega + i\gamma)} \left[\mathrm{I} - \frac{\overrightarrow{k}\otimes\overrightarrow{k}}{\overrightarrow{k}^2 - \frac{1}{\beta^2}\omega(\omega + i\gamma)}\right] \cdot \overrightarrow{E} \tag{3.4}$$

Investigating now the Ampere law in the spatial spectral domain it comes as $\nabla \times \overrightarrow{H} = \overrightarrow{j} - i\omega\varepsilon_0 \overrightarrow{E}$. Moreover, invoking the relation between the density current with the electric field in 3.4, the same equation can be reformulated as $\nabla \times \overrightarrow{H} = -i\omega\widehat{\varepsilon}(k,\omega)\overrightarrow{E}$, where the current density may be accounted in the phenomenological tensorial permittivity $\widehat{\varepsilon}(k,\omega)$ as a polarization susceptibility response whose expression is

$$\widehat{\varepsilon}(k,\omega) = \varepsilon_0 \left[\mathrm{I} - \frac{{\omega_p}^2}{\omega(\omega + i\gamma)} \left[\mathrm{I} - \frac{\overrightarrow{k}\otimes\overrightarrow{k}}{k^2 - \frac{\omega(\omega+i\gamma)}{\beta^2}}\right]\right] \tag{3.5}$$

One may further notice that if the diffusion is negligible ($\beta \to 0$) the *Drude's* permittivity is once again recovered. However, in the literature [49] one may find a slightly different expression for the permittivity tensor containing a term ε_∞ [50] multiplying by the first identity matrix in Eq. 3.5. The term ε_∞ portrays the properties of the dielectric response of the bound valence electrons in the metal at high frequencies, excluding the conduction electrons [6]. In some approaches, such as in [51], this term (ε_∞) also accounts with the inter and intraband transitions in the metal, in order to achieve a permittivity description with higher accuracy when compared with the experimental data.

For a better perception of the consequences of a non-local dielectric response, the electric displacement may be computed in the spatial domain, which in practice corresponds to the convolution in Eq. 3.6.

$$\overrightarrow{D}(r,\omega) = \int\int\int d^3r' \widehat{\varepsilon}(r - r') \cdot \overrightarrow{E}(r') \tag{3.6}$$

It is clear from the Eq. 3.7, that in contrast with a local permittivity, from where only a Dirac's delta term appears, the non-local one contains an extra term.

$$\widehat{\varepsilon}(r) = \varepsilon_0 \left(1 - \frac{{\omega_p}^2}{\omega(\omega + i\gamma)}\right)\delta(r) - \frac{\varepsilon_0 {\omega_p}^2}{\omega(\omega + i\gamma)}\nabla\nabla\left(\frac{e^{i\sqrt{\omega(\omega+i\gamma)}r/\beta}}{4\pi r}\right) \tag{3.7}$$

Moreover, this term as a non-zero contribution in the vicinity $|r - r'| > 0$ of the position of interest r, decaying as the distance increases. This effect is pictured in Figure 3.1.

Another consequence of the diffusion is the enhancement of fields penetration induced by charges at the surface of a metal.

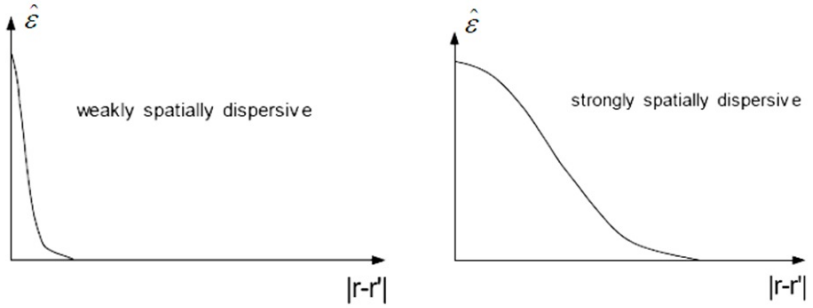

Figure 3.1: Permittivity contribution in terms of the spatial range from the position of interest for weakly (left image) and strong (right image) spatial dispersion. The Dirac's impulse widens as much as the nonlocality effects become stronger [2].

3.1.2 Transverse and Longitudinal Propagation modes

This section pretends to understand how the spatial dispersion affects the electromagnetic fields within the metal and its surface. Also, it compares the major modifications in the dispersion curves regarding its analogous in a local metal.

It will be of interest to determine the natural propagating modes present in a non-local metal slab. Considering plane waves propagating, the possible modes can either be transverse or longitudinal. In the case of the former, by defining $\overrightarrow{E_T}$ and ε_T as the components of the electric field and the permittivity, respectively, perpendiculars to the wave vector ($\overrightarrow{k}$), the electric displacement may simplify into a direct multiplication , *i.e.*, $\overrightarrow{D} = \widehat{\varepsilon} \cdot \overrightarrow{E_T} = \varepsilon_T \overrightarrow{E_T}$. The transverse permittivity ε_T is given by Eq. 3.8 and it already contains the term ε_∞ addressed previously.

$$\varepsilon_T(\omega) = \varepsilon_0 \left(\varepsilon_\infty - \frac{{\omega_p}^2}{\omega(\omega + i\gamma)} \right) \tag{3.8}$$

In this scenario, it is interesting to note that the spatial dispersion does not affect the propagation of transverse waves when comparing to a similar local medium. Thus, the dispersion is the same as in the *Drude's* model.

An analogous simplification occurs in the computation of the electric displacement for the longitudinal modes of the electric field ($\overrightarrow{E_L}$) as $\overrightarrow{D} = \widehat{\varepsilon} \cdot \overrightarrow{E_L} = \varepsilon_L \overrightarrow{E_L}$. The longitudinal permittivity is denoted by ε_L and its expression, that is now also a function of the $\overrightarrow{k}$, is found in the Eq. 3.9.

$$\varepsilon_L(\omega, \overrightarrow{k}) = \varepsilon_0 \left(\varepsilon_\infty - \frac{{\omega_p}^2}{\omega(\omega + i\gamma) - \beta^2 \overrightarrow{k}^2} \right) \tag{3.9}$$

Hence, the permittivity contains contributions of both propagation's modes such that its interdependence is given by Eq. 3.10.

$$\widehat{\varepsilon}(\omega, \overrightarrow{k}) = \varepsilon_T \left(I - \frac{\overrightarrow{k} \otimes \overrightarrow{k}}{\overrightarrow{k}^2} \right) + \varepsilon_L \frac{\overrightarrow{k} \otimes \overrightarrow{k}}{\overrightarrow{k}^2} \tag{3.10}$$

Moreover, it is evident the implicit dependence of the diffusion effects on the longitudinal permittivity through the term $\beta^2 \overrightarrow{k}^2$, which implies, in contrast with the local scenario, that the bulk plasmons admit radiation fields (non-null Poynting vector S) even though the magnetic field is approximately zero [2]. In turn, the dispersion of the bulk plasmons will be consequently modified, more precisely by setting $\varepsilon_L(\omega, \overrightarrow{k}) = 0$ (condition for longitudinal waves admittance in the scenario where $\nabla \cdot \overrightarrow{D} = 0$), which produces the following dispersion equation

$$k_{\parallel,l} = \pm\sqrt{{k_x}^2 + {k_y}^2 + \frac{\frac{{\omega_p}^2}{\varepsilon_\infty} - \omega(\omega + \iota\gamma)}{\beta^2}} \tag{3.11}$$

In the latter expression, it is assumed that the $\hat{z}$ component of the wave vector is imaginary (*i.e.* $k_z = ik_{\parallel,l}$), due to the known evanescence behavior of surface plasmons. The signal choice stays unequivocally determined, accordingly to the direction of wave attending to its intrinsic decaying behavior.

3.1.3 Additional Boundary Conditions

Another problem arises when introducing an interface formed by a local and spatial dispersive medium, because of the indetermination on the characterization of the propagation waves, when using the Maxwellian Boundary Conditions (MBC). Therefore, no longer suffices to impose the continuity of the tangential E and H fields. The interpretation behind this problem lies on the allowed number of polarization states per $(\omega, \overrightarrow{k})$, which may be greater than two (the typical for local media). This is intimately related to the degrees of freedom in dispersive materials manifested through material internal variables such as the current $\overrightarrow{J}$ and charge density ρ, which require a boundary condition at the interface. In fact, for the case of a metal-dielectric interface, there are three polarizations: two transverse and one longitudinal to the interface (for a deeper understanding consult [2]).

This fact envisages that to solve the boundary value problem for a non-local medium it must be applied Additional Boundary Conditions (ABC) [52]. Nevertheless, an issue remains related with the correct ABC's choice, since it does not exist a general formulation to derive the suitable ABC for a given system. Instead, an *ad hoc* study towards a specific system must be conducted in order to find a correct ABC. There is some controversy regarding to what ABC should be used in certain scenarios [52].

For a dielectric-metal interface context, the additional condition was already subject of a detailed study [21, 52, 53], where the two most recognized approaches are either when the normal component of the current $\overrightarrow{J}$ vanishes at the surface or when the electric field $\overrightarrow{E}$ is assumed to be continuous. These two conditions coincide in the case where the local dielectric is vacuum. The reasoning behind the first approach is supported by the fact that, neglecting the bound charges, the current should not spill out from the metal interface. While the second one is justified by assuming that the fields vary smoothly at the interface. One should be aware that the correct condition should be only the vanishing of the free electrons current at the interface $\overrightarrow{J_f}\Big|_{z=0} \cdot \hat{n} = 0$.

For the case under study (a metal-dielectric interface), the continuity of $\overrightarrow{D}$ at the interface (from the MBC), together with the ABC $\overrightarrow{J}\Big|_{z=0} \cdot \hat{n} = 0$, yield to the condition 3.12, where ε_b is the dielectric response that includes the vacuum and the bound charges contribution at the metal, and that for the present case is equal to ε_∞.

$$\varepsilon_b \overrightarrow{E}(z = 0^-) \cdot \hat{n} = \varepsilon_d \overrightarrow{E}(z = 0^+) \cdot \hat{n} \tag{3.12}$$

This is ensured by the constitutive correlations: $\overrightarrow{D} = \varepsilon \overrightarrow{E} + \frac{\overrightarrow{J}}{-i\omega}$ in the metal region and $\overrightarrow{D} = \varepsilon_d \overrightarrow{E}$ in the dielectric.

Further on, regarding the boundary conditions, the methodology employed is the same one followed at [2, 21] .

3.2 Electromagnetic Field in Quasi Static Approximation

3.2.1 Dispersion

A similarly work to the one developed throughout section 2.3.3 takes place hereafter, where the quantization of the Electromagnetic field modes are reproduced, now accounting with the diffusion effects.

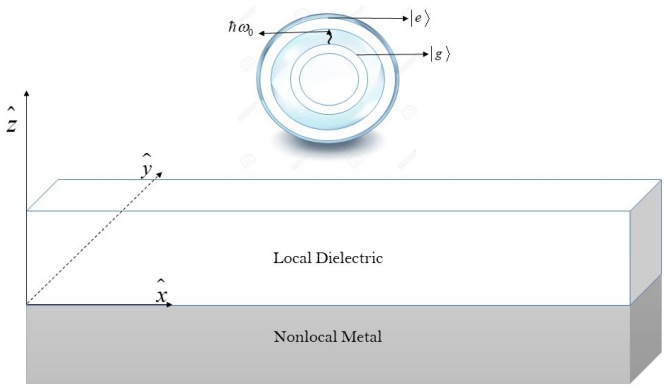

Figure 3.2: System under study: non-local surface plasmon in the vicinity of a two-level quantum object, e.g., a two-level hydrogen atom or a quantum dot.

Once more, this is attained by considering an electrostatic regime ($\nabla \times \overrightarrow{E} \approx 0$ and $H \approx 0$), which is a reasonable approximation for wavelengths greater than the distances involved in the system. The schematic of the system is represented in Figure 3.2. Bearing in mind that it can be introduced an electric potential ϕ, such that $\overrightarrow{E} = -\nabla\phi$, and that no external charges are contemplated ($\nabla \cdot \overrightarrow{D} = 0$), it follows

As seen before, the analysis is simplified by expanding the electric potential in planar waves with the form $\phi \sim e^{i(\overrightarrow{k}\cdot\overrightarrow{r}-\omega t)}$. Hence, in the dielectric substrate Eq. 3.13 yields to $(\overrightarrow{k} \cdot \overrightarrow{k})\varepsilon_D\phi = 0$, which is equivalent to say that only transverse waves are allowed, *i.e.*, $(\overrightarrow{k} \cdot \overrightarrow{E} = 0)$.

$$\nabla \cdot (\widehat{\varepsilon}(\omega, \kappa) \cdot \nabla\phi) = 0 \tag{3.13}$$

From the latter condition and since the waves propagating perpendicularly to the interface are evanescent, the propagation constant k_z is imaginary such that $k_z = ik_\parallel$, where $k_\parallel = \sqrt{k_x^2 + k_y^2}$ is a real number. In the metal layer, besides the transverse solution $\overrightarrow{k^2} = 0$, a longitudinal wave solution also appears $\varepsilon_L(\omega, \overrightarrow{k})\phi = 0$, which, as seen previously, leads to $k_{\parallel,l}$.

Exploiting the system's translational invariance and symmetry along the $\hat{x}$ and $\hat{y}$ direction, it may be chosen the modes with propagation wave vector $\overrightarrow{k} = (k_x, 0, 0)$. Thereby, a general structure of ϕ may be written as in Eq. 3.14, where A_1, A_2 and B are arbitrarily constants, whose dependence on each other is given by the MBC plus the ABC.

$$\phi(r,t) = e^{i(k_\parallel x - \omega t)} \begin{cases} A_1 e^{k_\parallel z} + A_2 e^{k_{\parallel,l} z} & , z < 0 \\ B\, e^{-k_\parallel z} & , z > 0 \end{cases} \tag{3.14}$$

Moreover, these correlations also provide a valuable insight regarding the dispersion curves. So, it is easily checked from 3.14, 3.12 and the two MBC, $\phi(z = 0^+) = \phi(z = 0^-)$ and $\overrightarrow{D}(z = 0^+) = \overrightarrow{D}(z = 0^-)$, that the

linear equations' system may be written in the nicely summarized matricidal form presented in Eq. 3.15.

$$\begin{pmatrix} 1 & 1 & -1 \\ \varepsilon_T(\omega) & 0 & \varepsilon_D \\ \varepsilon_b k_{\parallel} & \varepsilon_b k_{\parallel,l} & \varepsilon_D k_{\parallel} \end{pmatrix} \begin{pmatrix} A_1 \\ A_2 \\ B \end{pmatrix} = \begin{pmatrix} 0 \\ 0 \\ 0 \end{pmatrix} \tag{3.15}$$

This system is solvable by the trivial solution, which is not of special interest here, and by the one that comes from matching the matrix determinant to zero. The latter leads to the Eq. 3.16 and to the relations among the coefficients: $-A_1\varepsilon_T(\omega)/\varepsilon_d = B$ and $A_1 + A_2 = B$.

$$\varepsilon_b(\varepsilon_T(\omega) + \varepsilon_d)k_{\parallel,l} + \varepsilon_d\left(\varepsilon_T(\omega) - \varepsilon_b\right)k_{\parallel} = 0 \tag{3.16}$$

Through simple algebra manipulation, Eq. 3.16 may acquire the arrangement

$$1 + \varepsilon_d\left(\frac{1}{\varepsilon_T(\omega)} + \frac{k_{\parallel}}{k_{\parallel,l}}\left(\frac{1}{\varepsilon_b} - \frac{1}{\varepsilon_T(\omega)}\right)\right) = 0 \tag{3.17}$$

which is identical to the one found in [2], with the exception that in the latter no approximation is made.

In addition, one may realize by rewriting $k_{\parallel,l}$ in terms of $k_{\parallel}$ (that is equivalent to k_x since it is assumed $k_y = 0$) and by replacing $\varepsilon_T(\omega)$ (defined in Eq. 3.8) in the expression 3.17, that it is not possible to achieve a unique analytical function of $k\left(\omega\right)$ for all the domain of ω. Nevertheless, the same does not hold true for the positive domain of ω, which is the one with interesting physical meaning. In fact the dispersion equation $k\left(\omega\right)$ that covers the the entire frequency domain is composed by two branches, being these associated with the negative and positive frequencies. This multivalued feature of the dispersion equation, presented in Eq. 3.18, emerges due to the necessity of $k\left(\omega\right)$ be symmetry for the positive and negative frequencies.

$$k_{\parallel} = \frac{\mid \omega \mid}{\beta}\left(1 - \frac{\omega_{sp}^2}{\omega^2}\right) \tag{3.18}$$

In addition, one may conclude by inspection of Eq. 3.18 that, unlike to what happens in the local model of the SPP in the regime quasi-static, where infinite modes can propagate at $\omega = \omega_{sp}$, in this case no propagation waves are supported.

We used the *Mathematica* and numerical methods to obtain the non-local dispersion curve in the electrostatic regime. This curve is traced in Figure 3.3 together with the dispersion curves for the non-local SPP without approximations (from [2]) and for the one using the local model in the quasi-static regime. The first comment of the derived dispersion curve regarding the one in the electrostatic regime having local medium response is that the curve is no longer a constant line for $\omega = \omega_{sp}$. In fact, it still resembles a horizontal line intrinsic of the local scenario but with a small slope that allows higher frequencies to propagate as the wavenumber increases. Also, in comparison with the dispersion curve associated with the exact model of the non-local response, it is possible to see that for large wavenumbers both slopes are coincident, which allows one to infer that the diffusion effects enable the propagation of frequencies above the usual surface plasmon resonance.

For an easier perception of the nonlocality, it was resorted to normalized variables, such as $\eta_{eff} = k_x/k_0$, $\omega_n = \omega/\omega_p$, and plotted the dispersion curves for different values of β (Figure 3.4). As one may observe, it appears a well known blue shift on the dispersion curve which corroborates the idea that stronger the nonlocality is, the easier is the propagation of modes for frequencies above the ω_{sp}. This also implies that the habitual divergence for the local SPP on the density states at the plasmon resonance no longer appears. Hence, this modification may be seen as a redistribution of those states over a wider range of frequencies interval. Besides that, the quasi-static approximation presents itself a good approximation as the frequency and the wavenumber increase in comparison with the dispersion curve produced by the exact derivation in the dispersion.

It should be stressed out that as β decreases, the non-local influence on the dispersion curves also diminishes, *e.g.*, for $c/\beta = 500$ the curve almost coincides with the line that passes at $\omega = \omega_{sp}$. Throughout this study the

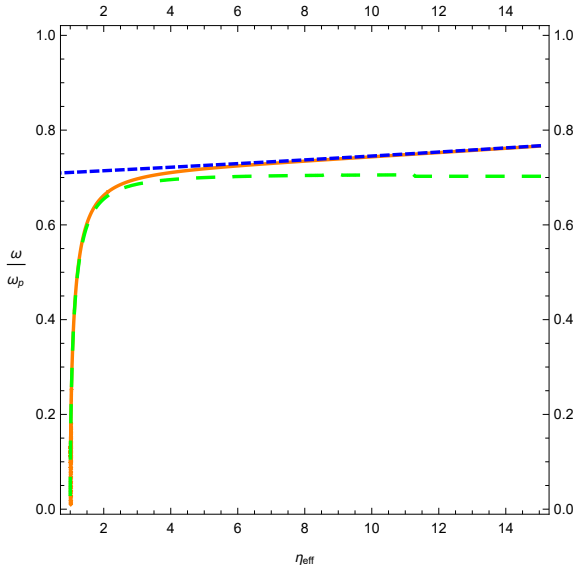

Figure 3.3: Lossless surface plasmon dispersion curves with $\varepsilon_b = 1$, $\varepsilon_d = 1$, $c/\beta = 100$. Although the typical values are around $c/\beta = 200$, where we considered stronger diffusion effects to perceive better the impact of the medium non-locality on the dispersion curves. The green dashed curve corresponds to local scenario within the Drude model, the orange curve corresponds to non-local medium without approximations, the blue dashed curve corresponds to non-local medium in the electrostatic approximation.

phenomenological variable β is assumed to be the one of the silver metal, $\beta \approx 0.0036 \times c$,which is computed by $\beta = \sqrt{\frac{3}{5}} v_F$, where v_F is the *Fermi velocity* of silver.

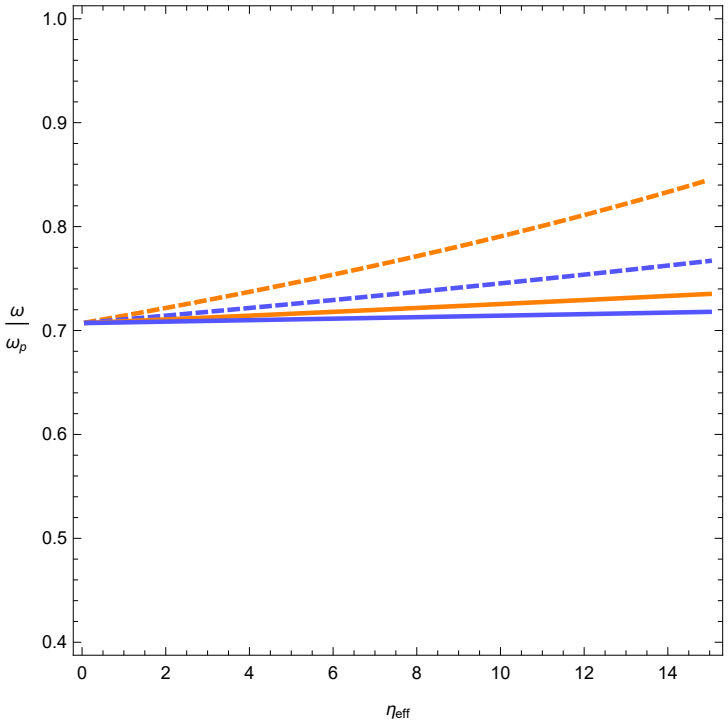

Figure 3.4: Lossless surface plasmon dispersion curves in the quasi-static regime with $\varepsilon_b = 1$, $\varepsilon_d = 1$. The blue dashed curve corresponds to $c/\beta = 50$, the orange dashed curve corresponds to $c/\beta = 100$, the blue curve corresponds to $c/\beta = 200$ and the orange curve corresponds to $c/\beta = 500$.

Thus, it may also be achieved an expression for ω in terms of $k_{\parallel}$ that is represented in Eq. 3.19.

$$\omega\left(k_{\parallel}\right)=\begin{cases}\frac{k_{\parallel}\beta}{2}+\sqrt{\frac{\beta^2k_{\parallel}^2}{4}+\omega_{sp}^2}, & \omega>0\\ \frac{k_{\parallel}\beta}{2}-\sqrt{\frac{\beta^2k_{\parallel}^2}{4}+\omega_{sp}^2}, & \omega<0\end{cases} \tag{3.19}$$

This function is obtained from the quadratic formula, where the signal of the square root must be chosen so that the values of frequency obtained in the original dispersion equation (Eq. 3.17) can be regained. As odd as this double choice in the solution may seem, the new degree of freedom emerges when the term $k_{\parallel,l}$ in Eq. 3.17 is squared, being added a new solution to the equation with no physical meaning. These analytical expressions for relating the wavenumber with the frequency are fundamental for the analysis on the Density of States (DOS) for the non-local SPP, which is addressed bellow.

3.2.2 Density of States of Non-local SPP

As mentioned before, the divergence of the density of states [2] at $\omega=\omega_{sp}$ is an intrinsic characteristic of the SPP described by a local model. This feature has great implications in the interaction between a quantum object and light (SPP electromagnetic waves) which is discussed in the next Section. Therefore, next we derive the DOS of the spatial dispersive SPP, using a two dimensional (2D) analysis, because of the SPP evanescent behavior in the $\hat{z}$ direction, that allows to constrain the propagation along the 2D metal-dielectric interface. The discussion of this topic will be extended to the local media and to the free space scenario. By free space, it is meant that the atom is surrounded by vacuum rather than by the surface plasmonic slab. Unlike to the SPP DOS, which is defined in a 2D space, in the free space scenario we have a three dimensional topology. In addition to the 3D analysis for the free space DOS also a 2D derivation is made in order to compare DOS's with the same dimensions. The 2D free space DOS allows to better compare and understand how the density of states varies with the introducing of a plasmonic interface.

The dispersion relation of the electromagnetic wave in free space is simply given by the *wave equation*, ${k_{\parallel}}^2={k_x}^2+{k_y}^2+{k_z}^2=\varepsilon_0\frac{\omega^2}{c^2}$, where in the 2D case $k_z=0$. For the DOS examination, just the small range of frequencies in the vicinity of the ω_{sp} is important to extract the relevant conclusions.

The usual procedure [54] to derive the DOS of a given electromagnetic source is via the Green Function [55] of the system. However, the equations used to reckon the number of states per frequency and per area or per volume depending on the analysis, are given in Eq. 3.20 and Eq. 3.21 for a 2D and a 3D geometry, respectively.

$$n\left(\omega\right)_{2D}=\frac{1}{L^2}\sum_{ky,kx}\delta\left(\omega-\omega_{k_{\parallel}}\right) \tag{3.20}$$

$$n\left(\omega\right)_{3D}=\frac{1}{L^3}\sum_{ky,kx,kz}\delta\left(\omega-\omega_{k_{\parallel}}\right) \tag{3.21}$$

Whether it is considered a 2D or 3D geometry, L is considered the length of the edges for the square and cube side. The derivation for the 2D and 3D is going to be done in parallel.

Instead of computing the number of states per frequency, many books prefer to use the number of states per energy units, which is the same, in practice since the energy and the frequency are directly related. Another quantity that is extremely useful, but which will not be adopted in this work, is the Local Density of States (LDOS) [56]. In addition to the DOS, the LDOS gives the density of states for a chosen point in the space and it is settled as a weighted sum containing the eigenvectors' amplitude [56].

A common method to sum all the possible states in the k spectral domain is to use the periodic boundary conditions, assuming that $L\to\infty$, to transform the sum into a continuous integral. The resultant equation for

$n(\omega)_{2D}$ and $n(\omega)_{3D}$ are presented in Eq. 3.22 and Eq. 3.23, respectively.

$$n(\omega)_{2D} = \frac{1}{(2\pi)^2} \int_0^\infty dk_x \int_0^\infty dk_y \delta\left(\omega - \omega_{k_\parallel}\right) \tag{3.22}$$

$$n(\omega)_{3D} = \frac{1}{(2\pi)^3} \int_0^\infty dk_x \int_0^\infty dk_y \int_0^\infty dk_z \delta\left(\omega - \omega_{k_\parallel}\right) \tag{3.23}$$

In both cases, the integration variables are in the Cartesian coordinate system, while the wavenumber inside the *Dirac delta* ($k_\parallel$) acts as the radial coordinate either in the polar or spherical system. Thus, a change of variables to the polar and to the spherical systems must take place, in which the integral over the angular variables is equal to 2π in the 2D scenario and 4π in 3D, since the system is rotational invariant in both cases. Hence, the DOS functions acquire the structures of Eq. 3.24 and Eq. 3.25 for the 2D and 3D model, respectively.

$$n(\omega)_{2D} = \frac{1}{2\pi} \int_0^\infty k_\parallel \delta\left(\omega - \omega_{k_\parallel}\right) dk_\parallel \tag{3.24}$$

$$n(\omega)_{3D} = \frac{1}{2\pi^2} \int_0^\infty k_\parallel^2 \delta\left(\omega - \omega_{k_\parallel}\right) dk_\parallel \tag{3.25}$$

Being these general formulas, the derivation of the DOS of the SPP for the non-local model will now take place. The first problem lies on the fact that $\omega_{k_\parallel}$ depends on the integration variable, which complicates the integration. Then, to surpass this difficulty it may be used a property of the *Dirac* δ-function [57], which says that if a function $f(x)$ is monotonic along their integration region, then $\int f(x)\,\delta(g(x))dx = \frac{f(x_0)}{|g'(x_0)|}$, where $g(x_0)$ is the root of $g(x)$. Hence, the expression $n(\omega)$ acquires the new form represented in Eq. 3.26, where $\omega_{k_\parallel}$ is the frequency of the surface plasmons that is related to the wave vector through the dispersion Eq. 3.19.

$$n(\omega) = \frac{1}{(2\pi)} k_\parallel \frac{1}{\left| \frac{\partial \omega}{\partial k} \Big|_{\omega = \omega_{k_\parallel}} \right|} \tag{3.26}$$

Moreover, attending that the derivative $\frac{\partial \omega_{k_\parallel}}{\partial k}$ is determined by Eq. 3.27 and writing the wave vector in terms of ω (accomplished using Eq. 3.18), the DOS of the non-local SPP is simplified into Eq. 3.28.

$$\frac{\partial \omega_{k_\parallel}}{\partial k} = -\frac{\beta}{2} + \frac{k\beta^2}{4\sqrt{\frac{k^2\beta^2}{4} + \omega sp^2}} \tag{3.27}$$

$$n_{sp}(\omega) = \frac{\omega^4 - {\omega_{sp}}^4}{2\pi\beta^2\omega^3} \tag{3.28}$$

This function shows that the density of states at the surface plasmon resonance is zero. This appears to be contradictory according to what happens in the local scenario in the quasi-static approximation, where the number of states diverges at $\omega = \omega_{sp}$. This divergence is easily observed through Eq. 3.24, since that the frequency of any k mode is always $\omega(k) = \omega_{sp}$, implying that the δ-function simplifies into $\delta(\omega - \omega_{sp})$. Consequently, for $\omega \neq \omega_{sp}$ the integral is zero and otherwise is infinite since there are infinite modes of k at the surface plasmon resonance. The explanation to the contrast in the non-local can be made through the inspection of its dispersion curve (blue dashed curve in Figure 3.3), from where is seen that no propagation mode is supported at $\omega = \omega_{sp}$ (since wave vector corresponds to the null vector).

The representation of the DOS for values below ω_{sp} is suppressed throughout this section because the dispersion relation and the propagation modes themselves are not defined for that frequency interval. One may

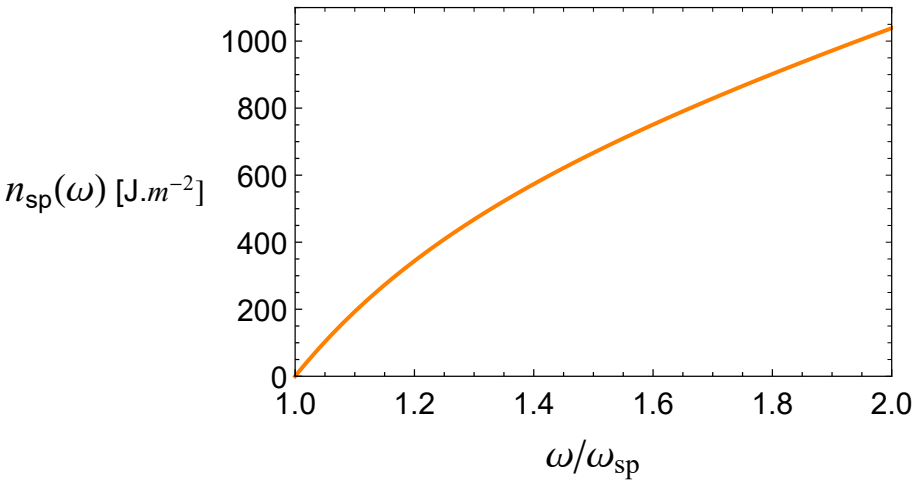

Figure 3.5: Density of states of a non-local surface plasmon, which is plotted for the frequencies in the vicinity of the surface plasmon resonance ($\omega \in [\omega_{sp}, 2\omega_{sp}]$). The frequency is normalized as ω/ω_{sp} and therefore the plot is general for any metal.

inspect from the Figure 3.3 that for $\omega \gg \omega_{sp}$ the exact and approximate curves of the spatial dispersive, SPP overlap. Such behavior occurs due to the validity limit of the quasi-static approximation which portrays accurately the reality of the problem only for the high frequencies (over ω_{sp}) [58].

In addition, the DOS for the local SPP described via the *Drude model* and without the quasi-static approximation being made [2] is presented in the equation below.

$$n_{sp}(\omega)_{Local} = \frac{1}{16\pi c^2} \frac{\omega_{sp}^2}{(\omega_{sp} - \omega)^2} \tag{3.29}$$

However, this formula is only valid for frequencies in the vicinity of ω_{sp} since the original dispersion relation ($k(\omega) = \frac{\omega}{\sqrt{2}c}\sqrt{\frac{\omega_p^2-\omega^2}{\omega_{sp}^2-\omega^2}}$) is approximated by $k(\omega) \approx \frac{\sqrt{\omega_{sp}^3}}{2c}\frac{1}{\sqrt{\omega_{sp}-\omega}}$. From the formula, it is concluded that the same divergence of states occurs at ω_{sp}, albeit that, in contrast to the electrostatic approximation, the number of states at other frequencies is non-zero. However, the DOS decreases as the considered frequency moves away from ω_{sp}.

The DOS of the spatial dispersive SPP is represented in Figure 3.5 for the frequencies interval $[\omega_{sp}, 2\omega_{sp}]$, where is visible that the number of states increases as the frequency increases but without the habitual peak from the local approach. Also, in comparison to the local scenario, where the function of $\omega(k)$ is constant (horizontal line for $\omega = \omega_{sp}$), in the non-local case, the same function is multivalued. Therefore, all the concentration of the k states is redistributed along a wider range of frequencies.

Moving now to the DOS in free space for the 2D and 3D cases, the expressions can be found in Eq. 3.30 and Eq. 3.31, respectively.

$$n_0(\omega)_{2D} = \frac{2\omega}{\pi c^2} \tag{3.30}$$

$$n_0(\omega)_{3D} = \frac{\omega^2}{\pi c^3} \tag{3.31}$$

The main difference in comparison to the DOS derivation for the non-local SPP stands in dispersion relation that is now given by $k = \frac{\omega}{c}$. Additionally, it is also needed to multiply by a factor of 2 because of the two possible polarizations of the modes TEM.

To conclude the analysis is plotted in Figure 3.6 the ratio between $n_{sp}(\omega)$ and $n_0(\omega)_{3D}$. It is identified that $n_0(\omega)_{3D}$ possesses more states than the DOS of the non-local SPP. What one could expect is that the presence

of a metal slab, that is able to support electromagnetic modes, would always increase the number of light modes in comparison to the case of the TLA in empty space. However, the examination $n_{sp}(\omega)$ was made in only two dimensions while the $n_0(\omega)_{3D}$ was made in three. Therefore, it should be instead compared the case ratio between $n_{sp}(\omega)$ and $n_0(\omega)_{2D}$, which is plotted in Figure 3.7. This Figure shows that DOS of the SPP in the nonlocality can achieve magnitudes five times higher than the free space in a 2D geometry, which confirms that the presence of an apparatus that support radiation waves increases the number of states per frequency.

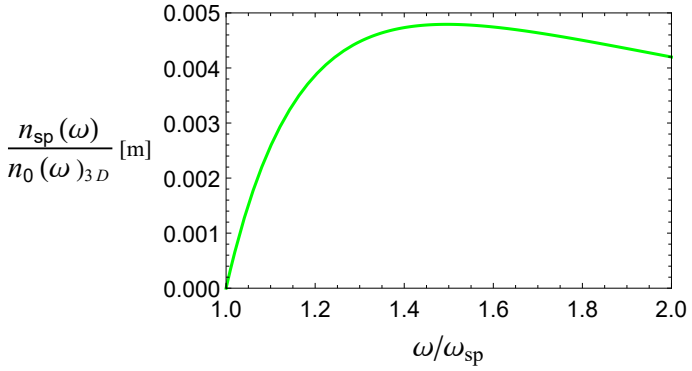

Figure 3.6: The graphic shows the comparison between the DOS of the non-local surface plasmon and of the 3D free space, which is plotted for the frequencies in the vicinity of ω_{sp}. It is considered a silver metal slab, where its $\omega_{sp} \approx 2\pi \times 646$ THz and $\beta \approx 0.0036c$ [m] (being c the speed of light).

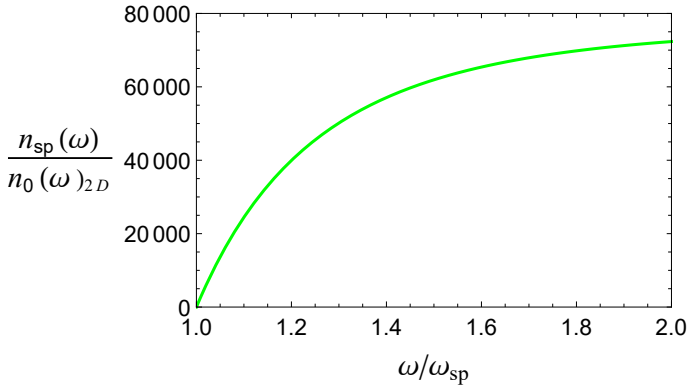

Figure 3.7: The graphic shows the comparison between the DOS of the non-local surface plasmon and of the 2D free Space, which is plotted for the frequencies in the vicinity of ω_{sp}. It is considered a silver metal slab, where its $\omega_{sp} \approx 2\pi \times 646$ THz and $\beta \approx 0.0036c$ [m] (being c the speed of light).

3.3 Non-local SPP Electromagnetic Field Quantization

At this point, the quantization of SPP accounting with the non-local diffusion effects is similar to the one used in the local scenario, and indeed it presents the same structure as the one in Eq. 2.50. Nevertheless, since the electric potential scalar ϕ contains an additional longitudinal wave the values of the normalization constants, given by the habitual normalization in Eq. 2.53, will be different. Another important assumption is the neglect of the system damping, *i.e.*, $\gamma \approx 0$ in order to achieve a real-valued permittivity. The main reason for this approximation is due to the simple approach that can be undertaken. If the losses were introduced directly in the permittivity, then the Hamiltonian, that is composed by the electric field operator, would not be *Hermitian*, which is a required property of any observable. Then, to account with the losses, it would be necessary to introduce phenomenological variable that would reproduce the effects of the losses (for a thorough understanding see [28]).

However, the material matrix M is now dependent not only on the frequency but also on the wave vector $\overrightarrow{k}$, as shown in Eq. 3.32.

$$\mathrm{M} = \begin{pmatrix} \hat{\varepsilon}(\omega, \overrightarrow{k})\mathrm{I}_{3\times3} & 0 \\ 0 & \mu_0\mathrm{I}_{3\times3} \end{pmatrix} \tag{3.32}$$

Consequently, this means that $\frac{\partial[\omega\mathrm{M}]}{\omega}$ is defined for each k mode. Indeed, only the term regarding the permittivity is of interest since $F_{nk} = (E_{nk}, 0)^T$ and therefore only $\frac{\partial[\omega\hat{\varepsilon}]}{\omega}$ is relevant to compute. Moreover, since it is considered the electrostatic approximation the electric field can be defined in terms of an electric scalar potential such that $\overrightarrow{E} = -\nabla\phi(\omega, \mathrm{r})$, where $\phi(\omega, \mathrm{r})$ is the potential defined previously in Eq. 3.14. Therefore the electric field may be rewritten as

$$\vec{E} = -ie^{ik_\parallel x} \begin{cases} \overrightarrow{k_1}E_1 + \overrightarrow{k_2}E_2 & , z < 0 \\ \overrightarrow{k_3}E_3 & , z > 0 \end{cases} \tag{3.33}$$

where: $\overrightarrow{k_1} = \left(k_\parallel, 0, -ik_\parallel\right)$; $\overrightarrow{k_2} = \left(k_\parallel, 0, -ik_{\parallel l}\right)$; $\overrightarrow{k_3} = \left(k_\parallel, 0, ik_\parallel\right)$; $E_1 = A_1e^{k_\parallel z}$; $E_2 = A_2e^{k_{\parallel l} z}$; $E_3 = Be^{-k_\parallel z}$. The advantage in such representation lies in the fact that, for the metal interface, $\frac{\partial[\omega\hat{\varepsilon}(\omega, \overrightarrow{k})]}{\omega}$ can also be written in terms of wave vectors, as one may foresee from 3.10, simplifying greatly the normalization computation. Actually, it is easy to confirm that in the metal interface $\frac{\partial[\omega\hat{\varepsilon}(\omega, \overrightarrow{k})]}{\omega} \cdot \left(\overrightarrow{k_1}E_1 + \overrightarrow{k_2}E_2\right)$ yields to $\varepsilon_0\left[E_1\left(\varepsilon_b + \frac{\omega_p^2}{\omega^2}\right)\overrightarrow{k_1} + E_2\left(2\varepsilon_b^2\frac{\omega_p^2}{\omega^2}\right)\overrightarrow{k_2}\right]$. Nevertheless, one must recall that the ω and $\overrightarrow{k}$ variables must be replaced by corresponding propagating mode for which they are multiplying ($\vec{k_1}$ or $\vec{k_2}$) in the expression $\frac{\partial[\omega\hat{\varepsilon}(\omega, \overrightarrow{k})]}{\omega}$. Another property that eases the calculation is the fact that multiplying a wave vector $\vec{k_i}$ by $\left(I - \frac{\overrightarrow{k}\otimes\overrightarrow{k}}{\overrightarrow{k}^2}\right)$ yields to zero, by the implicit definition of the transverse permittivity term.

Clearly, in the dielectric interface, it results that $\frac{\partial[\omega\hat{\varepsilon}]}{\omega} = \varepsilon_0\varepsilon_d$ since the dielectric response is a constant. At this point, it only remains the assignment of the integral limits in the normalization expression. Hence, it is assumed that the metal slab has a general length L along the $\hat{x}$ and $\hat{y}$ direction and that it has no limitation in the $\hat{z}$ direction, *i.e.*, $\int_0^L dx \int_0^L dy \int_{-\infty}^{\infty} dz$. Since the wave decaying grows very rapidly as one moves further away from the slab, the limits in the $\hat{z}$ direction can be considered as a good approximation. Finally, the normalization after some algebraic manipulation results in

$$\frac{1}{2}\varepsilon_0 \int_0^L dx \int_0^L dy \left\{ \begin{array}{l} \int_{-\infty}^{0} \left[\begin{array}{l} \left(\left|\overrightarrow{k_1}E_1\right|^2 + \overrightarrow{k_2}^* \cdot \overrightarrow{k_1}{E_2}^*E_1\right)\left(\varepsilon_b + \frac{{\omega_p}^2}{{\omega_{nk}}^2}\right) \\ + \left(\left|\overrightarrow{k_2}E_2\right|^2 + \overrightarrow{k_1}^* \cdot \overrightarrow{k_2}{E_1}^*E_2\right)\left(2\frac{\varepsilon_b^2{\omega_p}^2}{{\omega_{nk}}^2}\right) \end{array} \right] dz \\ + \int_0^{\infty} \varepsilon_d\left|\overrightarrow{k_3}E_3\right|^2 dz \end{array} \right\} = 1 \tag{3.34}$$

One can further simplify the above expression, noting that inside the integral no term depends on the coordinates x and y, *i.e.*, $\int_0^L d_x \int_0^L d_y = L^2$. In addition, if the wave vectors $\vec{k_i}$ and the E_i are replaced by their expression presented above, it is easily extracted the integrals over z, leading to the Eq. 3.35.

$$\frac{1}{2}L^2\varepsilon_0 \left[\frac{|A_2|^2\left(k_\parallel^2 + k_{\parallel.l}^2\right)\omega^2{\varepsilon_b}^2}{k_{\parallel,l}\omega_p^2} + \frac{|A_1|^2k_\parallel\left(\omega_p^2 + \varepsilon_b\omega^2\right)}{\omega^2} + A_2^*A_1k_\parallel\left(\varepsilon_b + \frac{\omega_p^2}{\omega^2} + \frac{2\varepsilon_b^2\omega^2}{\omega_p^2}\right) + |B|^2k_\parallel\right] = 1 \tag{3.35}$$

In fact, in the latter equation was used one of the boundary conditions relating A_1 with A_2 to realize that $A_1^*A_2 = A_1A_2^*$, which allowed to group both terms. Furthermore, it is admitted that the dielectric substrate is vacuum ($\varepsilon_d = 1$) and that the bound charge contribution for the metal permittivity is $\varepsilon_b = 1$ for a matter of simplicity.

In these conditions, the linear system of equations that determine the normalization constants is fully determined and the expressions for these coefficients may be found in Eq. 3.36. This solution results from the combination of the normalization equation Eq. 2.53 with the two of the three equations derived from the boundary conditions (*e.g.*, $-A_1\varepsilon_T(\omega)/\varepsilon_d = B$ and $A_1 + A_2 = B$), which form a linear independent equation's system. In fact, apart from one degree of freedom regarding the arbitrary initial phase, the normalization constants are well determined and the initial phase is chosen in such a way that it leads to Eqs. 3.36a, 3.36b and 3.36c.

$$A_1 = \frac{\sqrt{\frac{2}{L^2\varepsilon_0}}}{\sqrt{k_\parallel \varepsilon_T(\omega)^2 + k_\parallel \frac{\omega^2+\omega_p^2}{\omega^2} + (1+\varepsilon_T(\omega))^2 \frac{\omega^2}{\omega_p^2}\frac{k_\parallel^2+k_{\parallel,l}^2}{k_{\parallel,l}} - k_\parallel (1+\varepsilon_T(\omega))\left(1+\frac{2\omega^2}{\omega_p^2}+\frac{\omega_p^2}{\omega^2}\right)}} \tag{3.36a}$$

$$A_2 = -\frac{(1+\varepsilon_T(\omega))\sqrt{\frac{2}{L^2\varepsilon_0}}}{\sqrt{k_\parallel \varepsilon_T(\omega)^2 + k_\parallel \frac{\omega^2+\omega_p^2}{\omega^2} + (1+\varepsilon_T(\omega))^2 \frac{\omega^2}{\omega_p^2}\frac{k_\parallel^2+k_{\parallel,l}^2}{k_{\parallel,l}} - k_\parallel (1+\varepsilon_T(\omega))\left(1+\frac{2\omega^2}{\omega_p^2}+\frac{\omega_p^2}{\omega^2}\right)}} \tag{3.36b}$$

$$B = -\frac{\varepsilon_T(\omega)\sqrt{\frac{2}{L^2\varepsilon_0}}}{\sqrt{k_\parallel \varepsilon_T(\omega)^2 + k_\parallel \frac{\omega^2+\omega_p^2}{\omega^2} + (1+\varepsilon_T(\omega))^2 \frac{\omega^2}{\omega_p^2}\frac{k_\parallel^2+k_{\parallel,l}^2}{k_{\parallel,l}} - k_\parallel (1+\varepsilon_T(\omega))\left(1+\frac{2\omega^2}{\omega_p^2}+\frac{\omega_p^2}{\omega^2}\right)}} \tag{3.36c}$$

To gain some insights regarding these abstract formulas, the analogy with the ones for a local approach of the surface plasmons can be made, where the normalization constants are given by $|A_1| = |B| = \frac{1}{\sqrt{2L^2\varepsilon_0 k_\parallel}}$ and $A_2 = 0$ (since the longitudinal wave is not predicted by the *Drude's* model) [38]. Indeed, if the obtained constants are evaluated at the surface plasmon frequency the results match exactly the local approach. In order to compare the values of these coefficients over the frequencies near the surface plasmon resonance, it is plotted the values of A_1, A_2 and B, in the Figure 3.8. Their absolute value will also be needed for the spontaneous emission computation for the non-local SPP, reason why it is represented in Figure 3.9, from where, in particular, it is discerned that for frequencies near ω_{sp}, $|B|$ presents a small variation.

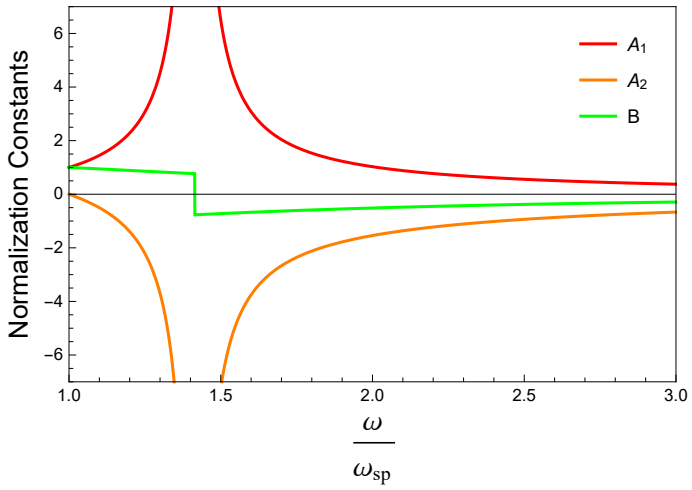

Figure 3.8: Plot of the normalization constants over the normalized frequency ω/ω_p for the frequencies in the interval $\omega \in [0, 1.5\,\omega_p]$. The red, orange and green curves are associated with the constants A_1, A_2 an B, respectively. Their value is also normalized to $\frac{1}{\sqrt{2L^2\varepsilon_0 k_\parallel}}$ (value of the constants for the local SPP in the quasi-static approximation at $\omega = \omega_{sp}$). Is was assumed a silver slab with $\beta \approx 0.0036 \times c$, with c the speed of light.

Furthermore, the nonlocality has influence in the value of these coefficients over the frequency, through the wave vectors $k_{\parallel,l}$ and $k_\parallel$ as one may check from the dispersion equation. However, if these values are normalized

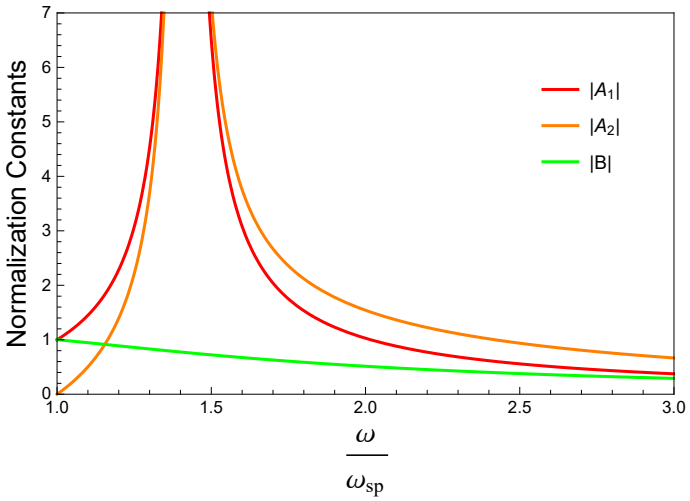

Figure 3.9: Plot of the absolute value of the normalization constants over the normalized frequency ω/ω_p for the frequencies in the interval $\omega \in [0.5\,\omega_p, 1.5\,\omega_p]$. The red, orange and green curves are associated with the constants $|A_1|$, $|A_2|$ an $|B|$, respectively. Their value is also normalized to $\frac{1}{\sqrt{2L^2\varepsilon_0 k_\parallel}}$ (value of the constants for the local SPP in the quasi-static approximation at $\omega = \omega_{sp}$). Is was assumed a silver slab with $\beta \approx 0.0036 \times c$, with c the speed of light.

by the value for the local scenario in the quasi-static approximation, $\frac{1}{\sqrt{2L^2\varepsilon_0 k_\parallel}}$, then an interesting feature arises when computing the plot of the coefficients for different values of β. In the case where the normalization is made, one may further check that the plots do not modify their shape by varying the diffusion strength. However, on the other hand, if no normalization is applied, then the graphics, that are presented in Figures 3.10, 3.11 and 3.12, vary with the variation of β, wherein the local limit is observed that every coefficient tends to zero for any given frequency. Hence, this implies that the dependence of these normalization constants with β is essentially proportional to $\frac{1}{\sqrt{k_\parallel}} \propto \sqrt{\beta}$, that indeed tends to zero as β goes to zero.

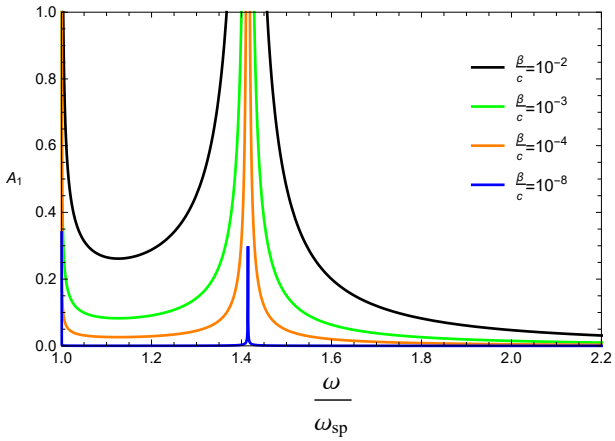

Figure 3.10: Plot of the normalization constant A_1 over the frequency interval $\omega \in [0.5\,\omega_p, 1.5\,\omega_p]$ for different values of β. The black, green, orange and blue curve correspond to diffusion strengths of $\frac{\beta}{c} = 10^{-2}, \frac{\beta}{c} = 10^{-3}, \frac{\beta}{c} = 10^{-4}, \frac{\beta}{c} = 10^{-8}$, respectively. The coefficient was normalized to $\frac{1}{\sqrt{L^2\varepsilon_0}}$.

Apart from one degree of freedom, regarding the arbitrary initial phase, the normalization constants are well determined and the initial phase is chosen in such a way that it leads to Eqs. 3.36a, 3.36b and 3.36c.

Returning to the quantization of the SPP Electromagnetic field, one may notice that since all the constants are well determined, the electric field operator may be written down immediately. This is accomplished by resorting to the habitual expression of the electromagnetic field operator, which for the sake of convenience is

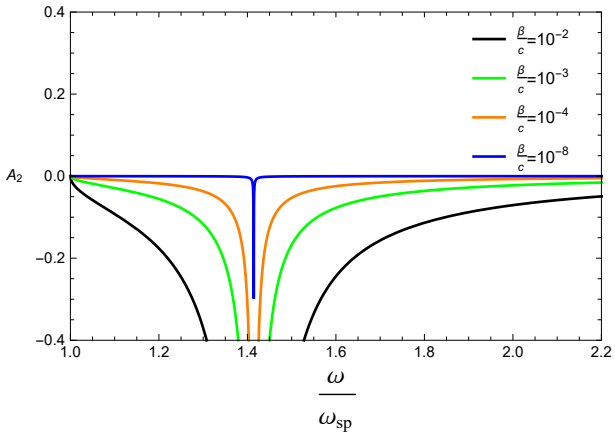

Figure 3.11: Plot of the normalization constant A_2 over the frequency interval $\omega \in [0.5\,\omega_p, 1.5\,\omega_p]$ for different values of β. The black, green, orange and blue curve correspond to diffusion strengths of $\frac{\beta}{c} = 10^{-2}, \frac{\beta}{c} = 10^{-3}, \frac{\beta}{c} = 10^{-4}, \frac{\beta}{c} = 10^{-8}$, respectively. The coefficient was normalized to $\frac{1}{\sqrt{L^2\varepsilon_0}}$.

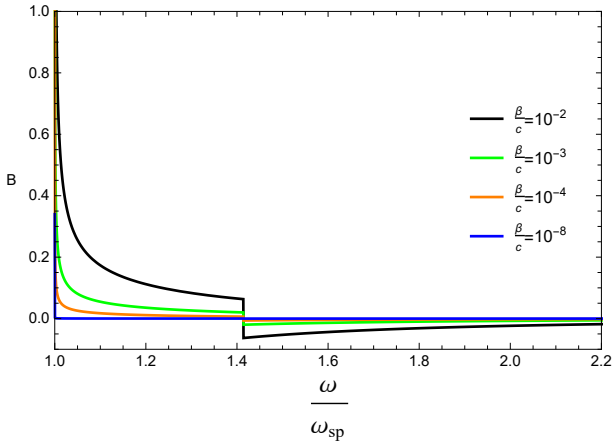

Figure 3.12: Plot of the normalization constant B over the frequency interval $\omega \in [0.5\,\omega_p, 1.5\,\omega_p]$ for different values of β. The black, green, orange and blue curve correspond to diffusion strengths of $\frac{\beta}{c} = 10^{-2}, \frac{\beta}{c} = 10^{-3}, \frac{\beta}{c} = 10^{-4}, \frac{\beta}{c} = 10^{-8}$, respectively. The coefficient was normalized to $\frac{1}{\sqrt{L^2\varepsilon_0}}$.

rewritten above in Eq. 3.37, where $\mathbf{E}_{nk}(r)$ corresponds to the nk mode of the electric field, whose expression is found at 3.20.

$$\widehat{\mathbf{E}}(r) = \sum_{\omega_{nk}>0} \sqrt{\frac{\hbar\omega_{nk}}{2}} \left(\widehat{\mathbf{a}}_{nk}\mathbf{E}_{nk}(r) + \widehat{\mathbf{a}}^{\dagger}_{nk}\mathbf{E}^{*}_{nk}(r)\right) \tag{3.37}$$

Chapter 4

Quantum Model Description For Light-Matter Systems

4.1 Two-level Atom Approximation

The present Section attempts to conduct a simplified quantum analysis of an atom, whose purpose is to perform an examination on the interactions between the atom and the Electromagnetic field modes of the non-local surface plasmons. As it is well known, an atom is constituted by a positively charged nucleus and by electron(s) that is(are) associated with a corresponding orbital. Plenty of work [22, 59, 32] dedicated to the study of atoms has been developed over the years. Yet, even for the simplest problem (hydrogen atom), a complex treatment is still required to derive the eigenstates and the energy levels. In these approaches, concepts such as the *quantum numbers* (n, l, m_l, m_s) and the energy degeneracies produced by symmetries of the atom arise naturally and are discussed in detail at [59, 32]. Leaving aside all these interesting but rather complex properties of an atom, the study to be developed will seek to simplify as much as possible its mathematical representation by applying the Two-Level Atom (TLA) approach, which will be developed below.

The two-level approximation model [60] is the elected approach to take in quantum optics when dealing with atom-light interactions, since it reproduces the important features [61] of the system such as the *Spontaneous Emission* and the *Rabi oscillations*. This approximation considers that the real structure of an atom, containing an infinite number of energy levels, can be well described at some extent by one having only two energy levels [60]. This approximation is supported by two other considerations [62]. The first assumes that the interaction between the atom and the radiation fields are weak enough to introduce the Dipole Approximation (DA) (consult [22] for derivation of DA) that will be addressed further. The second assumes that the frequency of the interacting Electromagnetic field, ω_{EM}, is near to the resonance transition frequency ω_0 of the two energy levels considered and detuned from the resonant frequency of any other possible transition [63]. Here, the resonant frequency transition is related to the absolute energy difference, $E_{gap} = \|E_n - E_m\|$, between two given energy levels n and m by $\omega_{nm} = E_{gap}/\hbar$. In fact, it is quite well known from the past literature [60] that the transitions, which occur due to the radiation interaction, have their main contribution from the field's frequencies that are near the resonant frequencies transitions, neglecting the rapidly oscillatory terms. This latter assumption is formally designed by Rotating Wave Approximation (RWA) and it will be later discussed.

The mathematical representation [64] of the two-level atom is formally analogous to the one of a $\frac{1}{2}$ spin particle in an external magnetic field, since the spin can either be parallel or anti-parallel to the field, leading to two different eigenenergy levels. The details of the spatial dependence in the wave-functions regarding the

eigenstates of the TLA shall be ignored and are retained within the bra $\langle i|$ and ket $|i\rangle$ notation.

A two-level energy atom is described (at Figure 4.1) by a two-dimensional state space spanned by the two energy eigenstates $|e\rangle$ and $|g\rangle$ corresponding to the excited and the ground states, respectively. The two states constitute a complete orthonormal basis such that $|e\rangle = (1\,,0)^T$ and $|g\rangle = (0\,,1)^T$. The Hamiltonian operator of the two-level atom is simply given by

$$H_{At} = E_e\,|e\rangle\,\langle e| + E_g\,|g\rangle\,\langle g| \tag{4.1}$$

where E_e and E_g are the only two energy eigenvalues for the excited and ground states, correspondingly. Moreover, the energy eigenvalues are such that $E_e = (\hbar\omega_0)/2$ and $E_g = -(\hbar\omega_0)/2$, see Figure 4.1. One should bear in mind that, since no absolute energy can be measured, the eigenenergies values are arbitrary and may be chosen according to each preference, whereas the energy difference must stay invariant to such alternative.

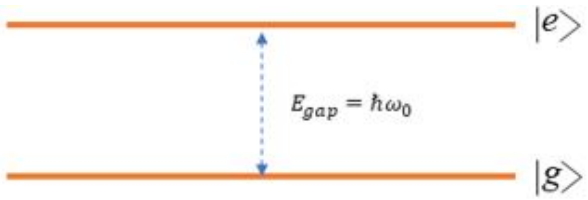

Figure 4.1: Two level atom representation with the below state corresponding to the ground state and the upper one to the excited state.

The usual operators introduced regarding the subject of the two-level atom are the $\boldsymbol{\sigma}^+$ and $\boldsymbol{\sigma}^-$, which are defined as

$$\sigma^+ = |e\rangle\,\langle g| = \begin{pmatrix} 0 & 1 \\ 0 & 0 \end{pmatrix} \tag{4.2a}$$

$$\sigma^- = |g\rangle\,\langle e| = \begin{pmatrix} 0 & 0 \\ 1 & 0 \end{pmatrix} \tag{4.2b}$$

Their physical consequences are perceptible as one applies these operators to a general state $\psi = c_e\,|e\rangle + c_g\,|g\rangle$, whence the $\boldsymbol{\sigma}^+$ yields to the excitation of an electron on the ground state to the excited one, and $\boldsymbol{\sigma}^-$ produces the opposite transition.

In addition, the Pauli matrices [65], presented at Eq. 4.3, are typically introduced because they provide a convenient basis.

$$\boldsymbol{\sigma_x} = \begin{pmatrix} 0 & 1 \\ 1 & 0 \end{pmatrix} \qquad \boldsymbol{\sigma_y} = \begin{pmatrix} 0 & -i \\ i & 0 \end{pmatrix} \qquad \boldsymbol{\sigma_z} = \begin{pmatrix} 1 & 0 \\ 0 & -1 \end{pmatrix} \tag{4.3}$$

The subscript in these matrices is associated with the respective spatial coordinate. The Hamiltonian in this notation may be compactly written as $H_{At} = \frac{\hbar\omega_0}{2}\boldsymbol{\sigma_z}$. In contrast to $\boldsymbol{\sigma}^+$ and $\boldsymbol{\sigma}^-$, $\boldsymbol{\sigma_z}$ is a Hermitian operator and its expectation value is an observable physical quantity. Also, its expectation value, $\langle\psi\,|\sigma_z|\,\psi\rangle = |c_e|^2 - |c_g|^2$, gives the inversion w of the atom, since $|c_e|^2$ and $|c_g|^2$ are the probabilities for finding, respectively, the atom in state $|e\rangle$ or $|g\rangle$ upon a measurement. One may find out that $|c_e|^2 + |c_g|^2$ must be equal to 1, since the TLA can only be found either in the ground or in the excited states.

4.2 Light-Matter Interactions

4.2.1 Dipole Approximation

With the quantum description of the two-level atom and the surface plasmons addressed, it is now time to discuss how a quantum object (fermion) interacts with the electromagnetic fields' modes, and further ahead with the non-local SPP in specific. Although a rigorous examination would require the inclusion of the vacuum modes in the system interaction, this will not be part of the following approach because the coupling between the atom and the SPP modes is considered to be stronger.

In the literature [66, 67], the light-matter interactions have been subject of an extensive analysis. For the simple case of an electron trapped in a binding atomic potential $\mathbf{V}(r)$ and subjected to the action of an external electromagnetic field, an Hamiltonian of the system $\mathbf{H}_{Tot}$ can be formulated as appears in Eq. 4.4.

$$\mathbf{H}_{Tot} = \frac{1}{2m}[\mathbf{P} - e_0\mathbf{A}(r,t)]^2 + e\mathbf{U}(r,t) + \mathbf{V}(r) \tag{4.4}$$

The $\mathbf{A}(r,t)$ and $\mathbf{U}(r,t)$ are the vector and scalar potential of the electromagnetic field, respectively, and e_0 is the elementary charge. It has been shown [22, 68] that if the light interaction is a weak perturbation, $\mathbf{H}_{Tot}$ can be expressed by the sum of three Hamiltonian parcels displayed at Eq. 4.5, where $\mathbf{H}_{At} = \frac{1}{2m}\mathbf{P}^2 + \mathbf{V}(r)$ is the unperturbed atom Hamiltonian contribution, $\mathbf{H}_{EM}$ the electromagnetic Hamiltonian and $\mathbf{H}_{Int} = -\vec{\boldsymbol{\mu}} \cdot \vec{\boldsymbol{E}}(r_0,t)$ the Hamiltonian due to the interaction between the last two unperturbed systems. Here r_0 corresponds to the position of the atom's center of mass in an arbitrary coordinate system, which is chosen to be the one of Figure 3.2.

$$\mathbf{H}_{Tot} = \mathbf{H}_{At} + \mathbf{H}_{EM} + \mathbf{H}_{Int} \tag{4.5}$$

In the latter expression, $\vec{\boldsymbol{E}}(r_0,t)$ stands for the electric field operator and $\vec{\boldsymbol{\mu}}$ corresponds to the electric dipole moment operator given by $\vec{\boldsymbol{\mu}} = -e_0\vec{\boldsymbol{r}}$, assuming, therefore, a similar format to that of a classical electrostatic potential. As a matter of fact, the interaction Hamiltonian only assumes that form if the frequency of the electric field is close to the resonant frequency ω_0 of the transition in the two-level atom. One should not confuse the position r_0 with the operator $\vec{\boldsymbol{r}}$. The latter is identical to a vector with the atom center of mass (positive charge) as the initial point and the negative charge (electrons) as the terminal point. Due to the quantum mechanical uncertainty in the electron and atom positions, $\vec{\boldsymbol{r}}$ must be an operator rather than a vector.

Since the electron is not at the same position as the nucleus but at its surroundings, the interaction Hamiltonian should have a dependence on r (the electron position in the chosen coordinate system). However, if the wavelengths associated with the light modes are bigger than the atomic boundary distance, the *Dipole Approximation* (DA) [60, 66, 68] can be adopted. The DA basically states that the electron "sees" a constant electromagnetic field along their orbitals and therefore its position $r \approx r_0$, *i.e.*, which in fact yields to $\mathbf{H}_{Int} \approx -\vec{\boldsymbol{\mu}} \cdot \vec{\boldsymbol{E}}(r_0,t)$. Since the size of the atoms are the $10^{-10}[m]$ order, the maximum frequency in the validity region of DA lies in the ultraviolet spectrum. Thus, it is suitable for most plasmonic structures since ω_{sp} is found below this range.

Notice that none atom or atomic levels were specified for the present work. In fact, this conceptual problem only demands that the atoms (or either quantum dots[1]) must have a reasonable structure that allows the TLA approximation and a resonant frequency transition near the frequency of interest ω_{sp}. The reason behind this is that the important task here is to observe the consequences of the interaction on the spontaneous emission rate of the SPP and its differences for a range of frequencies near the surface plasmon resonance, since the density of states in the Local Density of States is higher near ω_{sp}.

[1]Quantum dots[69] are semiconductor nanocrystals and are sometimes designed as *artificial atoms* to emphasize that have bound, discrete electronic states confined in all three spatial dimensions. The quantum dot has a discrete quantized energy spectrum and their tunable band gap varies with the particle size, which proportionates a unique opportunity to consider it as an artificial two-level atom with a resonant frequency near the ω_{sp} [70, 71].

Moreover, it is useful to write the dipole moment operator in terms of the excited and ground state basis, being represented in a matricidal structure in 4.6.

$$\vec{\boldsymbol{\mu}} = -e_0 \begin{pmatrix} \langle e\,|\tilde{\mathbf{r}}|\,e\rangle & \langle e\,|\tilde{\mathbf{r}}|\,g\rangle \\ \langle g\,|\tilde{\mathbf{r}}|\,e\rangle & \langle g\,|\tilde{\mathbf{r}}|\,g\rangle \end{pmatrix} \tag{4.6}$$

The electrons possess a symmetrical distribution with respect to the nucleus [72]. Therefore, it is perfectly reasonable to predict that the $\langle e\,|\tilde{\mathbf{r}}|\,e\rangle$ and $\langle g\,|\tilde{\mathbf{r}}|\,g\rangle$ will vanish since the electric displacement operator $\vec{\boldsymbol{r}}$ is a vector and so, for two symmetric positions, it will have opposite signals. This may be better explained either in the grounds of the parity or by the Wigner-Eckart theorem [22]. Consequently, the electric dipole moment yields to Eq. 4.7, where $\vec{\gamma} = e_0\,\langle g\,|\tilde{\mathbf{r}}|\,e\rangle$ and $\vec{\gamma}^* = e_0\,\langle e\,|\tilde{\mathbf{r}}|\,g\rangle$, due to the Hermitian property of the electric dipole moment operator.

$$\vec{\boldsymbol{\mu}} = -\left[\vec{\gamma}\boldsymbol{\sigma}^- + \vec{\gamma}^*\boldsymbol{\sigma}^+\right] \tag{4.7}$$

Besides, as one may check by the expectation value of $\vec{\boldsymbol{\mu}}$ in Eq. 4.8, this only remains not-null if the system is in a superposition of the excited and the ground state.

$$\langle\psi\,|\vec{\boldsymbol{\mu}}|\,\psi\rangle = -e\left[c_g^* c_e\,\langle g|\,\vec{\boldsymbol{r}}\,|e\rangle + c_e^* c_g\,\langle e|\,\vec{\boldsymbol{r}}\,|g\rangle\right] \tag{4.8}$$

4.2.2 Rabi Oscillations

Before proceeding with the analysis of the SPP, it is worth to address the classical analogous system of a two-level atom and a classical monochromatic electrical field of the form $\vec{E} = E_0\vec{\xi}\left[e^{i(kr_0-\omega t)} + e^{-i(kr_0-\omega t)}\right]$. This is a typical introductory example found in quantum optics books such as [68, 73], in which is observed the *Rabi Oscillations* phenomenon. An extensive literature has been devoted to this phenomenon, which is endorsed experimentally either by its detection in observations in single electron spin [74] or in a single molecule [75]. As it is evident the $\mathbf{H}_{EM}$ is here dropped and for the case where $\vec{\boldsymbol{\mu}}$ and $\vec{\xi}$ are parallel, the interaction Hamiltonian is reduced to

$$\mathbf{H}_{Int} = \left[\gamma\sigma^- + \gamma^*\sigma^+\right] E_0\left[e^{i(kr_0-\omega t)} + e^{-i(kr_0-\omega t)}\right] \tag{4.9}$$

Moreover, to understand the time evolution of this system is particularly convenient to define a wave function $|\psi(t)\rangle$ as in Eq 4.10.

$$|\psi(t)\rangle = c_e(t)e^{-i\frac{\omega_0}{2}t}\,|e\rangle + c_g(t)e^{i\frac{\omega_0}{2}t}\,|g\rangle \tag{4.10}$$

This choice becomes clear once the $|\psi(t)\rangle$ is plugged in the *Schrödinger* equation, since, due to the two-level atom, the time evolution is completely incorporated by the exponential terms, whereas the derivative terms in Eq. 4.11 are associated with the electric dipole moment.

$$i\hbar\left(\dot{c}_e(t)e^{-i\frac{\omega_0}{2}t}\,|e\rangle + \dot{c}_g(t)e^{i\frac{\omega_0}{2}t}\,|g\rangle\right) = \mathbf{H}_{Int}\left(c_e(t)e^{-i\frac{\omega_0}{2}t}\,|e\rangle + c_g(t)e^{i\frac{\omega_0}{2}t}\,|g\rangle\right) \tag{4.11}$$

Furthermore, it is straightforward to check that, by multiplying on both sides of Eq. 4.11 by $\langle e|$ and $\langle g|$ and attending to Eq. 4.9, the following two distinct differential equations can be obtained

$$\dot{c}_e(t) = -\frac{i}{\hbar}\gamma^* E_0\left[e^{i(kr_0-\omega t)} + e^{-i(kr_0-\omega t)}\right] c_g(t)e^{i\omega_0 t} \tag{4.12a}$$

$$\dot{c}_g(t) = -\frac{i}{\hbar}\gamma\, E_0\left[e^{i(kr_0-\omega t)} + e^{-i(kr_0-\omega t)}\right] c_e(t)e^{-i\omega_0 t} \tag{4.12b}$$

Afterward, as it is common, it is employed the *RWA*, which fundamentally says that for large enough time intervals, the terms rotating with higher frequencies, $\omega_0 + \omega$, seem static, *i.e.*, their mean value is approximately zero, and, thus, only the slow rotating terms $\triangle = \omega - \omega_0$ are considered. For a deeper understanding of the *RWA* and their subtle use case variations please consult [64, 76]. Also, the slow rotating terms are said to be energy conserving terms [68].

In this approximation it is rather easy to find a general solution for the motion equations 4.12, since both the expressions can be separated into to second order differential equations, whose general solution is given in Eqs. 4.13.

$$c_e(t) = e^{-i\frac{\Delta}{2}t}\left[A_1\cos\left(\tilde{\Omega}_R t\right) + A_2\sin\left(\tilde{\Omega}_R t\right)\right] \tag{4.13a}$$

$$c_g(t) = e^{i\frac{\Delta}{2}t}\left[B_1\cos\left(\tilde{\Omega}_R t\right) + B_2\sin\left(\tilde{\Omega}_R t\right)\right] \tag{4.13b}$$

In the latter, the A_1, A_2, B_1 and B_2 are arbitrary constants, $\tilde{\Omega}_R = \frac{\sqrt{\Delta^2 + 4{\Omega_R}^2}}{2}$ is a general *Rabi oscillation frequency* and $\Omega_R = \frac{|\gamma|E_0}{\hbar}$ is the actual *Rabi oscillation frequency* that appears at the resonance. In order to seek a particular expression for the problem, it must be imposed that the probability of electron to be found in any energy level at any time is always equal to one (*i.e.* $|c_e(t)|^2 + |c_g(t)|^2 = 1$).

Likewise, an initial condition is required, in which for the present case it will be deliberately assumed that the electron at the time $t = 0$ is in the excited state and consequently, $|c_e(t=0)|^2 = 1$ and $|c_g(t=0)|^2 = 0$. Lastly, an arbitrary phase is adopted such that the finals expressions in Eq. 4.14 are produced.

$$c_e(t) = e^{-i\frac{\Delta}{2}t}\left[\cos\left(\tilde{\Omega}_R t\right) + i\frac{\Delta}{2\tilde{\Omega}_R}\sin\left(\tilde{\Omega}_R t\right)\right] \tag{4.14a}$$

$$c_g(t) = -ie^{i\frac{\Delta}{2}t}e^{-ikr_0}Arg(\gamma)\frac{\Omega_R}{\tilde{\Omega}_R}\sin\left(\tilde{\Omega}_R t\right) \tag{4.14b}$$

Moreover, in the resonance regime ($\omega_0 = \omega$) one has $\Delta = 0$ and $\tilde{\Omega}_R = \Omega_R$ which consequently simplify the transition temporal equations into the following formulas

$$c_e(t) = \cos\left(\tilde{\Omega}_R t\right) \tag{4.15a}$$

$$c_g(t) = -ie^{-i\vec{k}\cdot\vec{r}}Arg(\gamma)\sin\left(\tilde{\Omega}_R t\right) \tag{4.15b}$$

These oscillations reveal the intrinsic periodicity of the transitions produced by an external field mode with a frequency near the resonance. Although it will not be the same, this property already presents itself an insightful behavior regarding the interaction of the SPP with the two-level atom.

4.3 Spontaneous Emission of Non-local SPP in the Presence of a TLA

Moving now into one of the goals of this dissertation, a formulation of the time evolution for the interaction of the non-local SPP with the two-level atom will be carried right away.

However, for the situation where the Electromagnetic field is described by an operator, the time evolution of the eigenstates of the system is not so trivial to formulate because now the field modes have their own basis $|k\rangle$. A viable procedure to solve this problem is to work in the *Schrödinger Picture*, where the time evolution is all contained within the eigenstates, and, afterward, to resort to the Time-Dependent Perturbation Theory (TDPT) at its first order term. So, considering that the unperturbed system $\mathbf{H}_0$ is formed by the two-level atom plus the Electromagnetic field Hamiltonians (*i.e.* $\mathbf{H}_0 = \mathbf{H}_{At} + \mathbf{H}_{EM}$) and that $\mathbf{H}_{Int}$ is the perturbation of system, which must be much smaller than $\mathbf{H}_0$ to guarantee the correct employment of the TDPT.

On intuitive grounds one may claim that the $\mathbf{H}_{At}$ and $\mathbf{H}_{EM}$ commute, which is equivalent to say two important features: that a common base exists and is given by the tensorial product $|n,k\rangle = |n\rangle \otimes |k\rangle$ where n stands

for the two-level eigenstates and k for the states corresponding to the SPP normal modes; the time evolution for the TLA and the SPP may be solved independently as if they were isolated, from where it may be adopted the following wave-function

$$\psi^0(r,t) = \sum_{n,k} c_{n,k}\, e^{-i\frac{(E_n+E_k)}{\hbar}t}\, |n,k\rangle \tag{4.16}$$

where $|n,k\rangle$ and $|c_{n,k}|^2$ are, respectively, the spatial dependence and the density probability for each orthogonal mode of the wave-function. E_n is the eigenenergy of the n state of the TLA and E_k is the eigenenergy of the k mode of the SPP.

Although this is only valid for the unperturbed system $\mathbf{H}_0$, the strategy to solve the temporal evolution of the system accounting with the perturbation is to assume that the system modification along the time can be fully captured just by including a time dependence in the coefficient $c_{n,k}(t)$. By doing that the new wave-function (in Eq. 4.17) can be inserted in the *Schrödinger* equation (in Eq. 4.18) resulting, after some simple algebra manipulation and by simplifying the notation of $|n,k\rangle$ modes in merely $|n\rangle$ (without any loss of information), into Eq. 4.19.

$$\psi(r,t) = \sum_{n,k} c_{n,k}(t)\, e^{-i\frac{(E_n+E_k)}{\hbar}t}\, |n,k\rangle \tag{4.17}$$

$$i\hbar\frac{\partial}{\partial t}\psi(r,t) = \mathbf{H}_{Tot}\,\psi(r,t) \tag{4.18}$$

$$i\hbar\sum_n \dot{c}_n(t)\, e^{-i\frac{E_n}{\hbar}t}\, |n\rangle = \mathbf{H}_{Int}\sum_n c_n(t)\, e^{-i\frac{E_n}{\hbar}t}\, |n\rangle \tag{4.19}$$

Furthermore, by recalling that the interaction Hamiltonian can also be decomposed as in Eq. 4.20, one may check that by multiplying on the left side of Eq. 4.19 by $\langle f|$ and isolating the term $\dot{c}_f(t)$, it is achieved the equality present in Eq. 4.21.

$$\mathbf{H}_{Int} = \sum_m \sum_n |m\rangle\langle m|\,\mathbf{H}_{Int}\,|n\rangle\langle n| \tag{4.20}$$

$$\dot{c}_f(t) = -\frac{i}{\hbar}\sum_m \langle f|\,\mathbf{H}_{Int}\,|n\rangle\, c_n(t)\, e^{-i\frac{\left(E_n-E_f\right)}{\hbar}t} \tag{4.21}$$

To find out the structure of $c_n(t)$, it is imposed the initial condition that, at the time instant $t=0$, the system is found in the state $|i\rangle$, *i.e.*, $c_n(t=0)$ is zero for all n except for $n=i$, being equal to one in this case. The first term of the TDPT is now used by affirming that $c_n(t)$ can be approximated by its value at the initial condition instant. Thus, the integration of $\dot{c}_f(t)$ yields to the expression in Eq. 4.22, which is a very well known formula denominated by Fermi's Golden Rule (FGR) [72, 77].

$$c_f(t) = -\frac{i}{\hbar}\int_0^t \langle f|\,\mathbf{H}_{Int}\,|i\rangle\, e^{-i\frac{\left(E_i-E_f\right)}{\hbar}t'}\,dt' \tag{4.22}$$

The FGR is used to compute the probability over time of an initial state $|i\rangle$ ending up in a final state $|f\rangle$ and the foundation behind its derivation is associated with the first order term of the TDP theory. Despite the extensive use of this method by researchers, it is important to emphasize that the validity of the FGR depends on the time intervals that are considered [78].

Therefore, to compute the probability of the system to transit from the initial state $|i\rangle$ into the final state

$|f\rangle$, which is defined as $P_{i\to f}(t) = |c_f(t)|^2$ and may also be written as in Eq. 4.23 through the FGR.

$$P_{i\to f}(t) = \frac{1}{\hbar^2}\left|\langle f|\,\mathbf{H}_{Int}\,|i\rangle \int_0^t e^{-i\frac{\left(E_i-E_f\right)}{\hbar}t'}dt'\right|^2 \tag{4.23}$$

For the present case, the interaction Hamiltonian has no time dependence because we are working in the *Schrödinger Picture*. Therefore, the integral is solvable and leads to Eq. 4.24, where $\omega_{fi} = \frac{E_f - E_i}{\hbar}$ is the introduced variable with frequency units associated with the difference between the eigenenergies of the final and initial state, correspondingly.

$$P_{i\to f}(t) = \frac{t^2}{\hbar^2}|\langle f|\mathbf{H}_{Int}\,|i\rangle|^2 \mathrm{sinc}\Big(\frac{\omega_{fi}}{2}t\Big)^2 \tag{4.24}$$

At this point, one may wonder which initial and final states are we interested in. To become clear, the goal is to calculate the spontaneous emission rate. Thus, the initial state must correspond to the excited state of the TLA and to absence of photons, *i.e*, the initial state is $|e,0\rangle$. On the other hand, the final state corresponds to the TLA being on the ground state and to the emergence of one (and only one) SPP photon, that can be represented as $\sum_k |g,1_k\rangle$, where the subscript k is associated with all possible light modes. Therefore, the transition probability for this particular case is given as in Eq. 4.25, where basically $\mathbf{H}_{Int}$ is substituted by the electric dipole momentum and the electric field operators, and the final state becomes a sum over all possible SPP modes.

$$P_{i\to f}(t) = \frac{t^2}{\hbar^2}\sum_k \left|\langle g,1_k|\left[\overrightarrow{\gamma}\sigma^- + \overrightarrow{\gamma}^*\sigma^+\right]\cdot\sqrt{\frac{\hbar\omega_k}{2}}\left(\widehat{\mathbf{a}}_k\overrightarrow{\mathbf{E}}_k(r) + \widehat{\mathbf{a}}_k^\dagger\overrightarrow{\mathbf{E}}_k^*(r)\right)|e,0\rangle\right|^2 \mathrm{sinc}\Big(\frac{\omega_{fi}}{2}t\Big)^2 \tag{4.25}$$

It is trivial to deduce that the only the term resulting from the distributive multiplication that remains non-zero is the one containing the σ^- and $\widehat{\mathbf{a}}_k^\dagger$ operators. Consequently, the initial and final energies are $E_i = \hbar\frac{\omega_0}{2}$ and $E_f = \hbar\left(-\frac{\omega_0}{2}+\omega\right)$, respectively, where ω is the frequency extracted from the relation $\widehat{\mathbf{a}}_k^\dagger(t) = e^{i\omega t}\,\widehat{\mathbf{a}}_k^\dagger$. Bearing this in mind the transition probability comes as visible in Eq.4.26.

$$P_{i\to f}(t) = \frac{t^2}{\hbar^2}\sum_k \left|\sqrt{\frac{\hbar\omega_k}{2}}\vec{\gamma}\cdot\overrightarrow{\mathbf{E}}_k(r)\right|^2 \mathrm{sinc}\Big(\frac{\omega_{fi}}{2}t\Big)^2 \tag{4.26}$$

A rigorous analysis regarding the FGR is exploited at [77, 78], where is used the premise of letting $t\to\infty$ and that $\omega_{fi}\approx 0$ which is to say that the frequency regime is near the resonance. These considerations allow the replacement of the $\mathrm{sinc}()$ by a δ function, since the former function becomes sharply peaked at the resonance. Also, attending to the known integral formula $\int_{-\infty}^{\infty} d\omega \frac{2}{\pi}\frac{\sin^2\left(\frac{\omega t}{2}\right)}{\omega^2 t} = 1$, it is quite simple to check that the correct normalization leads to the expression Eq. 4.27.

$$\Gamma_{sp}(\omega) = \frac{2\pi}{\hbar^2}\sum_k \left|\sqrt{\frac{\hbar\omega_k}{2}}\vec{\gamma}\cdot\overrightarrow{\mathbf{E}}_k(r)\right|^2 \delta(\omega_{fi}) \tag{4.27}$$

The latter equation is known as the transition rate, defined as $\Gamma_{sp}(t) = \lim_{t\to\infty}\frac{P_{i\to f}(t)}{t}$, and specifically, in this case, measures the number of photons emitted per time unit. This is a result that is widely employed in atomic transitions problems [79], where the frequency is near the resonance.

Leaving the details of the Electric field structure aside, it is known that the possible wave-guided modes of the surface plasmons can propagate either along the $\hat{x}$, or the $\hat{y}$ direction. Therefore, it is necessary to account with all these modes ($\sum_{k_x,k_y}$), which by invoking the periodic boundary conditions admits the replacement of the sum by an integral ($\sum_{k_x,k_y} \to \frac{L^2}{(2\pi)^2}\iint dk_y dk_x$). Moreover, due to properties of the Dirac delta function, the only contribution for the integral comes from the wavevector k_0 associated with the frequency of the electric field

$\omega = \omega_0$. Bearing this in mind, it becomes useful to change the variables coordinate system from Cartesian to Polar ($k_x = k\cos\phi$ and $k_y = k\sin\phi$), since the computation of the integral is now limited to a circumference of radius $k = k_0$. Here, k_0 corresponds to $k_\parallel$ (having the dispersion equation mentioned in Eq. 3.18) since $\omega_0 = \omega$. Consequently, the expression of the spontaneous emission is modified, as one may check in Eq. 4.28.

$$\Gamma_{sp}(\omega) = \frac{L^2}{2\pi\hbar^2}\int_0^{2\pi} d\phi \int_0^{\infty} k_0 \left|\sqrt{\frac{\hbar\omega_0}{2}}\vec{\gamma}\cdot\overrightarrow{\mathbf{E}}_{k_0}(r)\right|^2 \delta(\omega-\omega_0)\,dk \tag{4.28}$$

Also, resorting once again to the property of the Dirac delta ($\int f(x)\,\delta(g(x))dx = \frac{f(x_0)}{|g'(x_0)|}$), one attains to the result at Eq. 4.29.

$$\Gamma_{sp}(\omega) = \frac{L^2}{2\pi\hbar^2}\int_0^{2\pi} d\phi k_0 \frac{\left|\sqrt{\frac{\hbar\omega_0}{2}}\vec{\gamma}\cdot\overrightarrow{\mathbf{E}}_{k_0}(r)\right|^2}{\left|\frac{\partial\omega_0}{\partial k}\right|} \tag{4.29}$$

In addition, one may also write $\frac{\partial\omega_0}{\partial k}$ as the gradient of ω_0 since the gradient of a function in these coordinates is given by $\nabla f = \frac{\partial f}{\partial k}\widehat{k} + \frac{1}{k}\frac{\partial f}{\partial\theta}\widehat{\theta}$ and ω_0 has no dependence in the θ. Furthermore, one may yield to Eq. 4.30 attending that the angular integration leads to a multiplication factor of 2π, since the system is rotational invariant over θ.

$$\Gamma_{sp}(\omega) = \frac{k_0 L^2}{\hbar^2}\frac{\left|\sqrt{\frac{\hbar\omega_0}{2}}\vec{\gamma}\cdot\overrightarrow{\mathbf{E}}_{k_0}(r)\right|^2}{|\nabla\omega_0|} \tag{4.30}$$

The derivative $\frac{\partial\omega}{\partial k}$ is easily extracted, as shown in Eq. 4.31, by using the dispersion equation deduced in the previously Chapter 3.

$$\frac{\partial\omega}{\partial k} = \frac{\beta}{2} + \frac{1}{2}\frac{k\beta^2}{\sqrt{k^2\beta^2+4\omega_{sp}^2}} \tag{4.31}$$

Furthermore, it is assumed that for the sake of simplicity the electric dipole vector is aligned in the $\hat{z}$ direction. This implies that the only component of the electric field operator that will contribute to the dot product is the one parallel to $\hat{z}$. In this condition and letting unspecified the function of the electric dipole element γ, the transition rate becomes Eq. 4.32.

$$\Gamma_{sp}(\omega) = \frac{k_0 L^2\omega_0}{\hbar}\frac{|\gamma|^2|E_{k_0}(r_0)|^2}{\left|\beta + \frac{k_0\beta^2}{\sqrt{k_0^2\beta^2+4\omega_{sp}^2}}\right|} \tag{4.32}$$

Therefore, the last term to compute in order to obtain the transition rate is the square of the electric field in the $\hat{z}$ direction, where its only relevant branch is for $z > 0$, since the TLA is above the metal slab. It is straightforward to check that this term yields to the expression Eq. 4.33, which at last leads to the transition rate in Eq. 4.34.

$$|E_{k_0}(r_0)|^2 = k_\parallel^2\,|B|^2\,e^{-2k_0 r_0} \tag{4.33}$$

$$\Gamma_{sp}(\omega) = \frac{k_0^3 L^2\omega_0}{\hbar}\frac{|\gamma|^2|B|^2 e^{-2k_0 r_0}}{\left|-\beta + \frac{k_0\beta^2}{\sqrt{k_0^2\beta^2+4\omega_{sp}^2}}\right|} \tag{4.34}$$

As mentioned earlier, because of the chosen coordinate system, the position of the TLA nucleus can be represented in terms of z, being its length r_0.

In addition, as it was stated before and as one may check in Figure 3.9, the normalization coefficient $|B|$ is almost constant for frequencies in the interval $[\omega_{sp}, \omega_p]$. In this regime, $|B|$ has a similar value to that of the local approach ($\frac{1}{\sqrt{2L^2\varepsilon_0 k_\parallel}}$). Consequently, the emission rate in this approximation is given by Eq.4.35.

$$\Gamma_{sp}(\omega) = \frac{k_0^2 \omega_0}{2\hbar\varepsilon_0 \beta} \frac{|\gamma|^2 e^{-2k_0 r_0}}{\left|1 + \frac{k_0\beta}{\sqrt{k_0^2\beta^2 + 4\omega_{sp}^2}}\right|} \tag{4.35}$$

The variation of the emission rate for different values of the atomic frequency ω_0 is displayed in Figure 4.2, where, besides the formula in Eq. 4.34, it was also plotted the curve with the approximated expression (Eq. 4.35). It is observed that the plot has a peak near the ω_{sp}, being practically zero, elsewhere. Furthermore, the approximated expression is observed to be slightly above the amplitudes of the exact one, where the maximum amplitude is around the 3.6×10^3 THz which is about 130 times lower than the surface plasmon frequency. For the computation of the emission rate, it was considered that the distance between the plasmonic interface and the TLA $r_0 = 10\text{nm}$, which is an overstatement since quantum dots themselves typically have diameters of a few nanometers scale [80]. However, this assumption is imposed to ensure a strong coupling, which one may infer by observing Figure 4.3. As r_0 decreases, the emission rate peak increases its amplitude and widens its width (*i.e.*, interval of frequencies whose contribution is relevant also increases). This seems reasonable since the closer the unperturbed systems are from each other, the more intense their interaction becomes. In addition, the electric dipole moment employed for the computation of the emission rate corresponds to the *Rydberg atoms* [81]. These atoms are very appealing because of their strong responses in the presence of electric fields, which is explained by the high electric dipole moment value which is approximately $\gamma \approx 1212 \times 10^{-30}$ C m ≈ 364 C m [81]. Although the typical values of the electric dipole moment for most of the atoms and molecules are of a few *Debye*, the elected quantum object is the *Rydberg* atom, because it allows strong couplings between the TLA and the SPP to be achieved.

Also, from Eq. 4.35 it is possible to infer that at $\omega = \omega_{sp}$ the emission rate will vanish, since the wave vector also vanishes at that frequency. Nevertheless, the plot in Figure 4.2 shows that for frequencies slightly above ω_{sp} the emission increases extremely fast and has its maximum value in that region. This has some similarities with the emission rate in the local SPP model (that is commented further), since that, although the peak is not exactly a *Dirac delta* at $\omega = \omega_{sp}$, it possesses a narrowed finite peak in the vicinity of that frequency.

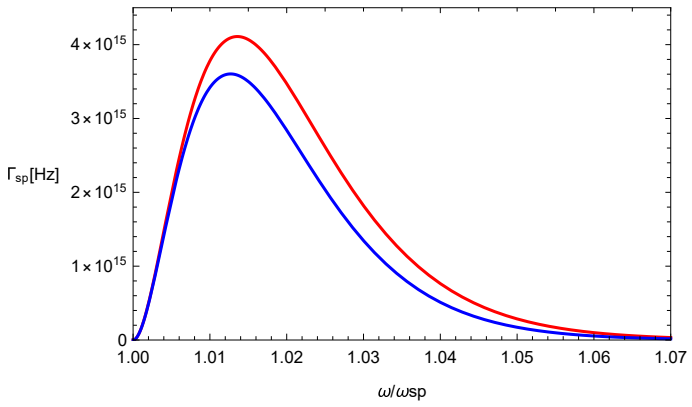

Figure 4.2: The graphic shows the Emission rate of the SPP in a non-local silver slab, where $\omega_{sp} \approx 2\pi \times 646 \times 10^{12}$[Hz] and $\beta \approx 0.0036c$ [m] (being c the speed of light). The blue curve corresponds to the exact expression of the normalization constant ($|B|$), while the red curve is assigned to the the emission rate formula where $|B|$ is approximated by $\frac{1}{\sqrt{2L^2\varepsilon_0 k_\parallel}}$.

To demonstrate how the presence of the metal slab in the vicinity of a TLA alters the emission rate of this one, it is made the contrast with the free space emission rate. As strange as it seems, the TLA in free space

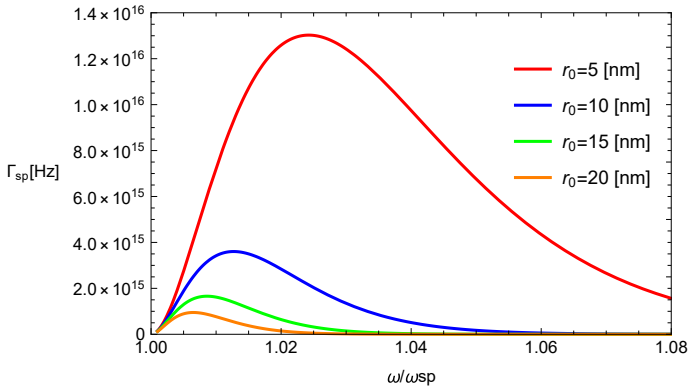

Figure 4.3: The graphic shows the plot of the emission rate of the SPP in a non-local silver slab, for different values of r_0. The red, blue, green and orange curves correspond to diffusion strengths of $r_0 = 5$ nm, $r_0 = 10$ nm, $\$r_0 = 15$ nm and $r_0 = 20$ nm, respectively.

also emits photons through the mechanism of spontaneous emission, although that in this case the formula [38, 82, 83] is given by Eq. 4.36.

$$\Gamma_0(\omega) = \frac{|\gamma|^2}{3\pi\hbar\varepsilon_0}\left(\frac{\omega_0}{c}\right)^3 \tag{4.36}$$

Hence, the comparison between both emission rates is illustrated in Figure 4.4, where is plotted the ratio Γ_{s0}/Γ_0. This graphic shows that the emission rate in the presence of the metal substrate can achieve values about 8000 times higher than in the case where it is absent. This is explained by the coupling that exists between the metal and the atom that allows an energy transfer from the atom to the metal and vice-versa.

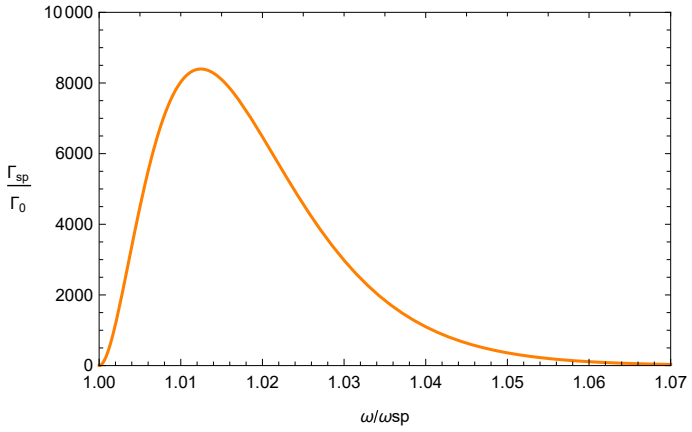

Figure 4.4: The graphic shows the spontaneous emission rate ratio between the nonlocal surface plasmon and the two dimensional free space spontaneous emission rates. The frequency interval corresponds to the vicinity of ω_{sp}. It is considered a silver metal slab, where its $\omega_{sp} \approx 2\pi \times 646 \times 10^{12}$[Hz] and $\beta \approx 0.0036c$ [m] (being c the speed of light).

Besides the comparison between the emission rate of the non-local metal with the free TLA in free space, it should also be made the correlation of the derived Γ_{sp} with its analogous in the case where a local approach is employed. If the quasi-static approximation is not employed, one easily confirms, by looking to Eq. 4.28, that the emission rate is infinite at $\omega = \omega_{sp}$ and zero otherwise. This happens because ω_{sp} is the only frequency for which wave modes are supported, and consequently the *Dirac* δ-function becomes $\delta(\omega - \omega_{sp})$. In contrast, Γ_{sp} has a high but finite peak in the vicinity of ω_{sp} and allows the emission of photons with different energies (frequencies), though the higher emission is verified in a short range near the surface plasmon resonance.

In addition, if one uses the *Drude's model* to describe the SPP in the electrostatic regime, then the emis-

sion rate will endorse the form given in Eq. 4.37, wherein its derivation was used the approximation $k(\omega) \approx \frac{\sqrt{\omega_{sp}^3}}{2c}\frac{1}{\sqrt{\omega_{sp}-\omega}}$ that is valid for frequencies near ω_{sp} [2, 38].

$$\Gamma_{Local} = \frac{|\gamma|^2 e^{-2k_0 r_0}}{16\hbar\varepsilon_0}\frac{\omega_{sp}^4}{(\omega_0-\omega_{sp})^2 c^2} \tag{4.37}$$

It should not be strange that the interval of frequencies which has more contribution to the emission rate is near the ω_{sp} because of the approximation of the *Dirac delta* in the *Fermi Golden Rule*. Indeed, this approximation implies that the only way to exist emission rate is in the case where the SPP waves have at least one radiation mode with frequency equal to the atomic frequency ω_0. Therefore, this must be intimately linked with the density of states (addressed in the previous Chapter) which provides a congruent explanation of the Emission rate, due to the high density that is verified for the frequencies near ω_{sp}.

Furthermore, this also explains why that, unlike to the predictions provided by the local theory where the emission rate explodes at $\omega = \omega_{sp}$, in the spatial dispersive model where no radiation mode is supported is witnessed no emission of photons. To reinforce this link between the DOS and the emission rate, one can start by visualizing in Eq. 4.27 that some resemblances with the DOS formula are evident. The latter equation can further be rearranged in the convenient form presented in Eq. 4.38 where $\mathbf{E}_{\hat{z},k}(r)$ is the component of the electric field parallel to the electric dipole moment, that without loss of generality is said to be in the $\hat{z}$ direction.

$$\Gamma(\omega) = \frac{2\pi}{\hbar^2}\frac{\hbar\omega_k}{2}|\gamma|^2\sum_k |\mathbf{E}_{\hat{z},k}(r)|^2\delta(\omega_k-\omega_0) \tag{4.38}$$

Hence, it is only needed a term with lengths of area (or volume for the 3D analysis) to the DOS formula emerge in Eq. 4.38. Actually, it is possible to inspect from the formula that gives the normalization of the Electromagnetic field modes, that since integration in the three dimensional space ($\int dx \int dy \int dz$) has units of volume, somehow the integrand (${E_{nk}}^* \cdot \frac{\partial[\omega\varepsilon(z,\omega)]}{\partial\omega} \cdot E_{nk}$) must have units of m^{-3}, in order to obtain an adimensional scalar. Since the term $\frac{\partial[\omega\varepsilon(z,\omega)]}{\partial\omega}$ will produce a result with units of permittivity, then the square of the electric field must have the m^{-3} dependence in its dimensions.

In free space, since the electric field is given by plane waves, it is clear from the modes normalization formula that $|\mathbf{E}_{\hat{z},k}(r)|^2 = \frac{1}{3L^3\varepsilon_0}$. Hence, one can rewrite the emission rate of the free space in terms of the DOS for the 3D space, which is displayed in Eq. 4.39, where it was used the definition of the DOS present in Eq. 3.22.

$$\Gamma_0(\omega) = \frac{\pi\omega_0}{3\hbar}\frac{|\gamma|^2}{\varepsilon_0}n(\omega)_{3D} \tag{4.39}$$

Similarly, an analogous procedure can be undertaken for $\Gamma_{sp}(\omega)$ where the expression of $\left|\mathbf{E}_{\hat{z},k}(r)\right|^2$ is already known and may be reviewed in Eq. 4.33. Thus, the relation between $n(\omega)_{2D}$ and $\Gamma_{sp}(\omega)$ is clearly given by Eq. 4.40.

$$\Gamma_0(\omega) = \frac{\pi\omega_0 k_0}{2\hbar}\frac{|\gamma|^2}{\varepsilon_0}e^{-2k_0 r_0}n_{sp}(\omega) \tag{4.40}$$

This dependence of the emission rate on the density of states justifies the correlation that is observed in their response over the frequency. Thereby, a system will emit more photons per unit of time in the frequencies that present a higher DOS. The comparison between $\Gamma_{sp}(\omega)$ and $\Gamma_0(\omega)$ can be done in terms of their DOS's and is exhibited in Eq. 4.41.

$$\frac{\Gamma_{sp}(\omega)}{\Gamma_0(\omega)} = \frac{3k_0}{2}e^{-2k_0 r_0}\frac{n_{sp}(\omega)}{n(\omega)_{3D}} \tag{4.41}$$

The influence of the nonlocality in the emission rate can be comprehended by inspection of Eq. 4.35. Then, if one replaces the wave vector in terms of ω, then it can be perceived that at the local limit scenario ($\beta \to 0$) the

transition rate has the limit $\Gamma_{\beta\to 0} = \frac{1}{\beta} e^{\frac{-\left(\omega^2-\omega_{sp}^2\right)}{\beta}}$. Thus, in the case of having $\omega \neq \omega_{sp}$, the limit goes to zero. Otherwise, the exponential term falls into an indeterminate form, that in the case of being a finite result it will yield to an infinite emission rate. This is in agreement with the behavior from the local SPP, since the density of states near the resonance frequency is infinite. In Figure 4.5 the plots of $\Gamma_{sp}(\omega)$ for different values of β are represented, from where it is concluded that as the diffusion effects become weaker, the peak in the emission rate becomes more narrowed around ω_{sp} and amplitude of the maximum increases. Attending to this behavior it is reasonable to infer that with $\beta = 0$ the $\Gamma_{sp}(\omega)$ will become a *Dirac delta* at $\omega = \omega_{sp}$, as the predicted by the local scenario.

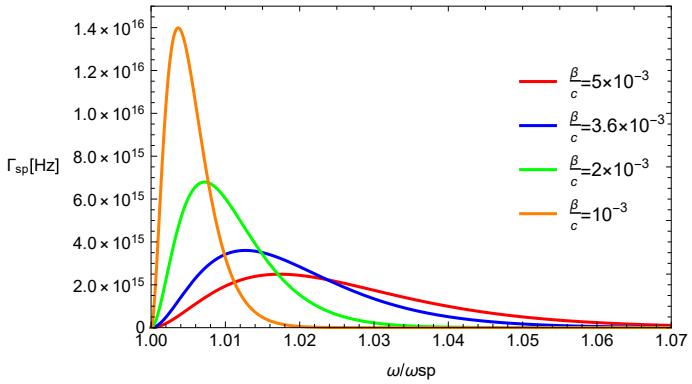

Figure 4.5: The graphic shows the plot of the Emission rate of the SPP in a non-local silver slab, for different values of β. The red, blue, green and orange curves correspond to diffusion strengths of $\frac{\beta}{c} = 5 \times 10^{-3}$, $\frac{\beta}{c} = 3.6 \times 10^{-3}$, $\frac{\beta}{c} = 2 \times 10^{-3}$ and $\frac{\beta}{c} = 10^{-3}$, respectively.

Chapter 5

Local SPP - Atom Quantum Interaction

5.1 Hamiltonian Reformulation

The interaction that emerges between a TLA and surface plasmon electromagnetic waves, when placing the atom in the vicinity of a metal slab is examined in this chapter. Moreover, it is intended to observe what the possible states for such system are and how does the probability of measuring a given state change over time. Thus, it is imposed that the initial state of the apparatus corresponds to having the TLA in an excited state and the absence of photon emission ($|e,0\rangle$). This is a mere matter-light interaction problem, as seen previously when discussing the *Rabi Oscillations* features, although that, in this case, the Electromagnetic field is composed of infinite quantized harmonic oscillator modes.

Before proceeding to the specific problem situation, is important to revise the general case for a given quantized electromagnetic source. For a basic apparatus containing a TLA and a cavity supporting infinite bosonic modes associated with infinite different frequencies, the interaction examination imposes an overwhelming barrier to the analytical treatment of the problem. The reason lies in the infinite nature of the light eigenmodes that does not allow an exact description of the system's dynamics.

However, the same does not succeed in the case of multi-level atoms interacting with a few quantized light modes, where plenty of research was already performed [84]. For instance, G. Benivegna *et al.* at [85] investigated the dynamical details on the interaction of a TLA with several quantized electromagnetic wave modes.

Many complex models to characterize bosonic-matter interactions exist as the Dicke model [86]. However, for this type of problems, the elected approach is the Jaynes–Cummings Model (JCM) [87]. The reasoning behind it lies in its simpler treatment and the good match that provides between its predictions and the experimental results. This model has picked the interest of many researchers because it yields reliable insights in areas such as solid-state physics quantum optics [88]. Examples of this approach applications are the description of ultra-cold Rydberg atoms interacting with light modes at [88] and the quantum entanglement modeling of atoms that interact with light fields in a cavity [89].

Yet, the approach that will be carried away is not exactly the JCM because, unlike this one, that uses the *RWA*, no approximation is made here. Later on, it will be evaluated the differences between the results that the application of the *RWA* would lead in comparison to our procedure.

One may question that since our problem contains an infinite sum of SPP light modes, then it would be unattainable to reach a solution for the *Schrödinger equation*. However, for a specific scenario where all the radiation modes are associated with a unique frequency, the *Hamiltonian* can be reformulated to a much simpler version that enables the computation of its time evolution. This feature occurs due to a degeneracy in the light eigenmodes that enables a modification in the basis. Hence, the SPP waves in the local model can have their time evolution derived, since they present a density of states that diverges at $\omega = \omega_{sp}$. The lossless *Hamiltonian*

for the SPP in the quasi-static approximation interacting with the TLA may be written as in Eq. 5.1

$$\hat{\mathbf{H}} = \frac{\hbar\omega_{sp}}{2}\sum_{\omega_k>0}\left(\hat{\mathbf{a}}_k\hat{\mathbf{a}}_k^\dagger + \hat{\mathbf{a}}_k^\dagger\hat{\mathbf{a}}_k\right) + \frac{\hbar\omega_0}{2}\hat{\boldsymbol{\sigma}}_z - (\gamma^*\hat{\boldsymbol{\sigma}}^+ + \gamma\hat{\boldsymbol{\sigma}}^-)\cdot\hat{\mathbf{E}}(r_0) \tag{5.1}$$

where the first term of the right side of equation is the electromagnetic field *Hamiltonian*, the second is the habitual TLA and the last term represents their interaction.

Therefore, in order to present a new reformulation of the *Hamiltonian*, the dynamics of the relevant operators in the *Heisenberg* picture is computed by attending that the time evolution of an operator $\hat{\Omega}$ is given by $\frac{d\hat{\Omega}}{dt} = \frac{i}{\hbar}\left[\hat{H},\hat{\Omega}\right]$. Then, one can easily confirm that either Eq. 5.2 and Eq. 5.3 hold true.

$$\frac{d\hat{\boldsymbol{\sigma}}^-}{dt} = -i\omega_0\hat{\boldsymbol{\sigma}}^- - \frac{i}{\hbar}\gamma\cdot\hat{\mathbf{E}}(r_0)\hat{\boldsymbol{\sigma}}_z \tag{5.2}$$

$$\frac{d\hat{\mathbf{a}}_k}{dt} = -i\omega_{sp}\hat{\mathbf{a}}_k + \frac{i}{\hbar}\hat{\boldsymbol{\mu}}\cdot\sqrt{\frac{\hbar\omega_{sp}}{2}}\mathbf{E}_k^*(r_0) \tag{5.3}$$

where the electric field operator is $\hat{\mathbf{E}}(r_0) = \sum_k^\infty \sqrt{\frac{\hbar\omega_{sp}}{2}}\left(\hat{\mathbf{a}}_k\hat{\mathbf{E}}_k(r_0) + \hat{\mathbf{a}}_k^\dagger\hat{\mathbf{E}}_k^*(r_0)\right)$. Moreover, it can be represented compactly by the sum of $\hat{\mathbf{E}}_-(r_0)$ and $\hat{\mathbf{E}}_+(r_0)$, where $\hat{\mathbf{E}}_-(r_0) = \sum_k^\infty \sqrt{\frac{\hbar\omega_{sp}}{2}}\hat{\mathbf{a}}_k\hat{\mathbf{E}}_k(r_0) = \hat{\mathbf{E}}_+^*(r_0)$.

Also, assuming once more that the transition dipole moment operator is oriented along $\hat{z}$, one can inspect that the commutator $\left[\hat{z}\cdot\hat{\mathbf{E}}_-(r_0), \hat{z}\cdot\hat{\mathbf{E}}_+(r_0)\right]$ results in Eq. 5.4.

$$\left[\hat{z}\cdot\hat{\mathbf{E}}_-(r_0), \hat{z}\cdot\hat{\mathbf{E}}_+(r_0)\right] = \frac{\hbar\omega_{sp}}{2}\sum_k\left|\hat{z}\cdot\hat{\mathbf{E}}_k(r_0)\right|^2 = \frac{L^2}{(2\pi)^2}\frac{\hbar\omega_{sp}}{2}\int_{-\infty}^{\infty}\int_{-\infty}^{\infty}dk^2\left|\hat{z}\cdot\hat{\mathbf{E}}_k(r_0)\right|^2 \tag{5.4}$$

In the last step, it was invoked the periodical boundary condition method to transform the sum into an integral. Furthermore, since $\left|\hat{z}\cdot\hat{\mathbf{E}}_k(r_0)\right|^2 = |B|^2k_\parallel^2e^{-2k_\parallel r_0}$ and the square of the normalization coefficient at the surface plasmon resonance is equal to $|B(\omega=\omega_{sp})|^2 = \frac{1}{2\varepsilon_0k_\parallel^2L^2}$, then we obtain Eq. 5.5.

$$\left[\hat{z}\cdot\hat{\mathbf{E}}_-(r_0), \hat{z}\cdot\hat{\mathbf{E}}_+(r_0)\right] = \frac{\hbar\omega_{sp}}{16\pi^2\varepsilon_0}\int_{-\infty}^{\infty}\int_{-\infty}^{\infty}dk_\parallel{}^2k_\parallel e^{-2k_\parallel r_0} \tag{5.5}$$

The integral of Eq. 5.5 is integrable by parts, from where the equality, $\int_{-\infty}^{\infty}\int_{-\infty}^{\infty}dk_\parallel{}^2k_\parallel e^{-2k_\parallel r_0} = \frac{\pi}{2}\frac{1}{r_0^3}$, can be extracted. Thereby, the commutator is simply given by Eq. 5.6.

$$\left[\hat{z}\cdot\hat{\mathbf{E}}_-(r_0), \hat{z}\cdot\hat{\mathbf{E}}_+(r_0)\right] = \frac{1}{32\pi}\frac{\hbar\omega_{sp}}{\varepsilon_0r_0^3} \tag{5.6}$$

We are now able to introduce a normalized operator $\hat{\mathbf{c}}_k$ (defined at Eq. 5.7), that has a significant contribution to the reformulation of the *Hamiltonian*.

$$\hat{\mathbf{c}}_k = \sqrt{\frac{32\pi r_0^3\varepsilon_0}{\hbar\omega_{sp}}}\hat{z}\cdot\hat{\mathbf{E}}_-(r_0) \tag{5.7}$$

Besides, it has the analogous commutation relation property of the bosonic operators since $\left[\hat{\mathbf{c}}_k, \hat{\mathbf{c}}_k^\dagger\right] = 1$.

To compute the dynamics of $\hat{\mathbf{c}}_k$ is convenient to first determine the time evolution of $\hat{\mathbf{E}}_-(r_0)$, that is exhibited in Eq. 5.8.

$$\frac{d\hat{\mathbf{E}}_-(r_0)}{dt} = -i\omega_{sp}\hat{\mathbf{E}}_-(r_0) + i\frac{\omega_{sp}}{2}\sum_k^\infty\hat{\mathbf{E}}_k(r_0)\hat{\mu}\cdot\hat{\mathbf{E}}_k^*(r_0) \tag{5.8}$$

So, merely by combining the Eq. 5.8 and the definition of $\hat{\mathbf{c}}_k$ at Eq. 5.7, and noticing that $\sum_k \left|\hat{z}\cdot\hat{\mathbf{E}}_k(r_0)\right|^2 = \frac{1}{16\pi\varepsilon_0 r_0^3}$, the dynamics of $\hat{\mathbf{c}}_k$ are simply given by 5.9.

$$\frac{d\hat{\mathbf{c}}_k}{dt} = -i\omega_{sp}\hat{\mathbf{c}}_k + \frac{i}{\hbar}\sqrt{\frac{\hbar\omega_{sp}}{32\pi\varepsilon_0 r_0^3}}\left(\gamma^*\hat{\sigma}^+ + \gamma\hat{\sigma}^-\right) \tag{5.9}$$

To understand better the interrelation between $\hat{\mathbf{c}}_k$ and the transition operators of the TLA ($\hat{\sigma}^+$and $\hat{\sigma}^-$), one can rewrite Eq. 5.2 in terms of the new operator $\hat{\mathbf{c}}_k$ as represented in Eq. 5.10.

$$\frac{d\hat{\sigma}^-}{dt} = -i\omega_0\hat{\sigma}^- + \frac{i}{\hbar}\sqrt{\frac{\hbar\omega_{sp}}{32\pi\varepsilon_0 r_0^3}}\left(\hat{\mathbf{c}}_k + \hat{\mathbf{c}}_k^\dagger\right) \tag{5.10}$$

From where one may infer that these two operators, $\hat{\mathbf{c}}_k$ and $\hat{\sigma}^-$, can have an oscillatory nature, since their variations decrease with their own magnitudes and increase with the other's operator magnitude. Furthermore, these two last equations are precisely the ones that what one would obtain for a fictitious system containing the following *Hamiltonian*

$$\hat{\mathbf{H}} = \frac{\hbar\omega_{sp}}{2}\hat{\mathbf{c}}^\dagger\hat{\mathbf{c}} + \frac{\hbar\omega_0}{2}\hat{\sigma}_z - (g\hat{\sigma}^+ + g^*\hat{\sigma}^-)\cdot\left(\hat{\mathbf{c}} + \hat{\mathbf{c}}^\dagger\right) \tag{5.11}$$

where $g = \gamma^*\sqrt{\frac{\hbar\omega_{sp}}{32\pi\varepsilon_0 r_0^3}}$ and represents the coupling strength between the two unperturbed systems. At first glance, it is evident the similarity of this *Hamiltonian* with one having a unique quantized light mode, that interacts with a TLA in the dipole approximation. Here, the last term represents the $\hat{\mathbf{H}}_{int}$ and the γ^* is substituted by g, which now also accounts with the distance of the metal slab to the atom and also on the work frequency. This problem is similar to the previously addressed case of a TLA interacting with a classical monochromatic wave. Therefore, we expect that some sort of *Rabi Oscillations* phenomenon will also be present in this scenario. Nonetheless, a different feature is now included due to the quantization of the Electromagnetic field that supports an infinite number of eigenstates, each associated with the number of photons existent in that state.

5.2 Lossless Interaction of SPP-TLA

The inspection of the system's time evolution will be followed by a change to the *Schrödinger picture*, where it will be the main goal of this section to solve the *Schrödinger* equation for the *Hamiltonian* in Eq. 5.11. Nevertheless, the latter *Hamiltonian* does not take into consideration the dispersion of energy through loss channels. However, as discussed before, the spontaneous emission of SPP photons is one of the reasons for which the energy is not conserved, because the photons that travel along the metal surface are irreversible lost into the environment. Due to the importance of this phenomenon, both the lossless and the loss scenarios will be worthy of attention.

Beginning first with the lossless situation, it is considered a general and convenient wavefunction, presented at Eq. 5.12, that can be a solution of the system and that already contains the time evolution of the unperturbed systems.

$$|\psi(t)\rangle = \sum_n c_n(t)\, e^{-i\frac{\omega_0}{2}t}e^{-i\omega_{sp}nt}\,|e,n\rangle + \tilde{c}_n(t)\, e^{i\frac{\omega_0}{2}t}e^{-i\omega_{sp}nt}\,|g,n\rangle \tag{5.12}$$

Introducing this wavefunction in the *Schrödinger equation*, one can confirm that most of the terms cancel with each other, in specific the ones referent to the time evolution of the unperturbed system, and yield to the Eq. 5.13.

$$i\hbar\sum_n e^{-i\omega_{sp}nt}\left(\dot{c}_n(t)\, e^{-i\frac{\omega_0}{2}t}\,|e,n\rangle + \dot{\tilde{c}}_n(t)\, e^{i\frac{\omega_0}{2}t}\,|g,n\rangle\right) = -\left(g\hat{\sigma}^+ + g^*\hat{\sigma}^-\right)\cdot\left(\hat{\mathbf{c}} + \hat{\mathbf{c}}^\dagger\right)|\psi(t)\rangle \tag{5.13}$$

The only terms that remain are the one's associated coupling between the TLA and the SPP waves. In fact, this formulation is analogous to the Interaction picture. However, the time evolution of the unperturbed system is not comprised in the operators but in the states.

$$|\psi(t)\rangle = \sum_n c_n(t)\, e^{-i\frac{\omega_0}{2}t} e^{-i\omega_{sp}2nt} |e, 2n\rangle + \tilde{c}_n(t)\, e^{i\frac{\omega_0}{2}t} e^{-i\omega_{sp}(2n+1)t} |g, 2n+1\rangle \tag{5.14}$$

A useful mechanism to understand what states are solutions to the system is to analyze what happens to an initial state $|i\rangle$ if the *Hamiltonian* operator is applied to it. As it is known, the only term that is able to modify $|i\rangle$ into another state is the $\hat{\mathbf{H}}_{int}$, since because $|i\rangle$ is a natural eigenmode of the unperturbed system and thus it remains unaltered. Therefore, imposing that the initial state is $|e, 0\rangle$, as stated above, and applying $\hat{\mathbf{H}}_{int}$ to it, the new possible state generated is $|g, 1\rangle$. Repeating this process successively o the new states produced, we find that it leads to $|e, 2\rangle$, $|g, 3\rangle$, $|e, 3\rangle$, etc. One may continue until realizes that a pattern shows up. The only terms that are created in the excited state correspond to even photon numbers, whereas for the ground state only the even photons' numbers constitute the solution. This is rapidly understood considering that if one has a state $|e, 2n\rangle$ ($n \in \mathbb{N}$) and exploits the outcome of $(g\hat{\sigma}^+ + g^*\hat{\sigma}^-) \cdot \left(\hat{\mathbf{c}} + \hat{\mathbf{c}}^\dagger\right) |e, 2n\rangle$, observes that the only terms that are created are $|g, 2n+1\rangle$ and $|g, 2n-1\rangle$, since the operator $\hat{\boldsymbol{\sigma}}^+$ has no atomic level to which it raises. Similarly, if one has the state $|g, 2n+1\rangle$ the only resulting states would be $|e, 2(n+1)\rangle$ and $|e, 2n\rangle$ which leads to even modes, also because there is no lower state than the ground state.

Nevertheless, one may argue that if the chosen initial state was $|g, 1\rangle$, then by the same reasoning the solutions of the system would be the states $|g, 2n\rangle$ and $|e, 2n+1\rangle$. This solution, that is completely different from the previous one, proves that the initial condition is extremely important to extrapolate a basis for the system. As it is intended that the TLA is excited and that no photon is being emitted in the initial state is ($|e, 0\rangle$), the general wavefunction can be restructured as in Eq. 5.14. Thus, replacing this new configuration at Eq. 5.13 and attending that $\hat{\mathbf{c}}\,|n\rangle = \sqrt{n}\,|n-1\rangle$ and $\hat{\mathbf{c}}^\dagger\,|n\rangle = \sqrt{n+1}\,|n+1\rangle$, one can manipulate the equation into two another equations 5.15, where the excited and ground atomic states are disassociated from each other.

$$\sum_n \dot{c}_n(t)\, e^{-i\omega_{sp}2nt} |e, 2n\rangle = g\frac{i}{\hbar} \sum_n \tilde{c}_n(t)\, e^{i\omega_0 t} e^{-i\omega_{sp}(2n+1)t} \left(\sqrt{2n+2}\,|e, 2n+2\rangle + \sqrt{2n+1}\,|e, 2n\rangle\right) \tag{5.15a}$$

$$\sum_n \dot{\tilde{c}}_n(t)\, e^{-i\omega_{sp}(2n+1)t} |g, 2n+1\rangle = g^*\frac{i}{\hbar} \sum_n c_n(t)\, e^{-i\omega_0 t} e^{-i\omega_{sp}2nt} \left(\sqrt{2n+1}\,|g, 2n+1\rangle + \sqrt{2n}\,|g, 2n-1\rangle\right) \tag{5.15b}$$

Moreover, invoking the fact that the states must be the equal either in the left and the right sides of the equations, it follows

Actually, this result is in agreement to what we would expect, since the only way to create an state with an even number of photons is by using the interaction *Hamiltonian* on the odd ones, and vice-versa. Also, the direct dependence in the first derivative of a given state, by the states with a difference of only one photon is also predictable, because of the structure of $\hat{\mathbf{H}}_{int}$ that does not allow to a state annihilate instantaneously more than one light *boson*. Yet, the first derivatives expressions obtained have always a recurrence relation with the other coefficients relative to different states. Therefore, since it is impossible to compute a solution for infinite coefficients, the procedure selected to solve approximately this system of differential equations is to impose a maximum number of coefficients and truncate the upper coefficients. To accomplish this task, we resorted to the computational power of the *Wolfram Mathematica* software. It is worth to mention that there are some particularities in two of the differential equations of the system in question by truncating coefficients. In fact, if the coefficients range from 0 to n, then in Eq. 5.16a the term $\tilde{c}_{n-1}$ must be zero since it is not in the range.

Likewise, the term c_{n+1} in Eq. 5.16b must also be zero.

$$\dot{c}_n(t) = g\frac{i}{\hbar}e^{i\omega_0 t}\left(\tilde{c}_{n-1}(t)\sqrt{2n}e^{i\omega_{sp}t} + \tilde{c}_n(t)\sqrt{2n+1}e^{-i\omega_{sp}t}\right) \tag{5.16a}$$

$$\dot{\tilde{c}}_n(t) = g^*\frac{i}{\hbar}e^{-i\omega_0 t}\left(c_n(t)\sqrt{2n+1}e^{i\omega_{sp}t} + c_{n+1}(t)\sqrt{2n+2}e^{-i\omega_{sp}t}\right) \tag{5.16b}$$

One should also recall that to determine the dynamics of the system, the condition of the initial state $|e,0\rangle$ must also be applied, which implies that at $t = 0$ one has $c_0 = 1$ and all the remaining terms are zero. Thus, it is assumed henceforth that the coefficients start at $n = 0$.

5.2.1 Comparison of the Exact Solution with *RWA* Approximation

In this subsection, it shall be compared the solutions which are obtained from the *Schödinger equation* by using the *Hamiltonian* in the *RWA* versus the ones acquired by using the *Hamiltonian* in Eq. 5.11 without any approximation. For the purpose of this contrast, it is enough to consider only a set of three states in the ground state ($|g,1\rangle$, $|g,3\rangle$ and$|g,5\rangle$) and three in the atomic excited level ($|e,0\rangle$, $|e,2\rangle$ and $|e,4\rangle$).

Therefore we start to present the *Hamiltonian* using the *RWA* in Eq. 5.17, where the terms that yield to non-conservative terms are cancelled.

$$\hat{\mathbf{H}}_{RWA} = \frac{\hbar\omega_{sp}}{2}\hat{\mathbf{c}}^\dagger\hat{\mathbf{c}} + \frac{\hbar\omega_0}{2}\hat{\sigma}_z - (g\hat{\sigma}^+\cdot\hat{\mathbf{c}} + g^*\hat{\sigma}^-\cdot\hat{\mathbf{c}}^\dagger) \tag{5.17}$$

This system and many other light-matter interactions where it is only considered a single mode of the Electromagnetic field has known solution [90]. In fact, it is easy to verify that if the system is in the initial state $|e,0\rangle$ the only new state generated by applying the $\hat{\mathbf{H}}_{RWA}$ is the state $|g,1\rangle$. If one repeats this process once again to $|g,1\rangle$, it is discerned that the search for new states that may solve the system finds its end.

Hence, the system becomes analogous to the one addressed in the subsection 4.2.2, when discussing the *Rabi oscillations*. Indeed, even the wavefunction that solves the system and that is represented in Eq. 5.18 is somehow similar to one presented in Eq. 4.10.

$$|\psi(t)\rangle = c_e(t)\,e^{-i\frac{\omega_0}{2}t}|e,0\rangle + c_g(t)\,e^{i\frac{\omega_0}{2}t}e^{-i\omega_{sp}t}|g,1\rangle \tag{5.18}$$

Moreover, resorting to the *Schrödinger equation* one can attain the equations 5.19a and 5.19b, through simple algebra manipulation.

$$\dot{c}_e(t) = g\frac{i}{\hbar}e^{i(\omega_0-\omega_{sp})t}c_g(t) \tag{5.19a}$$

$$\dot{c}_g(t) = g^*\frac{i}{\hbar}e^{-i(\omega_0-\omega_{sp})t}c_e(t) \tag{5.19b}$$

Using once again the notation $\Delta = \omega_{sp} - \omega_0$ and defining new frequency variables $\tilde{\Omega} = \frac{\sqrt{\Delta^2+4\Omega^2}}{2}$ and $\Omega = \frac{|g|}{\hbar}$, it is found that the general solution for this problem is given by Eq. 5.20a and Eq. 5.20b, where A_1, A_2, B_1 and B_2 are unknown constants.

$$c_e(t) = e^{-i\frac{\Delta}{2}t}\left[A_1\cos\left(\tilde{\Omega}t\right) + A_2\sin\left(\tilde{\Omega}t\right)\right] \tag{5.20a}$$

$$c_g(t) = e^{i\frac{\Delta}{2}t}\left[B_1\cos\left(\tilde{\Omega}t\right) + B_2\sin\left(\tilde{\Omega}t\right)\right] \tag{5.20b}$$

Using the condition of the initial state at $t = 0$ and stressing the case where the system is in coherence ($\omega_{sp} = \omega_0$), $c_e(t)$ and $c_g(t)$ simplify into Eq. 5.21a and Eq. 5.21b, respectively.

$$c_e(t) = \cos(\Omega t) \tag{5.21a}$$

$$c_g(t) = \sin(\Omega t) \tag{5.21b}$$

These *Rabi oscillations* are represented in Figure 5.1 together with the solutions for the exact *Hamiltonian* of Eq. 5.17 in the weak coupling regime and in the resonance.

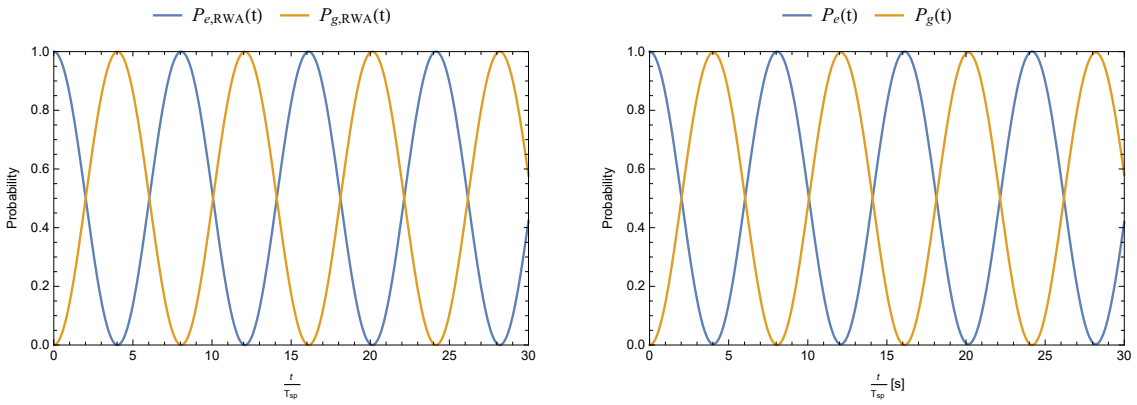

Figure 5.1: Plots of the probabilities $\mathrm{P}_e(t)$ (blue curve) and $\mathrm{P}_g(t)$ (orange curve), for a distance $r_0 = 10$ nm and considering a *rydberg atom* with $|\gamma| = 1212 \times 10^{-30}$ C m. The left graphic corresponds to the system in the *RWA* and the right graphic corresponds to the solution for the exact *Hamiltonian*, using 100 coefficients for its computation.

It is concluded by the figure that the approximation made by the *RWA* represents the original system with a high level of accuracy, as stated in the literature where is also necessary near resonance condition [87]. it is worth to mention that, since that in this section it is only addressed the lossless case, the probabilities of the states in the excited atomic level ($\mathrm{P}_e(t)$) and in the ground states ($\mathrm{P}_g(t)$) reveal a symmetry in relation to 50% as they must sum up to one.

Assuming now a higher value of g, by considering a distance $r_0 = 1$ nm and a *Rydberg atom*, it is made the same comparison to the solutions obtained in the *RWA* and with the original *Hamiltonian*, whose solution is truncated to 200 coefficients. The probabilities $\mathrm{P}_e(t)$ and $\mathrm{P}_g(t)$ are represented in Figure 5.2 for the RWA and the exact *Hamiltonian* in the graphics on left and right sides, respectively. It is certainly clear that the graphics bear no resemblance, and in fact, it seems that represent two completely different systems. As result, the *RWA* should not model a system with a strong interaction, since its essential features are lost in this approximation, such as the contribution of higher states that are important to characterize its dynamics. Another intriguing difference is that the number of oscillations in the *RWA* is higher (with a frequency $\frac{|g|}{\hbar}$), while that in the original system the probabilities $\mathrm{P}_e(t)$ and $\mathrm{P}_g(t)$ oscillate slowly and almost constantly near a probability of 50%. This is expected since the system is not binary as in the case of the *RWA* where only two coefficients exist. Hence, for a given instant there are more possible transitions either to an excited or a ground state, having each state its proper oscillatory pattern that, when sum all the contributions, concedes a steadier oscillation around the 50% probability.

5.2.2 System's Strong versus Weak Coupling

In this subsection is evaluated how the variation of the coupling strength g influences interaction between the TLA and the SPP waves over the time.

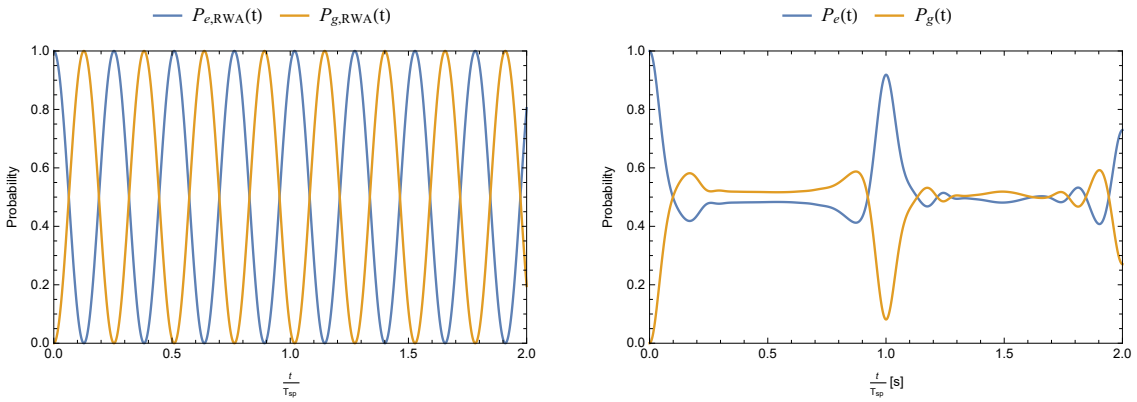

Figure 5.2: Plots of the probabilities $\mathrm{P}_e\,(t)$ (blue curve) and $\mathrm{P}_g\,(t)$ (orange curve), for a distance $r_0 = 1\,\mathrm{nm}$ and considering a *rydberg atom* with $|\gamma| = 1212 \times 10^{-30}\,\mathrm{C\,m}$. The left graphic corresponds to the system in the *RWA* and the right graphic corresponds to the solution for the exact *Hamiltonian*, using 200 coefficients for its computation.

Attending to Eq. 5.16 it is possible to infer that $\frac{|g|}{\hbar}$ as units of frequency, and so it is convenient to normalize this parameter and also the other frequency terms that appear in the computation of the coefficients (ω_{sp} and ω_0). Thereby, it is arbitrarily chosen to normalize these variables in relation to $\omega_s p$ so that the new variables become $\tilde{g} = \frac{g}{\hbar\omega_{sp}}$, $\tilde{\omega}_0 = \frac{\omega_0}{\omega_{sp}}$ and the surface plasmon is set to one unit. For this problem, one of the terms that has more influence in the behavior and time evolution of the coefficients' values is $\tilde{g}$, that symbolizes the strength of the coupling. Furthermore, by inspecting the *Hamiltonian* of the system is visible that for $\tilde{g} \geq 1$ the dipole perturbation becomes of the same magnitude order than the unperturbed system, and hence the system is considered to have a strong coupling. Otherwise, for $\tilde{g} \ll 1$ the coupling between the atom and the metal slab is weak. As seen before by the relation $g = \gamma^* \sqrt{\frac{\hbar\omega_{sp}}{32\pi\varepsilon_0 r_0^3}}$ and $\tilde{g} = \frac{g}{\hbar\omega_{sp}}$, the only way to change $\tilde{g}$ is by modifying the distance r_0 or by considering quantum objects with different electric dipole moment. Therefore, it is presented the absolute value of this parameter in Table 5.1 for different values of r_0 and $|\gamma|$.

Table 5.1: Values of $|\tilde{g}|$ for different values of electric dipole moment and for distinct values of r_0.

		r_0[nm]			
		1	2	5	10
$\gamma\left[10^{-30}\,\mathrm{C\,m}\right]$	1212	1.9635	0.6942	0.1756	0.0621
	10	0.0162	0.0057	0.0015	0.005

Inspecting the above Table it is seen that only for the *Rydberg* atom is reached the strong coupling, whereas for the typical values of $|\gamma|$, the system falls into the weak coupling regime even for the highest value. Moreover, by the formula and Table5.1, it is possible to conclude that coupling strength is modified more quickly by the variation of the distance r_0 since their proportionality is of $r_0^{-3/2}$, while that for the $|\gamma|$ the variation is linear.

Proceeding with the analysis, values with different magnitudes for investigating their influence in the time evolution of the systems were chosen. The selected values of $\tilde{g}$ are the ones corresponding to a *Rydberg atom* ($\gamma = 1212 \times 10^{-30}\,\mathrm{C\,m}$) for distances r_0 of 1 nm, 2 nm and 10 nm. One may realize that it is not examined the case where the electric dipole moment varies, but, since that ultimately what influences the behavior of the system is the value of $\tilde{g}$, it is enough to see how the latter is modified by $|\gamma|$. In addition, the regimes there are meant to be investigated and compared are the ones having a strong and weak coupling between the TLA and the SPP waves. Then it is visible by Table 5.1 that for $|\gamma| = 10 \times 10^{-30}\,\mathrm{C\,m}$ (typical value order) the only regime that is covered is the weak coupling, while that for the chosen scenarios, it is covered the weak, the strong and an intermediate state of both.

Beginning with $r_0 = 1\,\mathrm{nm}$, the solution for the coefficients $c_n\,(t)$ and $\tilde{c}_n\,(t)$ is computed truncating the

infinite possible number of states. Hence, N is defined to be the maximum number of states in the excited level and also for the ground levels, *i.e.*, $c_i\,(t) = 0$ and $\tilde{c}_i\,(t) = 0$ for $i > N$.

In this situation, due to the presence of a strong interaction, it is reckoned that the number of states relevant in the interaction will be greater than for the case where a small perturbation is entailed. Thereby, it is used $N = 10$ and $N = 20$ to ensure that the computed solutions have a good accuracy, and at the same time allow to perceive the magnitude order of states for which the system represents a good approximation. For the sake of simplicity, it is said that $\tilde{g}$ is real-valued and that all the forthcoming plots are scaled in time with a normalization to the time period of surface plasmon oscillation ($T_{sp} = \frac{2\pi}{\omega_{sp}}$).

The Figure 5.3 plots the probability of the states in an excited atomic level ($\mathrm{P}_e\,(t)$) and of the ones in the ground states ($\mathrm{P}_g\,(t)$), where the left side corresponds to having $N = 20$ and the right side to having $N = 10$. As one may see, these graphics present some differences, although that the principal nodes are captured by the one with less accuracy ($N = 10$). This means that the terms above the states $|g, 21\rangle$ and $|e, 20\rangle$ still have contribution enough to alter the overall probabilities $\mathrm{P}_e\,(t)$ and $\mathrm{P}_g\,(t)$, *i.e.*, the probability of the system transiting to a state with twenty "quanta" is not so negligible.

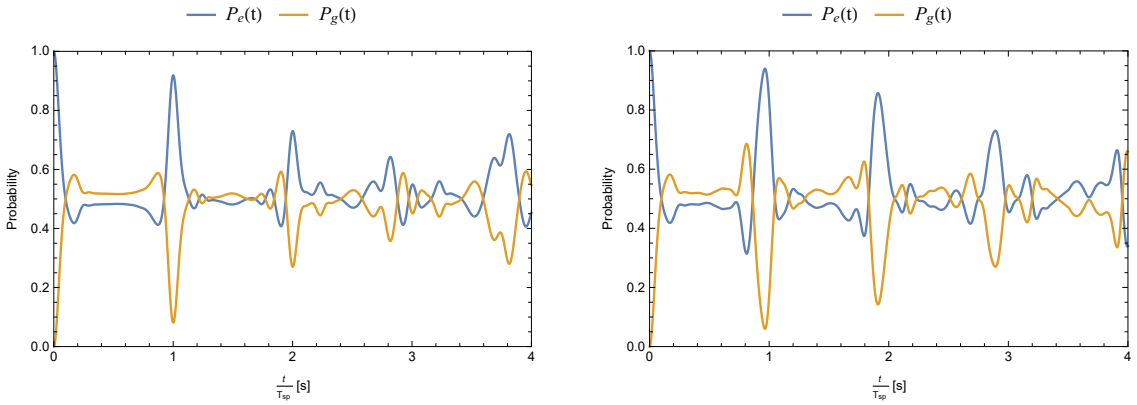

Figure 5.3: Plots of the probabilities $\mathrm{P}_e\,(t)$ (blue curve) and $\mathrm{P}_g\,(t)$ (orange curve), for a distance $r_0 = 1$ nm and considering a *rydberg atom* with $|\gamma| = 1212 \times 10^{-30}$ C m. The left and right graphics correspond to a truncation number of $N = 20$ and $N = 10$, respectively.

Furthermore, one may also compare the first four coefficients for both the truncation numbers in Figures 5.4 and 5.5, being in the former represented $\tilde{c}_0\,(t)$ and $c_0\,(t)$, and in the latter $\tilde{c}_1\,(t)$ and $c_1\,(t)$. Besides the small discrepancy observed in these graphics, it is worth to mention that, in spite of $\tilde{c}_1\,(t)$ and $c_1\,(t)$ having a lower probability most of the time than $\tilde{c}_0\,(t)$ and $c_0\,(t)$, probabilities that achieve are also high. This confirms that, in the strong coupling regime, the number of states to which the system can transit with a significant probability is higher. One can interpret this as a redistribution of the probability of finding the system in a given state over more states, instead of being concentrated in the two states with lower energy. Obviously, this implies that the *RWA* should not be applied to a system in these conditions.

In the case with $r_0 = 2$ nm, a similar procedure regarding the previous one was adopted. In Figure 5.6, $\mathrm{P}_e\,(t)$ and $\mathrm{P}_g\,(t)$ are plotted for $N = 4$ (graphic on the right) and $N = 100$ (graphic on the left). Moreover, in the same way as before, the first four coefficients for both values of N are exhibited in Figures 5.7 and 5.8. The huge difference in the terms truncated serves to highlight that the approximation that is made just by considering four coefficients of the ground and excited states, is almost as good as the one considering 100. One of the biggest differences observed by the graphics between the distances $r_0 = 2$ nm and $r_0 = 1$ nm is that, in the former, the variations are much smoother whether that in latter the oscillations are more abrupt (suggesting the presence of higher frequency components in the frequency spectrum). One may argue that, since the coupling strength $\tilde{g}$ has units of frequency and that for shorter distances $\tilde{g}$ increases, it is only normal that the effects felt on the graphics $r_0 = 1$ nm also vary more rapidly.

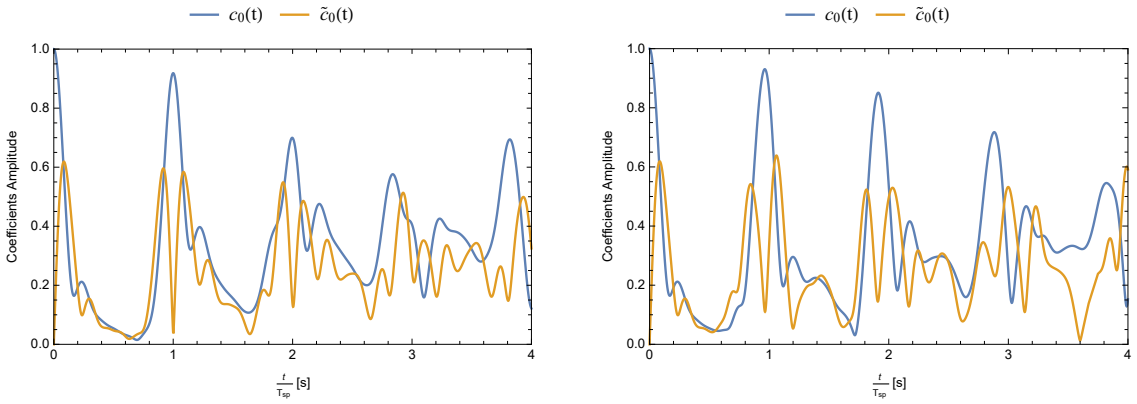

Figure 5.4: Plots of the probabilities $|c_0(t)|^2$ (blue curve) and $|\tilde{c}_0(t)|^2$ (orange curve), for a distance $r_0 = 1\,\text{nm}$ and considering a *rydberg atom* with $|\gamma| = 1212 \times 10^{-30}\,\text{C m}$. The left and right graphics correspond to a truncation number of $N = 20$ and $N = 10$, respectively.

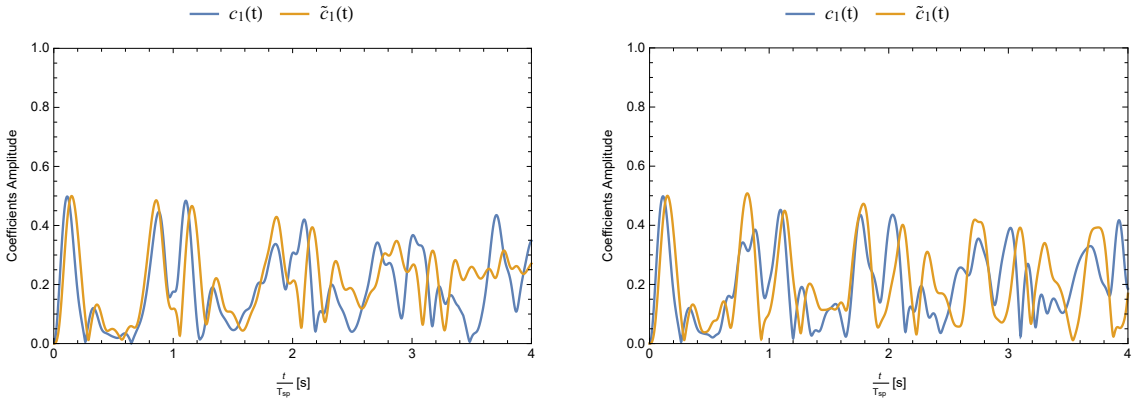

Figure 5.5: Plots of the probabilities $|c_1(t)|^2$ (blue curve) and $|\tilde{c}_1(t)|^2$ (orange curve), for a distance $r_0 = 1\,\text{nm}$ and considering a *rydberg atom* with $|\gamma| = 1212 \times 10^{-30}\,\text{C m}$. The left and right graphics correspond to a truncation number of $N = 20$ and $N = 10$, respectively.

The last scenario to be discussed is the weak coupling where $r_0 = 10\,\text{nm}$. Contrarily to the procedures applied before, it is reviewed the solution for only one truncation mode ($N = 50$) where the first four coefficients are exhibited in Figure 5.9. The plots show that the system's dynamics are essentially described by the first two coefficients, whose probability magnitude is far greater than the ones of the next states. This explains why only one truncation mode was used, since that it would not make much of a difference in neglecting states (other than $\tilde{c}_0(t)$ and $c_0(t)$) whose contribution is residual. Also, the probabilities $\mathrm{P}_e(t)$ and $\mathrm{P}_g(t)$ were already displayed in Figure 5.3, when comparing the exact solution with the one in the *RWA*. In comparison with the strong regime, the oscillations in the weak coupling are smoother, due to the smaller contribution of the higher states' frequency spectrum, and the transitions between states tend to occur at a slower rate (evidenced by the time scale of both regimes).

Another mechanism to observe the major differences that occur in the system as the coupling strength increases is trough the spectrum analysis of the probabilities $\mathrm{P}_e(t)$ and $\mathrm{P}_g(t)$. Therefore, it is computed the discrete *Fourier* transform for the three of coupling strength scenarios corresponding to $r_0 = 10\,\text{nm}$, $r_0 = 2\,\text{nm}$ and $r_0 = 1\,\text{nm}$ (for the *rydberg* atom). The spectres for the first four coefficients are presented in Figure 5.10, Figure 5.11, Figure 5.12, which correspond to the weak, medium and strong coupling scenarios, respectively. From these graphics it is possible to conclude that as the coupling strength increases not only the number of frequencies increases but also the value of the frequencies involved in the system, which is reasonable since that $\frac{g}{\hbar}$ has frequency units. The unique *Dirac delta* in the weak coupling is congruent with the only *Rabbi* oscillation

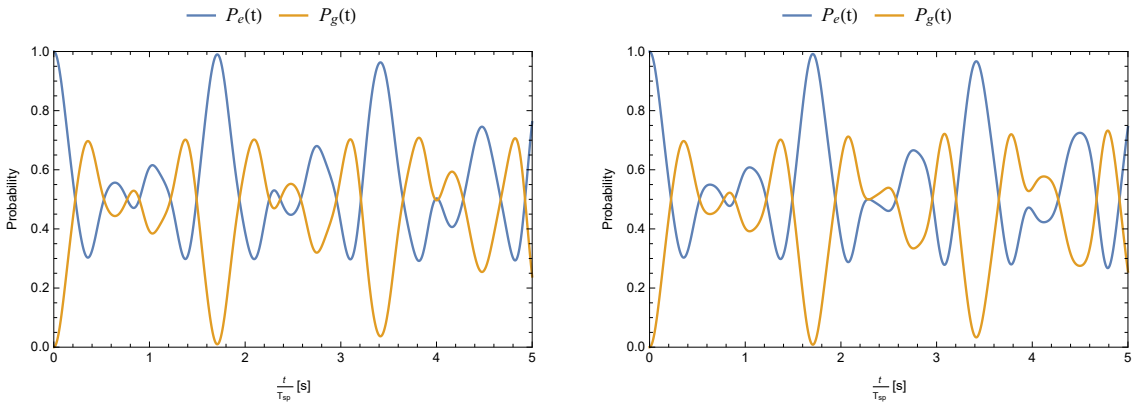

Figure 5.6: Plots of the probabilities $\mathrm{P}_e\,(t)$ (blue curve) and $\mathrm{P}_g\,(t)$ (orange curve), for a distance $r_0 = 2\,\mathrm{nm}$ and considering a *rydberg atom* with $|\gamma| = 1212 \times 10^{-30}\,\mathrm{C\,m}$. The left and right graphics correspond to a truncation number of $N = 100$ and $N = 4$, respectively.

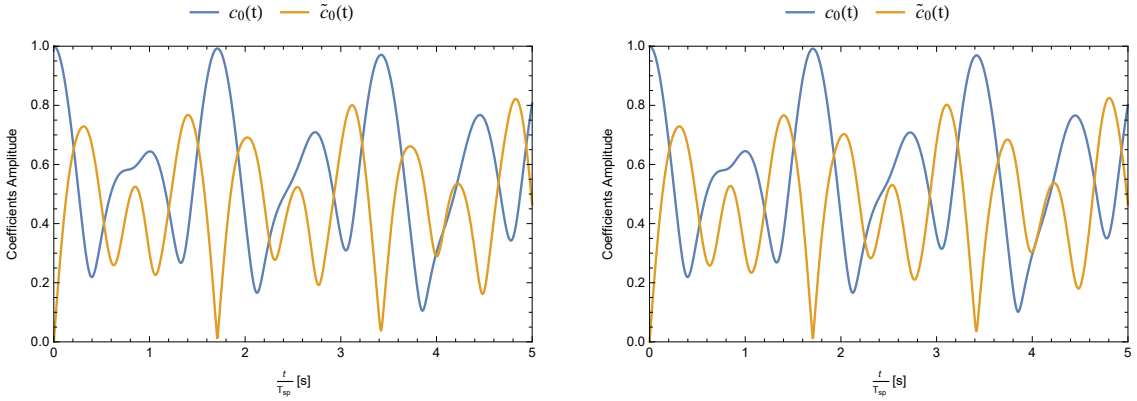

Figure 5.7: Plots of the probabilities $|c_0\,(t)|^2$ (blue curve) and $|\tilde{c}_0\,(t)|^2$ (orange curve), for a distance $r_0 = 2\,\mathrm{nm}$ and considering a *rydberg atom* with $|\gamma| = 1212 \times 10^{-30}\,\mathrm{C\,m}$. The left and right graphics correspond to a truncation number of $N = 100$ and $N = 4$, respectively.

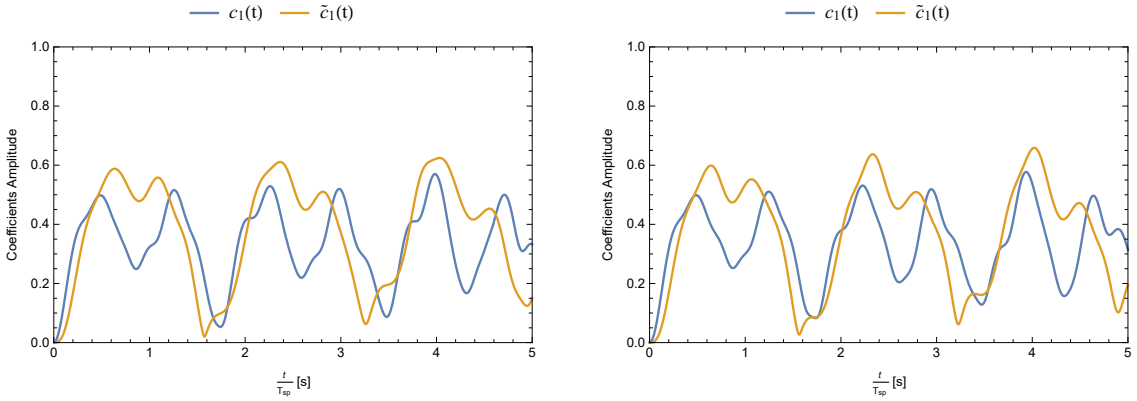

Figure 5.8: Plots of the probabilities $|c_1\,(t)|^2$ (blue curve) and $|\tilde{c}_1\,(t)|^2$ (orange curve), for a distance $r_0 = 2\,\mathrm{nm}$ and considering a *rydberg atom* with $|\gamma| = 1212 \times 10^{-30}\,\mathrm{C\,m}$. The left and right graphics correspond to a truncation number of $N = 100$ and $N = 4$, respectively.

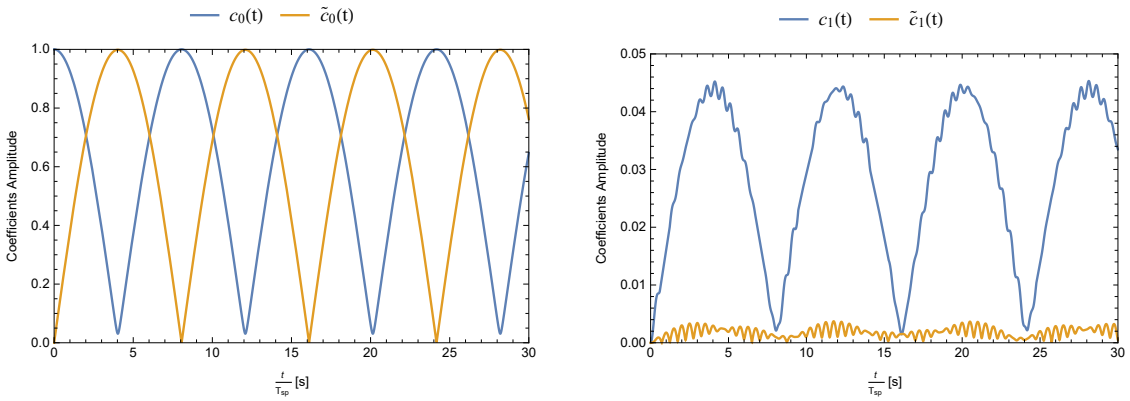

Figure 5.9: In the graphic of the left side are traced the plots that correspond to $|c_0\,(t)|^2$ (blue curve) and $|\tilde{c}_0\,(t)|^2$ (orange curve). In the graphic of the right side the plots correspond to the coefficients $|c_1\,(t)|^2$ (orange curve) and $|\tilde{c}_1\,(t)|^2$ (blue curve). Both graphics are plotted for the distance $r_0 = 2\,\text{nm}$ and is assumed a *rydberg atom* as the TLA, having $|\gamma| = 1212 \times 10^{-30}\,\text{C m}$.

(also observed in the RWA) where the frequency corresponds to $\tilde{g}$. The amplitudes of the peaks are obtained through the discrete *Fourier* transform and, therefore, their values are dependent on the number of samples as the sampling interval with used in the computation.

The excited and ground state in the same energy level seem to possess the same frequency peaks, which may be explained by the fact that both states have the same energy and experience the perturbation in the same way. For the strong coupling the peaks are almost equally spaced by a frequency interval near the plasmon resonance. In conclusion, stronger perturbations imply a higher number of states into which is probable to transit. This leads to different ways to indirectly excite a given state, which consequently yields different frequencies or, in other words, to a more complex oscillatory pattern. The spectrum analysis shows that even with a weak perturbation, the state basis in use do not constitute an eigenbasis of the system because there are always at least one nonzero frequency with a peak.

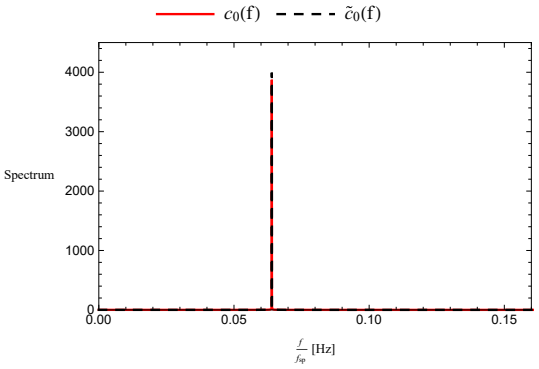

Figure 5.10: In the graphic of the left side is traced the spectrum correspondent to the coefficients $c_0\,(t)$ and $c_1\,(t)$, and on the the right side the ones correspondent to $\tilde{c}_0\,(t)$ and $\tilde{c}_1\,(t)$. Both graphics are plotted for the distance $r_0 = 10\,\text{nm}$ and is assumed a *rydberg atom* as the TLA, having $|\gamma| = 1212 \times 10^{-30}\,\text{C m}$.

5.2.3 Hamiltonian Matrix

For the case of the unperturbed system the *Hamiltonian* density matrix would be a diagonal matrix using its eigenbasis, where for the sake of simplicity is set the order sequence of the eigenstates in terms of the matrix as: $|e,0\rangle$, $|e,2\rangle$ ... $|e,2n\rangle$, $|g,1\rangle$, $|g,2\rangle$ ... $|g,2n+1\rangle$. Obviously, it is necessary to employ a truncation technique

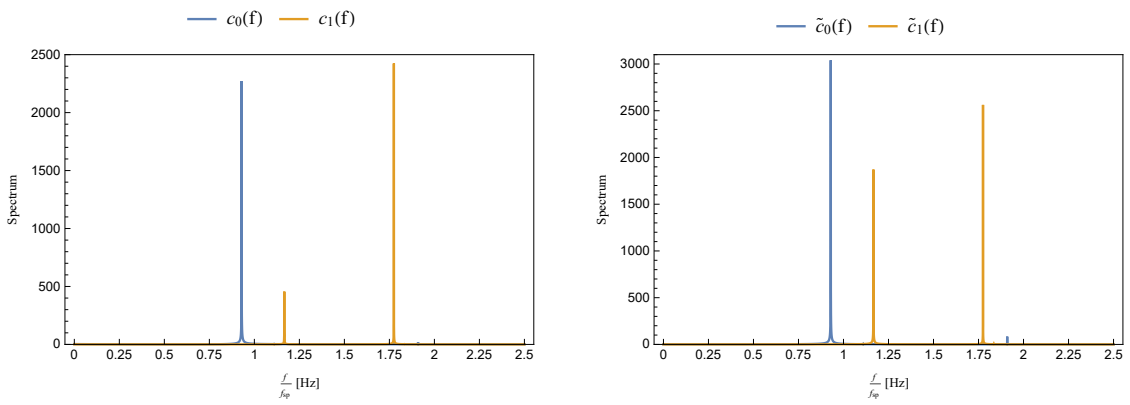

(a) (b)

Figure 5.11: In the graphic of the left side is traced the spectrum correspondent to the coefficients $c_0(t)$ and $c_1(t)$, and on the the right side the ones correspondent to $\tilde{c}_0(t)$ and $\tilde{c}_1(t)$. Both graphics are plotted for the distance $r_0 = 2$ nm and is assumed a *rydberg atom* as the TLA, having $|\gamma| = 1212 \times 10^{-30}$ C m.

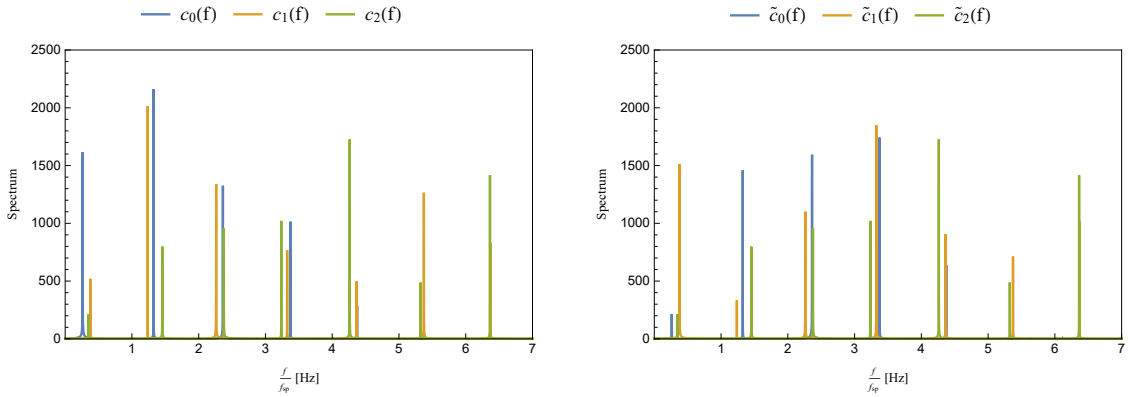

(a) (b)

Figure 5.12: In the graphic of the left side is traced the spectrum correspondent to the coefficients $c_0(t)$, $c_1(t)$ and $c_2(t)$, and on the the right side the ones correspondent to $\tilde{c}_0(t)$, $\tilde{c}_1(t)$ and $\tilde{c}_2(t)$. Both graphics are plotted for the distance $r_0 = 1$ nm and is assumed a *rydberg atom* as the TLA, having $|\gamma| = 1212 \times 10^{-30}$ C m.

to obtain a finite matrix, since the matrix is infinite.

Recalling that the density matrix is computed as in Eq.5.22, then it is straightforward to obtain the density matrix of the *Hamiltonian* on the presence of the perturbation, which may be retrieved from the matrix in Eq.5.23, where one can perceive the relation between a given coefficient and its anterior.

$$\begin{bmatrix} \langle 1|\,\mathbf{H}\,|1\rangle & \cdots & \langle 1|\,\mathbf{H}\,|N\rangle \\ \vdots & \cdots & \vdots \\ \langle N|\,\mathbf{H}\,|1\rangle & \cdots & \langle N|\,\mathbf{H}\,|N\rangle \end{bmatrix} \tag{5.22}$$

$$\begin{bmatrix} \hbar(\frac{\omega_0}{2}) & 0 & 0 & 0 & -g & 0 & 0 & 0 \\ 0 & \hbar(\frac{\omega_0}{2}+2\omega_{sp}) & 0 & 0 & -g\sqrt{2} & -g\sqrt{3} & 0 & 0 \\ 0 & 0 & \hbar(\frac{\omega_0}{2}+4\omega_{sp}) & 0 & 0 & -g\sqrt{4} & -g\sqrt{5} & 0 \\ 0 & 0 & 0 & \hbar(\frac{\omega_0}{2}+6\omega_{sp}) & 0 & 0 & -g\sqrt{6} & -g\sqrt{7} \\ -g^* & -g^*\sqrt{2} & 0 & 0 & \hbar(-\frac{\omega_0}{2}+\omega_{sp}) & 0 & 0 & 0 \\ 0 & -g^*\sqrt{3} & -g^*\sqrt{4} & 0 & 0 & \hbar(-\frac{\omega_0}{2}+3\omega_{sp}) & 0 & 0 \\ 0 & 0 & -g^*\sqrt{5} & -g^*\sqrt{6} & 0 & 0 & \hbar(-\frac{\omega_0}{2}+5\omega_{sp}) & 0 \\ 0 & 0 & 0 & -g^*\sqrt{7} & 0 & 0 & 0 & \hbar(-\frac{\omega_0}{2}+7\omega_{sp}) \end{bmatrix} \tag{5.23}$$

As one may identify, if the coupling strength as a nonzero value then the density of the matrix will not remain diagonal. This means that the eigenstates of the system are no longer the ones of the unperturbed system, *i.e.*, the new eigenstates that can in fact be measured are now a superposition of the previous eigenstates correspondent to the unperturbed system. As it will also be discussed, the new natural states will see their eigenergies being modified as the coupling strength increases. This type of analysis provides important insights in how the states of the system change and, in particular, how the previous states are related with the new ones as $\tilde{g}$ varies.

Considering that the new eigenstates are ordered as $|N\rangle$, $|N-1\rangle$ ... $|1\rangle$, $|0\rangle$, where higher eigenergy corresponds to $|N\rangle$ and the lower one to $|0\rangle$, then it can be computed the transformation matrix that transforms the previous basis in this new basis. Considering first the habitual scenario of weak coupling, the transformation matrix, as well as its inverse, are given in Figure 5.13, which are obtained by solving first the diagonalization of the *Hamiltonian* density matrix. It is visible that the excited and ground level states having the same energy (*e.g.*,$|e,2i\rangle$and $|g,2i+1\rangle$) generate the new states through a linear combination, having almost the same absolute contribution ($1/\sqrt{2}$). For example, the new lower eigenstate, $|0\rangle$, is practically given by $-\frac{1}{\sqrt{2}}|e,0\rangle-\frac{1}{\sqrt{2}}|g,1\rangle$, and the second lower, $|1\rangle$, by $\frac{1}{\sqrt{2}}|e,0\rangle-\frac{1}{\sqrt{2}}|g,1\rangle$. In fact, in spite of the new eigenenergies are still very similar to the previous ones, this new ones have a small deviation. Moreover, it was observed that for linear combinations where the contribution from the two old states have contrary signal, the energy will be greater in comparison when the contributions have the same signal. For example, in the case of the eigenergy correspondent to $|1\rangle$ this will be $E_1=\hbar(-\frac{\omega_0}{2}+\omega)(1+\triangle)$ while that for $|0\rangle$ its eigenergy is $E_1=\hbar(-\frac{\omega_0}{2}+\omega)(1-\triangle)$, where $\triangle$ is a small deviation. More specifically, if it is considered $\hbar=\omega=\omega_0=1$, for the sake of simplicity, then the new eigenenergies obtained for this weak coupling scenario are: 6.7, 6.3, 4.6, 4.4, 2.6, 2.4, 0.6, 0.4. Since that the new eigenstates are composed by only two of the previous states, it is only normal that only a *Rabbi* oscillation will appear in the spectrum, since the state can only transit between two states.

$$\begin{pmatrix}|7\rangle\\|6\rangle\\|5\rangle\\|4\rangle\\|3\rangle\\|2\rangle\\|1\rangle\\|0\rangle\end{pmatrix} = \begin{pmatrix} 0. & 0. & 0. & 0.7 & 0. & 0. & -0.1 & -0.7\\ 0. & 0. & 0. & 0.7 & 0. & 0. & -0.1 & 0.7\\ 0. & 0. & 0.7 & -0.1 & 0. & 0. & -0.7 & 0.\\ 0. & 0. & 0.7 & 0.1 & 0. & 0. & 0.7 & 0.\\ 0. & 0.7 & 0. & 0. & 0. & -0.7 & 0. & 0.\\ 0. & 0.7 & 0. & 0. & 0. & 0.7 & 0. & 0.\\ 0.7 & 0. & 0. & 0. & -0.7 & 0. & 0. & 0.\\ -0.7 & 0. & 0. & 0. & -0.7 & 0. & 0. & 0. \end{pmatrix} \begin{pmatrix}|e,0\rangle\\|e,2\rangle\\|e,4\rangle\\|e,6\rangle\\|g,1\rangle\\|g,3\rangle\\|g,5\rangle\\|g,7\rangle\end{pmatrix}$$

(a)

$$\begin{pmatrix}|e,0\rangle\\|e,2\rangle\\|e,4\rangle\\|e,6\rangle\\|g,1\rangle\\|g,3\rangle\\|g,5\rangle\\|g,7\rangle\end{pmatrix} = \begin{pmatrix} 0. & 0. & 0. & 0. & 0. & 0. & -0.7 & 0.7\\ 0. & 0. & 0. & 0. & -0.7 & 0.7 & 0. & 0.\\ 0. & 0. & 0.7 & -0.7 & 0. & 0. & 0. & 0.\\ -0.7 & 0.7 & -0.1 & -0.1 & 0. & 0. & 0. & 0.\\ 0. & 0. & 0. & 0. & 0. & 0. & 0.7 & 0.7\\ 0. & 0. & 0. & 0. & 0.7 & 0.7 & 0. & 0.\\ 0.1 & -0.1 & -0.7 & -0.7 & 0. & 0. & 0. & 0.\\ 0.7 & 0.7 & 0. & 0. & 0. & 0. & 0. & 0. \end{pmatrix} \begin{pmatrix}|7\rangle\\|6\rangle\\|5\rangle\\|4\rangle\\|3\rangle\\|2\rangle\\|1\rangle\\|0\rangle\end{pmatrix}$$

(b)

Figure 5.13: The matrix on the left side corresponds to the transformation on the previous basis to the new eigenbasis of the perturbed system, while the matrix on the right side corresponds to the inverse transformation. Both matrices are consider a truncation up to the first eight states and considering a coupling strength correspondent to a distance $r_0=10$ nm and a *rydberg atom* as the TLA.

For a medium coupling strength, the transformation matrices are displayed in Figure 5.14. In comparison with the previous case, where the new eigenstates had their main contribution due to only two terms, here they are projected in much more states. However, the higher and the lower new eigenstates are projected (with significance) into fewer states, since there are no immediate upper and lower states into to transit, respectively. From the structure of $\mathbf{H}_{Int}$, an atomic excited/ground state can only transit to the immediate ground/excited states with one photon difference. Hence, as $\tilde{g}$ gets stronger, the states also tend to indirectly transit, with an higher probability, to the states with two and even three photons differences. However, since the immediate states of a given state $|i\rangle$ also can transit back to $|i\rangle$, the projection is not so intuitive to perceive. Moreover, the new eigenerergies are 8.8, 6.4, 5, 3.7, 2.6, 1.4, 0.8, -0.5, from where it is seen that the deviations regarding the unperturbed eigenergies increases and it is even possible to achieve negative energies.

In the strong coupling scenario the transformation matrices are presented in Figure 5.15. The correct approach would be to use an higher truncation for this scenario. However, the dimension of the matrices would be too big to display them. Attending to this flaw, important comments to make in this regime are to the fact that the projection of the older states in the new eigenstates becomes piratically uncorrelated. Moreover the

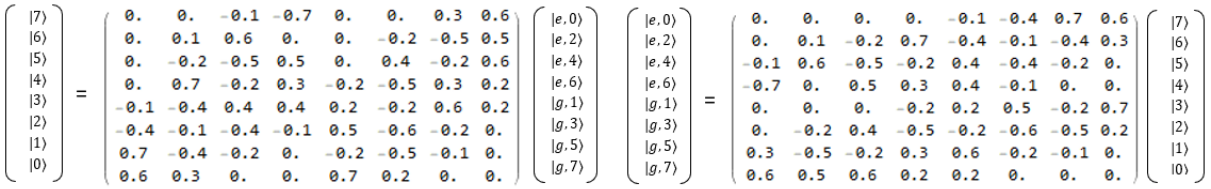

Figure 5.14: The matrix on the left side corresponds to the transformation on the previous basis to the new eigenbasis of the perturbed system, while the matrix on the right side corresponds to the inverse transformation. Both matrices are consider a truncation up to the first eight states and considering a coupling strength correspondent to a distance $r_0 = 2$ nm and a *rydberg atom* as the TLA.

new eigenergies are 13.7, 9.6, 6.2, 3.4, 1.3, -0.3, -2.2, -3.7, where the deviations are even more visible since the energy due to the perturbation is significantly high and the relationship of these eigenergies with the ones of the unperturbed system become unclear.

The time evolution of this new eigenstates probably have a time evolution $e^{-i\frac{E_i t}{\hbar}}$, being E_i the correspondent eigenenergy. Therefore, having the unperturbed states projected in terms of the new eigenbasis should allow to obtain the time evolution of the former states. In addition, the times evolution of the unperturbed states and of the coefficients $c_n(t)$ and $\tilde{c}_n(t)$ are related in such a way that the only difference in its spectrum is a shift on the frequency for the observed peaks.

A general wavefunction for the system represented in this eigenbasis may be of the form $|\psi\prime(t)\rangle = \sum_k \alpha_k e^{-i\omega'_k t}|k\rangle$, which contains the same information as the wavefunction $|\psi(t)\rangle$ of Eq. 5.14 in the previous basis. Therefore, assuming that both wavefunctions are the same but in different basis, then one may compute the probability to measure the state $|e,0\rangle$, *i.e.*, $\|\langle e,0|\psi(t)\rangle\|^2$ which must be equal to $|e,0\rangle$, *i.e.*, $\|\langle e,0|\psi\prime(t)\rangle\|^2$. In the unperturbed basis it is straightforward to show that this probability results in the coefficient $\|c_0(t)\|^2$. On the other hand in the other basis (the eigenbasis) the projection of the $|e,0\rangle$ in this basis must be done, which will depend in the coupling regime considered. Using the weak coupling as example, $|e,0\rangle \approx \frac{1}{\sqrt{2}}|0\rangle - \frac{1}{\sqrt{2}}|1\rangle$ which one may further check (assuming $\alpha_0, \alpha_1 \in \Re$) that its probability yields to

$$\|\langle e,0|\psi\prime(t)\rangle\|^2 = \frac{1}{2}\left[\alpha_0^2 + \alpha_1^2 + 2\cos\left((\omega'_1 - \omega'_0)\,t\right)\right] \tag{5.24}$$

Therefore, this result must be equal to the coefficient $\|c_0(t)\|^2$. One may verify in Figure 5.10 that the result of the previous equation is in agreement with the spectrum, since it shows only one peak for a frequency other than zero. The same procedure could be undertaken for the other coupling regimes, however they are not addressed here.

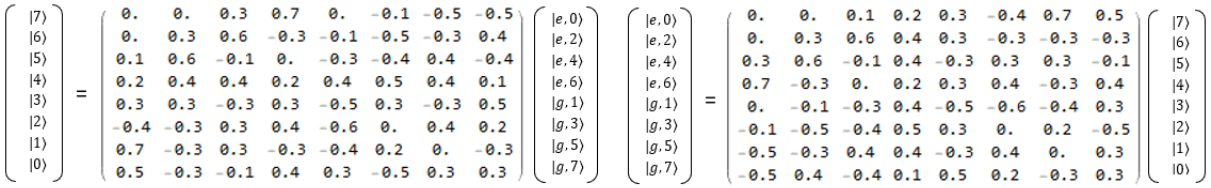

Figure 5.15: The matrix on the left side corresponds to the transformation on the previous basis to the new eigenbasis of the perturbed system, while the matrix on the right side corresponds to the inverse transformation. Both matrices are consider a truncation up to the first eight states and considering a coupling strength correspondent to a distance $r_0 = 1$ nm and a *rydberg atom* as the TLA.

5.2.4 Detuning Influence in the System Dynamics

In order to understand the influence of the detuning between ω_0 and ω_{sp} in the system's behavior, two different scenarios of detuning are addressed, which are further compared with the resonance case. These two scenarios correspond to having $\omega_0 \gg \omega_{sp}$ and $\omega_0 \ll \omega_{sp}$. In addition, the discussion highlights the differences between the weak and the strong coupling.

Starting with the weak coupling regime ($r_0 = 10\,\text{nm}$), the graphics of probabilities $\mathrm{P}_e(t)$ and $\mathrm{P}_g(t)$ for $10\omega_0 = \omega_{sp}$ and $\frac{\omega_0}{10} = \omega_{sp}$ are plotted in Figure 5.16, in the graphic on the right and in the left, respectively. The case of resonance was already displayed in Figure 5.2. The first big difference is spotted between the resonance case and the other two with $\omega_0 \neq \omega_{sp}$, wherein the former intense oscillations are observed while for the other scenarios, the system tends to remain in the initial state ($|e,0\rangle$) over the time. This means that in a weak coupling regime, if the TLA does not have an atomic frequency near the radiation waves frequency supported by the interacting metal slab, that in this case corresponds solely to ω_{sp}, then these two systems barely interact with each other and consequently almost no SPP quanta are radiated. However, for $\omega_0 \ll \omega_{sp}$ there are still identified some oscillations in the probabilities even that very closely of 1 for $\mathrm{P}_e(t)$ and of 0 for $\mathrm{P}_g(t)$. These oscillations in the perspective of the energy seem a little counter-intuitive, since that, because the initial state has a lower energy ($\hbar\omega_0$) than one in the ground state containing an SPP photon, it would be expected that the atom would not have enough energy to excite states where photons are emitted. However, by solving the differential equations system in Eq. 5.15 the solutions indicate that transitions to the ground states where SPP waves appear are possible.

In contrast, for $\omega_0 \ll \omega_{sp}$ the system manifest no modification of its initial state over the time. Thereby, the state $|e,0\rangle$, that is an eigenstate for the system unperturbed ($\hat{\mathbf{H}}_{EM} + \hat{\mathbf{H}}_{At}$) appears to be also an eigenstate of $\hat{\mathbf{H}}_{int}$ since it remains unaltered.

In conclusion, is observed that for the weak coupling the detuning of the atomic frequency in relation with ω_{sp} enables the systems to be treated separately as a good approximation, since the interaction between both is negligible.

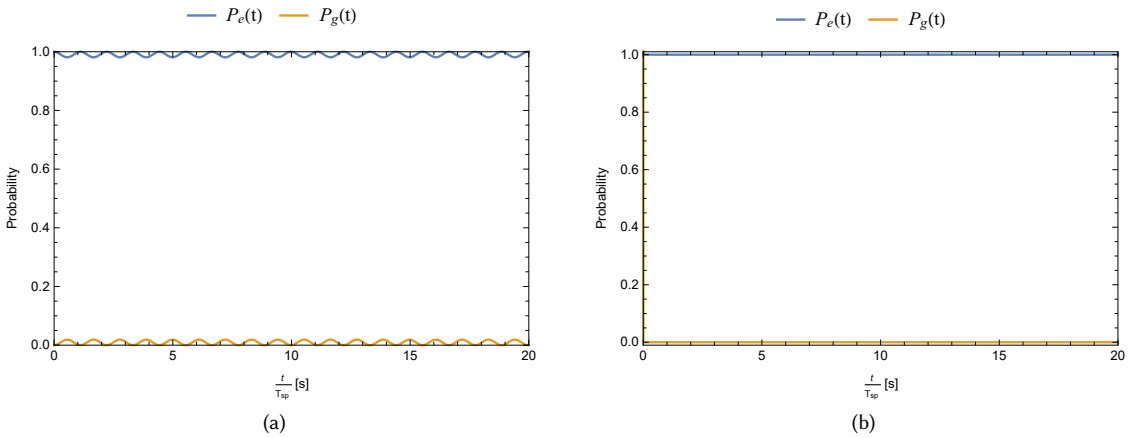

Figure 5.16: In the graphic of the left side are traced the plots that correspond to $\mathrm{P}_e(t)$ (blue curve) and $\mathrm{P}_g(t)$ (orange curve) for the case where $\frac{\omega_0}{10} = \omega_{sp}$. In the graphic of the right side the probabilities $\mathrm{P}_e(t)$ (blue curve) and $\mathrm{P}_g(t)$ (orange curve) are referent to having $10\omega_0 = \omega_{sp}$. Both graphics are plotted for the distance $r_0 = 10\,\text{nm}$ and is assumed a *rydberg atom* as the TLA, having $|\gamma| = 1212 \times 10^{-30}\,\text{C m}$.

Moving now to the strong coupling regime, the probabilities of the excited and ground states are represented in Figure 5.11 for $10\omega_0 = \omega_{sp}$ and $\frac{\omega_0}{10} = \omega_{sp}$, corresponding, respectively, to the graphics on the right and left side. Also, the plot of the resonance was previously presented in Figure 5.3, from where is observed a rapid oscillation either for $\mathrm{P}_e(t)$ or $\mathrm{P}_g(t)$ around the 50% probability. As stated before, this behavior may be explained by interference effects as a result of the overall contribution of the frequency spectrum of each relevant state.

Comparing this regime with the one for $\frac{\omega_0}{10} = \omega_{sp}$, what is discovered is that for the latter, the oscillations amplitude of $\mathrm{P}_e(t)$ and $\mathrm{P}_g(t)$ also achieve values of 50%, though their values vary within a wider probability range. Moreover, for $\frac{\omega_0}{10} = \omega_{sp}$ the system presents a surprising feature, that is related with the oscillations pattern regarding $\mathrm{P}_e(t)$ and $\mathrm{P}_g(t)$. This pattern resembles the typical *FM* modulation of a carrier, that is registered in Telecommunication systems. However, the envelope of these *FM* signals present the modulation of several frequencies. These frequencies may be associated with the intrinsic oscillatory pattern of each one of the states that have a meaningful contribution. This would also explain why the same behaviour in the weak coupling regime, with the same conditions, is not observed. To comprehend better this phenomenon the time evolution of the first four coefficients are plotted in Figure 5.18 for $10\omega_0 = \omega_{sp}$ and $\frac{\omega_0}{10} = \omega_{sp}$, in the graphics of the right and left, respectively. One may immediately notice that all the coefficients for $\frac{\omega_0}{10} = \omega_{sp}$ present a principal common oscillation frequency, which corresponds to the carrier frequency in analogy to the *FM* modulation.

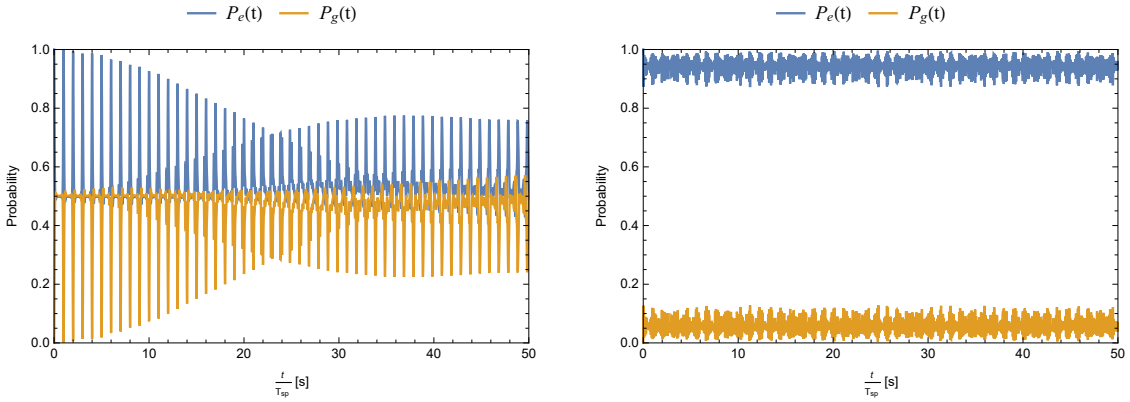

Figure 5.17: In the graphic of the left side are traced the plots that correspond to $\mathrm{P}_e(t)$ (blue curve) and $\mathrm{P}_g(t)$ (orange curve) for the case where $\frac{\omega_0}{10} = \omega_{sp}$. In the graphic of the right side the probabilities $\mathrm{P}_e(t)$ (blue curve) and $\mathrm{P}_g(t)$ (orange curve) are referent to having $10\omega_0 = \omega_{sp}$. Both graphics are plotted for the distance $r_0 = 1$ nm and is assumed a *rydberg atom* as the TLA, having $|\gamma| = 1212 \times 10^{-30}$ C m.

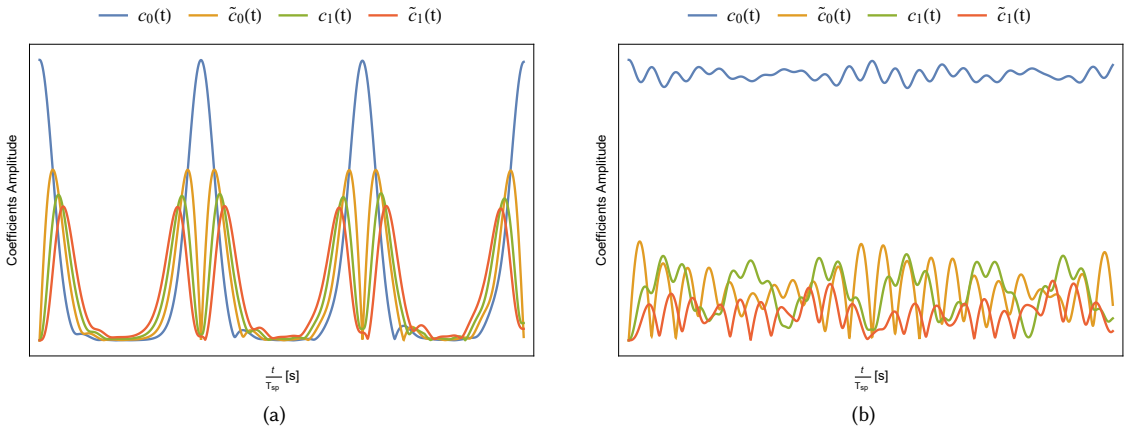

Figure 5.18: Plots of the probabilities $|c_0(t)|^2$ (blue curve), $|\tilde{c}_0(t)|^2$ (orange curve), $|c_1(t)|^2$ (green curve), $|\tilde{c}_1(t)|^2$ (red curve). The graphic on the left side corresponds to having $\frac{\omega_0}{10} = \omega_{sp}$ and the one on the right to $10\omega_0 = \omega_{sp}$. It was used a distance $r_0 = 2$ nm and it was considered a *rydberg atom* with $|\gamma| = 1212 \times 10^{-30}$ C m.

For the case of $10\omega_0 = \omega_{sp}$, besides no evident pattern is found, the states oscillate slightly but very rapidly. In addition the system presents probability values near one for $\mathrm{P}_e(t)$ and around zero for $\mathrm{P}_g(t)$. This shows that as the interaction *Hamiltonian* becomes stronger, the basis formed by the eigenstates of the coupled system

becomes more dissimilar in relation to the basis formed by the unperturbed *Hamiltonian* eigenstates, since the states transition oscillations occur at a higher rate. In addition, this result supports the idea found in the weak coupling regime, that for $\omega_0 \ll \omega_{sp}$, the transitions to other states still occur.

On the other hand, for $\omega_0 \gg \omega_{sp}$ the system over the time tends to stay in the initial state $|e, 0\rangle$, being more difficult for the system to transit to other possible states. The behavior of the system should be the inverse, by reasoning that an initial state having higher energy should be able to excite states with lower energy and the inverse should not occur. However, one must recall that the eigenstates and consequently the eigenenergies of the unperturbed system will suffer a hybridization when the interaction is included. Therefore, an analysis of the possible states formed in this hybridization and an explanation of how most likely the initial state will be projected in this new eigenbasis must be done, in order to comprehend intuitively what should occur to the system in each detuning scenario. However, this type of analysis is out of the scope of this work, reason why it is not addressed.

5.3 SPP-TLA Interaction Accounting with Loss Processes

Hereafter, it is shown how the introduction of loss channels in the interaction between the non-local SPP and the TLA influence their dynamics and what is the lifetime τ of the oscillations for the several eigenmodes of the system. The comparison between the coupling regimes in the presence of losses is stressed out. The evaluation between the lossless and loss description models is also addressed hereafter.

The introduction of radiation loss can be performed by defining $\omega_0^+ = \omega_0 + i\omega_0'$ and $\omega_0^- = \omega_0 - i\omega_0'$ and rewriting the wavefunction in Eq. 5.14, as in Eq 5.25.

$$\omega_0'' = -\frac{\Gamma_{sp}}{2} \tag{5.25}$$

By doing this, it is basically assumed that all the states are exponentially vanishing over time, being ω_0' dependent from the emission rate through the relation in Eq. 5.26.

$$|\psi(t)\rangle = \sum_n c_n(t)\, e^{-i\frac{\omega_0^-}{2}t} e^{-i\omega_{sp}2nt} |e, 2n\rangle + \tilde{c}_n(t)\, e^{i\frac{\omega_0^+}{2}t} e^{-i\omega_{sp}(2n+1)t} |g, 2n+1\rangle \tag{5.26}$$

This dependence [38, 91] is set as shown in Eq. 5.23 where $\frac{1}{2}$ term emerges when computing the temporal average of the Poynting vector.

The next step involves solving the *Schrödinger* equation inn order to obtain a system of differential equations. This procedure curiously yields to the same differential equations system in Eq. 5.16 for the system without losses. This in turn indicates that with this introduction of radiative losses, the transition patterns remain intact, *i.e.*, the coefficients are exactly the same. However the overall state has the exponential decaying property.

Two distinct cases of the losses are considered: weak coupling and strong coupling. For the first one, it was assumed an emission rate $\Gamma = 2 \times 10^{13}$ Hz, which was chosen by plotting the emission rate and picking an emission rate value near its maximum peak. In this regime, the emission rate was plotted for a distance ($r_0 = 10$ nm) and $|\gamma| = 100 \times 10^{-30}$ C m. The electric dipole moment was chosen to be the one magnitude lower than the one of the *Rydberg atom*, because if the latter was used, then the value of the emission rate would be higher than ω_{sp}. Consequently, the system would disperse all its energy before any observation of oscillation in the state's probability occurred. For the strong coupling, the same reasoning was applied. But in this case, the emission rate used for the losses was $\Gamma = 8 \times 10^{14}$ Hz, where a distance ($r_0 = 1$ nm) and $|\gamma| = 100 \times 10^{-30}$ C m were considered. The plots of the probabilities $\mathrm{P}_e(t)$ and $\mathrm{P}_g(t)$ are presented in Figure 5.19, wherein the left side of the graphics is encountered the weak coupling regime and on the right side the strong coupling regime. What one may observe is that a higher number of oscillations for the weak coupling occur before all the energy is lost

and the probabilities go to zero. This is explained through the lifetime $\tau = 1/\omega_0''$, since that for the weak coupling regime the emission rate value is lower, and consequently yielding to a larger τ than when compared with the strong regime, where the emission rate is higher. As seen before for a higher coupling strength $\tilde{g}$ the oscillations of in probability of the states occur at a higher rate. However, this result shows that, although the oscillation is higher for the case where a lower distance r_0 is assumed, also the lifetime τ of the system decreases. In fact, from the formula of the emission rate is possible to see that the emission rate increases exponentially with the decreasing of the distance, while that $\tilde{g}$ only increases with a magnitude of $\frac{3}{2}$. Hence, is only natural that growth of the oscillations rate is not sufficient to counterattack the effect of the τ decrease, which is translated in a lower number of oscillations before the probability collapse to zero.

The coefficients probability is also presented for both regimes in Figure 5.20. The main observation inferred by this image is that in the case of strong coupling the number of visible states is higher than in the weak one, where the response is fully captured by the two initial states.

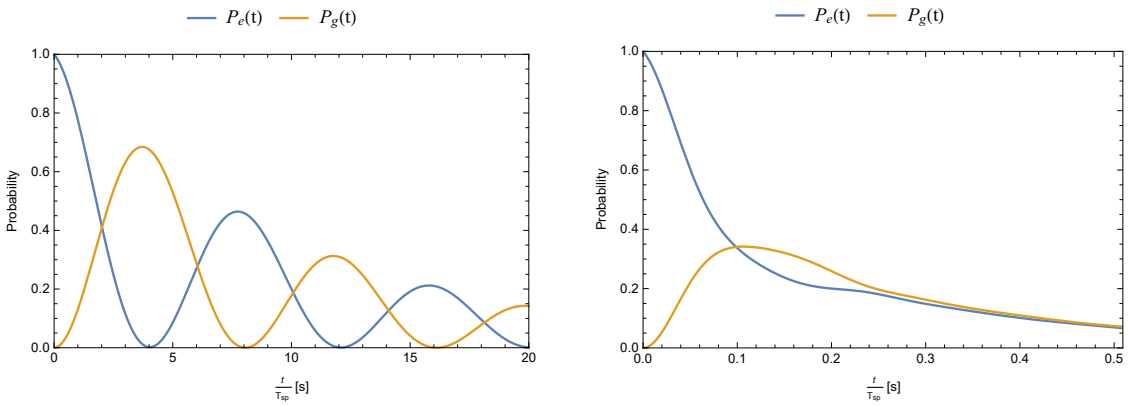

Figure 5.19: Plots of the probabilities $\mathrm{P}_e\,(t)$ (blue curve) and $\mathrm{P}_g\,(t)$ (orange curve), where graphics on the left and right side correspond to weak ($r_0 = 10$ nm and $\Gamma = 2 \times 10^{11}$ Hz) and strong ($r_0 = 10$ nm and $\Gamma = 8 \times 10^{12}$ Hz) coupling regime, respectively. It was used $|\gamma| = 100 \times 10^{-30}$ C m for both cases.

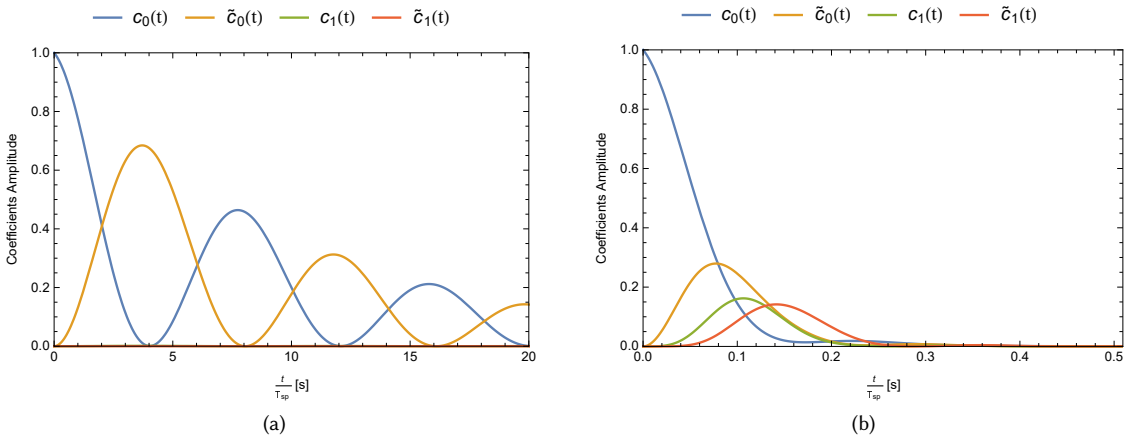

Figure 5.20: Plots of the probabilities$|c_0'\,(t)|^2$ (blue curve), $|\tilde{c}_0'\,(t)|^2$ (orange curve), where graphics on the left and right side correspond to weak ($r_0 = 10$ nm and $\Gamma = 2 \times 10^{13}$ Hz) and strong ($r_0 = 10$ nm and $\Gamma = 8 \times 10^{14}$ Hz) coupling regime, respectively. It was used $|\gamma| = 100 \times 10^{-30}$ C m for both cases.

Chapter 6

Conclusion

The purpose of this dissertation was to study the interaction between a TLA and SPP, where the former is placed in the vicinity of the metal slab, which supports SPP waves. To accomplish this objective, a local response of the metal slab and the quasi-static approximation for the system were assumed.

Another parallel objective for this work was to comprehend how the introduction of the nonlocality in the permittivity response of the SPP affects its propagation and in specific its dispersion relation. This analysis is made in comparison with the analogous local response, where for the sake of simplicity is considered the electrostatic regime in both scenarios. The study of the interaction between the TLA and the SPP waves was performed by analyzing the two systems individually as an initial approach.

Hence, for the SPP, a quantum description of its electromagnetic field is carried out for the local and non-local scenarios. Such is obtained by inspecting the energy of the electromagnetic field and by noticing that for each radiation mode a quantum harmonic oscillator can be associated. This allows writing the operator of the radiation field in terms of the creation and annihilation operators, which reproduce a discrete number of eigenenergies organized in an equally spaced ladder.

The same approach is made for the spatial dispersive SPP, where the diffusion effects are included in the permittivity via the phenomenological parameter β and using the *Hydrodynamic model*. This nonlocality means that the response of the permittivity in a given point depends not only of its response in that point but also in its surrounding region. This difficulty is surpassed by considering a solution formed by the sum of planar waves in the k domain. Thus, the permittivity acquires a dependence on the wave vector and it may be expressed as the sum of a longitudinal and transverse permittivity, as shown in Eq.3.9 and Eq.3.10, respectively. From these equations, it is visible that the spatial dispersion only affects the longitudinal component. Also, through the *Gauss's law*, an additional wave solution is observed, which is obtained by making this longitudinal component equal to zero.

In order to obtain the dispersion relation for the non-local SPP is necessary to use an *ABC* besides the habitual *Maxwellian* boundary conditions. This additional condition emerges due to the new degrees of freedom that arise in the medium due to its non-homogeneity. A usual procedure to resolve the arbitrariness in the ABC choice is by the use of constraints (with physical meaning) either for the charge density or the current.

Regarding the dispersion relation for the spatial dispersive medium in the quasi-static regime, it is seen that the value of ω is not constant for all the wavenumbers, in opposition to what happens in the local analogous. In the latter, the only frequency that supports waves is ω_{sp}. Furthermore, the monotonic curve presents a slight positive slope and the null wavevector is observed at $\omega = \omega_{sp}$, which implies that the propagation is made for frequencies above the surface plasmon resonance. It was also illustrated that if β increases, so does the slope of the curve.

The computed DOS for the non-local SPP confirms that the infinite number of states found for the local model (due to the $\delta(\omega - \omega_{sp})$) is redistributed over the interval of frequencies above ω_{sp}.

Regarding the atom description, in this study was employed the simplification of the TLA in order to quantize the atom. In this approximation, is assumed that the only relevant eigenenergies are the ground state and the one immediately above in terms of energy. The arguments that support this approximation lie on the consideration that an external radiation field must have a near resonance frequency from the atomic frequency relatively to these two states considered. Moreover, the frequency of the radiation must be detuned from frequencies associated with the neglected atomic levels. It was also considered the *Dipole Approximation*, which states that for wavelengths of the electric field much larger than the atomic dimensions, the field can be considered constant over the atom's region.

The solutions for the problem proposed are described in the basis formed by the tensorial product of the eigenstates of the unperturbed systems TLA and local SPP. Moreover, to obtain the time evolution of the system is considered a wavefunction containing the time evolution of the unperturbed *Hamiltonian* and an additional coefficient (time-dependent) to incorporate the time evolution of $\hat{\mathbf{H}}_{Int}$. This problem in the electrostatic regime gives origin to a system of differential linear equations that may be solved using the truncation of the coefficients above a chosen number. Also, it was determined that the solutions of the system, given the initial state $|e,0\rangle$, are of the form of $|e,2n\rangle$ and $|g,2n+1\rangle$ ($n \in \mathbb{N}$). Thus, the only states that can appear in this system in the atomic excited state correspond to states having an even number photons and being simultaneously in the ground state. This solution would be inverted if the initial state was $|g,0\rangle$.

The solutions obtained were evaluated in the weak and strong coupling regimes. The main conclusion that is extracted for the weak regime in resonance ($\omega = \omega_{sp}$) is that the number of states relevant to describe the dynamics of the interaction are mainly $|e,0\rangle$ and $|g,1\rangle$, which means that the system presents adversities to transit to the above states. Because of the small interference with higher states, the oscillation in the probabilities $\mathrm{P}_e\,(t)$ and $\mathrm{P}_g\,(t)$ are smooth and similar to the sinusoidal *Rabi oscillations*, addressed for the classically described radiation wave. Hence, the *RWA* represents a good approximation in these conditions.

However, in the strong coupling at the resonance, the number of coefficients, whose contribution entails most of the system evolution, is superior to the one found in the weak coupling regime. In addition, the probability of each state oscillated much faster is higher in this regime (strong coupling). The contribution of more states explains why the probabilities $\mathrm{P}_e\,(t)$ and $\mathrm{P}_g\,(t)$ have a non-smooth variation over the time, since the sum of the different frequency spectra for each state will cause interference effects. For this case, the *RWA* exhibits large discrepancies when compared to the real solution.

In the case of having $\omega_0 \ll \omega_{sp}$, is seen that exists a common oscillation frequency over the time for the coefficients probability, which acts as the carrier in a modulation *FM*. In the case of having $\omega_0 \gg \omega_{sp}$, the probabilities of the states are almost zero with the exception of the initial state, whose probability is near one. This means that the state tends to stay in the initial state, acting like an eigenstate of the total system including $\hat{\mathbf{H}}_{Int}$. If it is reasoned that the initial state has a higher energy than other states, then it should be possible to excite them and, otherwise, the system should remain in the same state. However, this behavior is the opposite to the one that is observed. Therefore, a detailed analysis of the hybridization of the new eigenstates of the system should be taken.

The interaction accounting with channel losses is also examined, where its inclusion is done through the emission rate phenomenon. The latter is derived using the *Fermi Golden Rule*, which consists in the first order term of the TDPT. Furthermore, it is also employed the *RWA* in order to keep the terms of $\hat{\mathbf{H}}_{Int}$ that are associated with energy conservation. The results of the emission rate for the non-local SPP displays a peak for frequencies near the surface plasmon resonance. The effect of the spatial dispersion in the emission rate is that for larger diffusion effect, the peak becomes wider and its maximum amplitude decreases. Therefore, in the local limit is possible to infer that the emission rate obtained will become a *Dirac delta*, which is in concordance to the local result.

In conclusion, the spatial dispersive response allows to frequencies above the ω_{sp} to support wave modes, which is intimately linked with the new longitudinal wave solution that appears for $\varepsilon_L(\omega, \overrightarrow{k}) = 0$. On the other

hand, this implies that the DOS in the non-local case is redistributed over a wider interval of frequencies and consequently the emission rate at ω_{sp} is no longer given by a result proportional to $\delta(\omega - \omega_{sp})$.

For future work, it may be developed a more accurate description of the spatial dispersion for the surface plasmons, *e.g.*, using other terms [92] that enable a better fit to the experimental data. Also, the study of the interaction of this plasmonic apparatus with a more interesting and complex system may be taken, like a multi-level atom with a degree higher than two. Then, a discussion about the dynamics of the new system in strong and weak coupling, as well as contrasting results with the TLA, should be extended.

Another development that could be made is the inclusion of other loss channels besides the one already considered due to the emission rate. An example of such, is the energy dispersed in the medium, which was initially introduced by the damping term in the permittivity. This introduction would need to be done in a heuristically way since the losses usually imply that the system's *Hamiltonian* loses its hermitian property.

It could also be investigated why the system in a detuning scenario presents an unexpected behavior, by analyzing the hybridization of the eigenstates of the unperturbed system that arises because of the interaction *Hamiltonian*.

The interaction between the SPP waves and the TLA described in this dissertation, but for the case where the medium has an anisotropic response, could also lead to an interesting problem.

Bibliography

[1] L. Novotny and B. Hecht, *Principles of Nano-Optics*. Cambridge University Press, 2006.

[2] M. Silveirinha, *Lecture Notes of Nano-Elecctromagnetic Plasmonics and Materials*, 2015.

[3] R. S. Anwar, H. Ning, and L. Mao, "Recent advancements in surface plasmon polaritons-plasmonics in subwavelength structures in microwave and terahertz regimes," *Digital Communications and Networks*, aug 2017.

[4] A. V. Zayats and I. I. Smolyaninov, "Near-field photonics: surface plasmon polaritons and localized surface plasmons," *Journal of Optics A: Pure and Applied Optics*, vol. 5, no. 4, pp. S16–S50, jun 2003. [Online]. Available: http://stacks.iop.org/1464-4258/5/i=4/a=353

[5] T. G. Philbin, "Canonical quantization of macroscopic electromagnetism," *New Journal of Physics*, vol. 12, no. 12, p. 123008, dec 2010.

[6] S. A. Maier, "Surface plasmon polaritons at metal / insulator interfaces," in *Plasmonics: Fundamentals and Applications*. Springer US, 2007, pp. 21–37.

[7] D. V. Sotnikov, A. V. Zherdev, and B. B. Dzantiev, "Detection of intermolecular interactions based on surface plasmon resonance registration," *Biochemistry (Moscow)*, vol. 80, no. 13, pp. 1820–1832, dec 2015.

[8] O. Benson, *Elements of Nanophotonics*, Humboldt-Universität zu Berlin, May 2009.

[9] I. Freestone, N. Meeks, M. Sax, and C. Higgitt, "The lycurgus cup — a roman nanotechnology," *Gold Bulletin*, vol. 40, no. 4, pp. 270–277, dec 2007.

[10] S. Sari, "Surface plasmon resonance (spr) configuration," The University of Sheffield, Sep. 2011. [Online]. Available: http://etheses.whiterose.ac.uk/2040/2/Sabban,_Sari.pdf

[11] X. Zhang and Z. Liu, "Superlenses to overcome the diffraction limit," *Nature Materials*, vol. 7, no. 6, pp. 435–441, jun 2008.

[12] D. M. West, *Fundamentos da Química Analítica*. Cengage, 2006. [Online]. Available: https://www.inesul.edu.br/site/documentos/QUIMICA_ANALITICA_SKOOG.pdf

[13] Allen, "Harmonic oscillator wavefunctions," Sep. 2010. [Online]. Available: https://upload.wikimedia.org/wikipedia/commons/9/9e/HarmOsziFunktionen.png

[14] "Casimir effect." [Online]. Available: https://byjus.com/physics/casimir-effect

[15] J. M. Fitzgerald, P. Narang, R. V. Craster, S. A. Maier, and V. Giannini, "Quantum plasmonics," *Proceedings of the IEEE*, vol. 104, no. 12, pp. 2307–2322, dec 2016.

[16] Y. Li, *Plasmonic Optics: Theory and Applications (Tutorial Texts)*. SPIE–The International Society for Optical Engineering, 2017.

[17] J. J. Hopfield, "Theory of the contribution of excitons to the complex dielectric constant of crystals," *Physical Review*, vol. 112, no. 5, pp. 1555–1567, dec 1958.

[18] J. M. Elson and R. H. Ritchie, "Photon interactions at a rough metal surface," *Physical Review B*, vol. 4, no. 12, pp. 4129–4138, dec 1971.

[19] Y. O. Nakamura, "Quantization of non-radiative surface plasma oscillations," *Progress of Theoretical Physics*, vol. 70, no. 4, pp. 908–919, oct 1983.

[20] M. S. Tame, K. R. McEnery, Ş. K. Özdemir, J. Lee, S. A. Maier, and M. S. Kim, "Quantum plasmonics," *Nature Physics*, vol. 9, no. 6, pp. 329–340, jun 2013.

[21] C. Schwartz and W. L. Schaich, "Hydrodynamic models of surface plasmons," *Physical Review B*, vol. 26, no. 12, pp. 7008–7011, dec 1982.

[22] R. Shankar, *Principles of Quantum Mechanics*. Springer US, 1994.

[23] Á. S. Sanz and S. Miret-Artés, *A Trajectory Description of Quantum Processes. II. Applications*. Springer Berlin Heidelberg, 2014.

[24] M. Razavy, *Quantum Theory of Tunneling*. WORLD SCIENTIFIC, jan 2003.

[25] P. Cappellaro, *22.51 Quantum Theory of Radiation Interactions*, MIT OpenCourseWare, 2012. [Online]. Available: https://ocw.mit.edu/courses/nuclear-engineering/22-51-quantum-theory-of-radiation-interactions-fall-2012/lecture-notes/MIT22_51F12_Notes.pdf

[26] F. Schwabl, *Advanced Quantum Mechanics*. Springer Berlin Heidelberg, 2005.

[27] M. G. Silveirinha and S. I. Maslovski, "Exchange of momentum between moving matter induced by the zero-point fluctuations of the electromagnetic field," *Physical Review A*, vol. 86, no. 4, oct 2012.

[28] M. G. Silveirinha, "Modal expansions in dispersive material systems with application to quantum optics and topological photonics," 2017.

[29] Dutra, *Cavity Quantum Electrodynamics*. John Wiley & Sons, 2004.

[30] N. M. Neil W. Ashcroft, *Solid State Physics*. Cengage Learning, Inc, 1976.

[31] I. H. Hutchinson, *Electromagnetic Waves in Plasmas*, 2003. [Online]. Available: https://ocw.mit.edu/courses/nuclear-engineering/22-611j-introduction-to-plasma-physics-i-fall-2003/lecture-notes/chap5.pdf

[32] G. P. P. Giuseppe Grosso, *Solid State Physics*. Elsevier LTD, Oxford, 2013.

[33] B. Ung, "Study of the interaction of surface waves with a metallic nano-slit via the finite-difference time-domain method," Master's thesis, Université Laval, 2007.

[34] M. Diem, *Modern Vibrational Spectroscopy and Micro-Spectroscopy*. John Wiley & Sons, Ltd, aug 2015.

[35] K. A. Milton, "The casimir effect: recent controversies and progress," *Journal of Physics A: Mathematical and General*, vol. 37, no. 38, pp. R209–R277, sep 2004.

[36] P. W. Milonni, *The Quantum Vacuum*. ACADEMIC PR INC, 1993.

[37] D. J. Griffiths and E. Ho, "Classical casimir effect for beads on a string," *American Journal of Physics*, vol. 69, no. 11, pp. 1173–1176, nov 2001.

[38] S. Lannebère and M. G. Silveirinha, "Negative spontaneous emission by a moving two-level atom," *Journal of Optics*, vol. 19, no. 1, p. 014004, dec 2016.

[39] M. Moeferdt, "Nonlocal and nonlinear properties of plasmonic nanostructures within the hydrodynamic drude model," 2017.

[40] Y. Luo, A. I. Fernandez-Dominguez, A. Wiener, S. A. Maier, and J. B. Pendry, "Surface plasmons and nonlocality: A simple model," *Physical Review Letters*, vol. 111, no. 9, aug 2013.

[41] C. David, "Two-fluid, hydrodynamic model for spherical electrolyte systems," *Scientific Reports*, vol. 8, no. 1, may 2018.

[42] R.-L. Chern, "Spatial dispersion and nonlocal effective permittivity for periodic layered metamaterials," *Optics Express*, vol. 21, no. 14, p. 16514, jul 2013.

[43] G. Barton, "Some surface effects in the hydrodynamic model of metals," *Reports on Progress in Physics*, vol. 42, no. 6, pp. 963–1016, jun 1979.

[44] J. M. Pitarke, V. M. Silkin, E. V. Chulkov, and P. M. Echenique, "Theory of surface plasmons and surface-plasmon polaritons," *Reports on Progress in Physics*, vol. 70, no. 1, pp. 1–87, dec 2006.

[45] E. K. U. Gross, C. A. Ullrich, and U. J. Gossmann, "Density functional theory of time-dependent systems," in *NATO ASI Series*. Springer US, 1995, pp. 149–171.

[46] A. Varas, P. García-González, J. Feist, F. García-Vidal, and A. Rubio, "Quantum plasmonics: from jellium models to ab initio calculations," *Nanophotonics*, vol. 5, no. 3, jan 2016.

[47] S. Raza, G. Toscano, A.-P. Jauho, M. Wubs, and N. A. Mortensen, "Unusual resonances in nanoplasmonic structures due to nonlocal response," *Physical Review B*, vol. 84, no. 12, sep 2011.

[48] R. Ruppin, "Non-local optics of the near field lens," *Journal of Physics: Condensed Matter*, vol. 17, no. 12, pp. 1803–1810, mar 2005.

[49] C. David and F. J. G. de Abajo, "Spatial nonlocality in the optical response of metal nanoparticles," *The Journal of Physical Chemistry C*, vol. 115, no. 40, pp. 19 470–19 475, sep 2011.

[50] R. Esteban, A. G. Borisov, P. Nordlander, and J. Aizpurua, "Bridging quantum and classical plasmonics with a quantum-corrected model," *Nature Communications*, vol. 3, no. 1, jan 2012.

[51] J. M. McMahon, S. K. Gray, and G. C. Schatz, "Calculating nonlocal optical properties of structures with arbitrary shape," *Physical Review B*, vol. 82, no. 3, jul 2010.

[52] S. I. Maslovski and S. A. Tretyakov, *Additional Boundary Conditions for Spatially Dispersive Media*. Instituto Superior Tecnico, 2000.

[53] A. Moreau, C. Ciracì, and D. R. Smith, "Impact of nonlocal response on metallodielectric multilayers and optical patch antennas," *Physical Review B*, vol. 87, no. 4, jan 2013.

[54] K. Joulain, R. Carminati, J. P. Mulet, and J. J. Greffet, "Definition and measurement of the local density of electromagnetic states close to an interface," 2003.

[55] E. N. Economou, *Green's Functions in Quantum Physics*. Springer Berlin Heidelberg, 2006.

[56] R. Carminati, A. Cazé, D. Cao, F. Peragut, V. Krachmalnicoff, R. Pierrat, and Y. D. Wilde, "Electromagnetic density of states in complex plasmonic systems," *Surface Science Reports*, vol. 70, no. 1, pp. 1–41, mar 2015.

[57] S. F. Cortizo, "On dirac's delta calculus," 1995. [Online]. Available: https://arxiv.org/abs/funct-an/9510004

[58] M. G. Silveirinha, S. A. H. Gangaraj, G. W. Hanson, and M. Antezza, "Fluctuation-induced forces on an atom near a photonic topological material," 2017.

[59] C. J. Foot, *Atomic Physics*. Oxford University Press, Nov. 2004.

[60] W. W. Chow, S. W. Koch, and M. Sargent, *Semiconductor-Laser Physics*. Springer Berlin Heidelberg, 1994.

[61] R. W. Boyd, *Nonlinear Optics*. Elsevier Science, 2008.

[62] M. Frasca, "A modern review of the two-level approximation," *Annals of Physics*, vol. 306, pp. 193–208, 2002.

[63] S. Zienau, "Optical resonance and two level atoms," *Physics Bulletin*, vol. 26, no. 12, pp. 545–546, dec 1975.

[64] A. A. Batista, "Rabi oscillations in two-level systems beyond the rotating-wave approximation," 2015.

[65] R. Bettles, "Single two-level atom," in *Springer Theses*. Springer International Publishing, 2017, pp. 15–37.

[66] C. W. Gardiner, *The Quantum World of Ultra-Cold Atoms and Light, Book I: Foundations of Quantum Optics*. IMPERIAL COLLEGE PR, 2014.

[67] C. George C. Schatz, Mark A. Ratner, *Quantum Mechanics in Chemistry*. DOVER PUBN INC, 2002.

[68] M. O. Scully and M. S. Zubairy, *Quantum Optics*. Cambridge University Press, 1997.

[69] M. A. Reed, "Quantum dots," *Scientific American*, vol. 268, no. 1, pp. 118–123, jan 1993.

[70] A. Zrenner, E. Beham, S. Stufler, F. Findeis, M. Bichler, and G. Abstreiter, "Coherent properties of a two-level system based on a quantum-dot photodiode," *Nature*, vol. 418, no. 6898, pp. 612–614, aug 2002.

[71] H. J. Krenner, S. Stufler, M. Sabathil, E. C. Clark, P. Ester, M. Bichler, G. Abstreiter, J. J. Finley, and A. Zrenner, "Recent advances in exciton-based quantum information processing in quantum dot nanostructures," *New Journal of Physics*, vol. 7, pp. 184–184, aug 2005.

[72] L. R. Radovic, *Chemistry & Physics of Carbon: Volume 31*. CRC PR INC, 2012.

[73] J. Keeling, *Light-Matter Interactions and Quantum Optics*. CreateSpace Independent Publishing Platform, 2014.

[74] F. Jelezko, T. Gaebel, I. Popa, A. Gruber, and J. Wrachtrup, "Observation of coherent oscillations in a single electron spin," *Physical Review Letters*, vol. 92, no. 7, feb 2004.

[75] I. Gerhardt, G. Wrigge, G. Zumofen, J. Hwang, A. Renn, and V. Sandoghdar, "Coherent state preparation and observation of rabi oscillations in a single molecule," 2008.

[76] M. S. Pierre Meystre, *Elements of Quantum Optics*. Springer Berlin Heidelberg, 2010.

[77] C. Cohen-Tannoudji, B. Diu, and F. Laloe, *Quantum Mechanics, Volume 2*. PAPERBACKSHOP UK IMPORT, 1977.

[78] J. M. Zhang and Y. Liu, "Fermi's golden rule: its derivation and breakdown by an ideal model," *European Journal of Physics*, vol. 37, no. 6, p. 065406, oct 2016.

[79] B. E. King, "Angular momentum coupling and rabi frequencies for simple atomic transitions," 2008.

[80] H. Hao, J. Ren, X. Duan, G. Lu, I. C. Khoo, Q. Gong, and Y. Gu, "High-contrast switching and high-efficiency extracting for spontaneous emission based on tunable gap surface plasmon," *Scientific Reports*, vol. 8, no. 1, jul 2018.

[81] T. F. Gallagher, "Rydberg atoms," *Reports on Progress in Physics*, vol. 51, no. 2, pp. 143–188, feb 1988.

[82] Y. Li and C. Argyropoulos, "Controlling collective spontaneous emission with plasmonic waveguides," *Optics Express*, vol. 24, no. 23, p. 26696, nov 2016.

[83] P. Góngora-Lugo and J. A. Maytorena, "Nonlocal effects on the spontaneous emission near a plasmonic nanowire," *Physical Review A*, vol. 95, no. 6, jun 2017.

[84] A. Messina, S. Maniscalco, and A. Napoli, "Interaction of bimodal fields with few-level atoms in cavities and traps," 2002.

[85] G. Benivegna and A. Messina, "Collective behavior ofMbosonic modes interacting with a single two-level atom," *Physical Review A*, vol. 37, no. 12, pp. 4747–4751, jun 1988.

[86] B. M. Garraway, "The dicke model in quantum optics: Dicke model revisited," *Philosophical Transactions of the Royal Society A: Mathematical, Physical and Engineering Sciences*, vol. 369, no. 1939, pp. 1137–1155, feb 2011.

[87] E. Jaynes and F. Cummings, "Comparison of quantum and semiclassical radiation theories with application to the beam maser," *Proceedings of the IEEE*, vol. 51, no. 1, pp. 89–109, 1963.

[88] P. Schneeweiss, A. Dareau, and C. Sayrin, "Cold-atom based implementation of the quantum rabi model," 2017.

[89] T. Meunier, A. L. Diffon, C. Rueff, P. Degiovanni, and J.-M. Raimond, "Entanglement and decoherence of n atoms and a mesoscopic field in a cavity," 2006.

[90] J. Larson, "Dynamics of the jayne-cummings and rabi models: old wine in new bottles," 2006.

[91] Y. C. Jun, R. D. Kekapture, J. S. White, and M. L. Brongersma, "Strong off-resonant enhancement of spontaneous emission in metal-dielectric-metal plasmon waveguide structures," 2008.

[92] A. Archambault, F. Marquier, J.-J. Greffet, and C. Arnold, "Quantum theory of spontaneous and stimulated emission of surface plasmons," *Physical Review B*, vol. 82, no. 3, jul 2010.